

**Host-Guest Assemblies for Functional Interfaces via Langmuir-Blodgett  
and Self-Assembly Technique**

Du Hyun Shin

Dissertation submitted to the Faculty of the Virginia Polytechnic Institute and State  
University in partial fulfillment of the requirements for the degree of

Doctor of Philosophy

In

Chemical Engineering

Stephen M. Martin, Chair  
Richey M. Davis  
William A. Ducker  
Sunghwan Jung

December 11, 2013, Blacksburg, VA

Keywords: Functional interfaces, organic molecular monolayer, Langmuir-Blodgett, self-assembly, low-density self-assembled monolayer, host-guest assemblies

# **Host-Guest Assemblies for Functional Interfaces via Langmuir-Blodgett and Self-Assembly Technique**

Du Hyun Shin

## **ABSTRACT**

Various technologies depend on interfacial events that are influenced by various molecular interactions at a solid-liquid interface. The functionality of a surface plays an important role in many applications such as catalysis, sensing, and bio-compatibility, which can benefit from distinctive chemical and physical surface properties. To create tailor-made functional surfaces, surface host-guest assemblies based on Langmuir-Blodgett and self-assembly technique have been employed as a model system as they may offer the potential ability to regenerate surface properties via intercalation of various functional guest molecules. This thesis ranges over the development and characterization of host-guest assemblies and their feasibilities for the regeneration of surface properties via intercalation of functional guests. In our work, 3-dimensional host structures with cavities are constructed on a targeted solid substrate using Langmuir-Blodgett and self-assembly techniques. In particular, by adopting the fundamental concept of host-guest interaction in supramolecular chemistry, we expect that structurally homologous guest molecules where functional groups are anchored can be intercalated into the cavities between hydrophobe arrays at the liquid-solid interface from solution under well-controlled conditions. This approach offers the potential of separating the functional of the monolayer from the inherent structure of the host.

The first part of this thesis details two-dimensional host-guest assemblies consisting of guanidinium (**G**), octadecylsulfonate (**S**) and various functional alkane guests at the air-aqueous interface and following deposition onto solid substrates via the Langmuir-Blodgett technique. In particular, we evaluated the stability of the host-guest assemblies and the

feasibility of exchanging molecular guests under exposure to various organic solvent environments. Analysis of X-ray reflectivity measurements of the thin films showed that good stability of the host-guest assembly could not be achieved due to weak interactions between the host monolayer and the solid surface. In addition, no evidence of intercalation of guest molecules into guest-free host-cavities was observed.

The second part of this thesis discusses the effective methodologies to prepare low-density self-assembled monolayers (LDSAMs) with cavities on silicon substrates. We employed a step-wise reaction based on hydrolytic or silane chemistry: integral spacer molecules such as anthracene-derivatives were anchored to the Si substrate and then long alkane chains were appended to the spacer molecules. The results showed that LDSAMs using an anthryl spacer are attached at the SAM/Si interface via a Si-O-C linkage, and the films do not exhibit a densely packed monolayer quality as would be expected for a non-sterically hindered alkyltrichlorosilane on Si. Thus, the resulting LDSAMs (with cavities) may be capable of accommodating other guest molecules with hydrocarbon chains through intercalation in order to form host-guest assemblies.

The third part of this thesis demonstrates the ability of LDSAMs to produce functional surfaces via the intercalation of various functional guest molecules. Self-assembled monolayers of (10-octadecyl)-9-anthracenethiol (host-SAMs) on Au substrates were prepared. Quartz crystal microbalance with dissipation (QCM-D) measurements was used to demonstrate the capacity of LDSAMs to confine guest molecules in the cavities and to probe the structural changes of the host-guest assembly during guest intercalation from ethanol solution. X-ray photoelectron spectroscopy (XPS) measurements were then used to probe host-guest monolayers formed by immersing the host monolayer in solutions in a variety of other solvents. A combined study of QCM-D and XPS showed that guest molecules were intercalated into host-cavities. The reversibility of the intercalation process allows a guest already situated in a host-cavity to be replaced with second guest under well-regulated solvent conditions.

To my wife, Jooeun, who has been through the journey with me

## Acknowledgements

To my mother, **Woni Im**, who passed away earlier this year, and my father, **Se-gyun Shin**. I cannot find the words to thank them. Also I have to thank **Ok-hyun**, **Hyun-suk**, and **Ae-suk**, my lovely sisters, for being my good friends, and so many thanks to my brothers-in-law, for being my great supporters.

I would like to thank my advisor, **Dr. Martin**. He truly taught me how to write, speak, and think with his enthusiasm and patience. Especially a careful concern he showed to me when I had a hard time is still unforgettable. I sincerely thank him.

I also would like to thank the members of my committee, **Dr. Ducker**, **Dr. Davis**, and **Dr. Jung** for being my sharpest critic. Their insightful comments, suggestions and encouragement helped me to accomplish my goal.

I thank **Dr. Michael F. Toney** and **Dr. Stefan Mannsfeld** at Stanford Synchrotron Radiation Laboratory (SSRL) for their help with the X-ray analysis, **Dr. Jerry Hunter** at Virginia Tech Nanoscale Characterization and Fabrication Laboratory (NCFL) for his help with my XPS work.

I have to thank **Hyung-ryul Joo** and his family. It has been ten years since he became my godfather. His continued support always helps me to stand up again. Special thanks to **Dr. Donmook Choi**, who encouraged me to think about how I should live.

Finally, I would like to thank my best friend, **Joeun Ko**, for her love, patience and support throughout all my years at Virginia Tech. I also thank her parents, **Kwang-uk Ko** and **Hae-sim Jung**, for their love and continued encouragement.

This work was funded by the National Science Foundation.

# Table of Contents

<b>Chapter 1</b> .....	1
Introduction.....	1
<b>Chapter 2</b> .....	5
Literature Review.....	5
2.1. Fundamental structure – functional organic molecules.....	5
2.2. Functional organic molecules .....	5
2.3. Functional monolayers on a surface.....	6
2.3.1. Functional monolayers on Au.....	8
2.3.2 Functional Monolayer on Silicon .....	8
2.4. Low-density LB films based on H-bonded network .....	9
2.5. Low-density SAMs.....	13
2.6. Surface characterization.....	14
2.6.1. Specular X-ray Reflectivity.....	14
2.6.2. Quartz Crystal Microbalance.....	18
2.6.3. X-ray Photoelectron Spectroscopy .....	21
2.7. References.....	26
<b>Chapter 3</b> .....	29
Host-Guest Assemblies for Functional Surfaces at the Air-Aqueous Interface.....	29
3.1. Introduction .....	29
3.2. Experimental Section.....	34
3.2.1. Materials .....	34
3.2.2. Surface Pressure-Area ( $\Pi$ -A) Isotherm and Langmuir-Blodgett Films.....	34
3.2.3. Grazing-angle incidence X-ray diffraction and X-ray Reflectivity .....	35
3.3. Results and Discussion .....	36
3.3.1. $\Pi$ -A isotherms for guest-free monolayers.....	36

3.3.2. II-A isotherms for host-guest monolayers .....	38
3.3.3. Stability of (G)C18S-based Langmuir-Blodgett films .....	39
3.4. Conclusion.....	49
3.5. Summary .....	50
3.6. References .....	51
<b>Chapter 4</b> .....	<b>54</b>
Low-Density Self-Assembled Monolayers Based on Integral Spacer .....	54
4.1. Introduction .....	54
4.2. Experimental Section.....	57
4.2.1. Materials .....	57
4.2.2. Substrate Preparation .....	57
4.2.3. Characterization of LDSAMs .....	57
4.2.4. Stepwise Reaction for the Formation of LDSAMs .....	58
4.3. Results and Discussion .....	61
4.4. Conclusions .....	72
4.5. Summary .....	72
4.6. References .....	73
<b>Chapter 5</b> .....	<b>75</b>
Host-Guest Assemblies via the Intercalation of Guest molecules on Low-Density Self-Assembled Monolayer	75
5.1. Introduction .....	75
5.2. Experimental .....	79
5.2.1. Materials .....	79
5.2.2. Sample preparation .....	79
5.2.3. Characterization of host-guest assembly .....	80
5.2.4. Synthesis.....	80
5.3. Results and Discussion .....	82
5.3.1. Examination of the host-guest assembly by QCM .....	83
5.3.2. Examination of the host-guest assembly by XPS.....	93
5.4. Conclusions .....	102
5.5. Summary .....	102

5.6. Reference.....	103
<b>Chapter 6</b> .....	105
Conclusions and Future work .....	105
<b>Appendix</b> .....	109
Supporting information for Low-Density Self-Assembled Monolayers Based on Integral Spacer.....	109
<b>Appendix A</b> - Electron density profiles for host-guest assemblies using LDSAM immersed in hexadecane solution in different solvents or different guest solution in toluene.....	109
Supporting information for Host-Guest Assemblies via the Intercalation of Guest molecules on Low-Density Self-Assembled Monolayer .....	111
<b>Appendix B</b> – XPS data for Host-Guest Assemblies via the Intercalation of Guest molecules on Low-Density Self-Assembled Monolayer .....	111
<b>Appendix C</b> - Calculation for the ratio of host to guest.....	132
<b>Appendix D</b> - Comparison of FTIR spectra between guest-free host-SAMs and host-guest assembly with stearic acid. ....	133
<b>Appendix E</b> - The ratio of CC* to total C 1s peak area for host-guest assemblies depending on polarity index of solvents or dielectric constant of solvents.....	134
<b>Appendix F</b> - The results of contact angles of water for host-guest assemblies in different guest molecules in various solvents.....	136
<b>Appendix G</b> - The comparison of the contact angle between guest-free LDSAMs, guest-included LDSAMs, and guest-removed LDSAMs.....	138
<b>Appendix H</b> - The dependence of the frequency shifts on the concentration of solution. ....	139

# List of Figures

Figure 2. 1. Self-assembled monolayer, <a href="http://www.mtl.kyoto-u.ac.jp/groups/sugimura-g/index-E.html">http://www.mtl.kyoto-u.ac.jp/groups/sugimura-g/index-E.html</a> .	7
Figure 2. 2. The structure of $[\text{Ni}(\text{Hbim})_3]^+$ . Six $[\text{Ni}(\text{Hbim})_3]^+$ can form the micro-porous structure with a large channel. * This image was copied from reference 13. ....	10
Figure 2. 3. Supramolecular networks of the large $\text{Zn}^{\text{II}}$ porphyrin complex sustained by multiple hydrogen bonds. * This image was copied from reference 14. ....	11
Figure 2. 4. Packing arrangement of the interdigitated (R-pentadecylmandelic acid, R-phenylethylamine) trilayer. *This image was copied from reference 28. ....	12
Figure 2. 5. Schematic illustration of the density variation across the interface. *This image was copied from reference 42. ....	15
Figure 2. 6. Geometry used for calculation of XRR from a perfect interface between regions having indices of refraction $n_1$ and $n_2$ showing angles of incidence $\theta_i$ and refraction $\theta_r$ . ....	15
Figure 2. 7. A layer of material, thickness $dt$ , at a depth $t$ emits photoelectrons with an intensity $dI$ in a direction parallel to the surface normal. ....	22
Figure 2. 8. Attenuation length as a function of kinetic energy. ....	23
Figure 2. 9. Relative intensity as a function of depth for Si 2p electrons emitted from silicon as a result of Al K $\alpha$ radiation. ....	24
Figure 2. 10. The effect of varying the take-off-angle in XPS. (a) shows detection of photoelectrons normal to the surface. By rotating the sample to glancing angles, as in (b), the escape depth $d$ is reduced and hence the XPS spectra are more surface specific. ....	25
Figure 2. 11. An illustration of the analysis of a thin metal oxide on a metal. The diagrammatic spectra show the effect of the collection angle on the elemental and oxide peaks of the metal. ....	25
Figure 3. 1. II-A isotherms of NaC18S (a) on a pure water subphase and (b) on an aqueous subphase containing 0.025M $\text{G}_2\text{CO}_3$ . The molecular area is $A_{\text{mol}} = 27 \text{ \AA}^2/\text{sulfonate}$ for NaC18S over pure	

water and $\text{Amol} = 44 \text{ \AA}^2/\text{sulfonate}$ for NaC18S over 0.025 M $\text{G}_2\text{CO}_3$ aqueous subphase. ....	36
Figure 3. 2. $\Pi$ -A isotherms for 1:1 mixture of (a) C18S on pure water, and (b) C18S monolayers on an aqueous subphase containing 0.025M $\text{G}_2\text{CO}_3$ with guest molecules, such as C16, C18Br, and C18OH, respectively.....	37
Figure 3. 3. $\Pi$ -A isotherms of (a) C18S on pure water and (G)C18S with (b) guest-free, (c) C16, (d) C18Br, (e) C18OH, and (f) NaphC18 on 0.025M $\text{G}_2\text{CO}_3$ aqueous subphase. The host-guest mixed monolayers at air-aqueous interface are transferred to a clean Si substrate at the surface pressure of $\pi = 20 \text{ mN/m}$ .....	39
Figure 3. 4. The electron density profile and summarized results corresponding to the data fits for (G)C18S guest-free monolayer. (G)C18S guest-free monolayer was compressed to 20 mN/m and then transferred to Si substrate. After LB deposition, samples were placed into hexane for different amount of time. Upon removal from hexane, X-ray reflectivity data was taken of the sample and fitted with two box models to determine the changes in the molecular structure of the film.....	41
Figure 3. 5. Electron density profiles and summarized results corresponding to the data fits for (G)C18S:C18Br monolayer. (G)C18S:C18Br monolayer was compressed to 20 mN/m and then transferred to Si substrate. After LB deposition on Si, samples were placed into pure hexane and cyclohexane solutions for different amount of time. Upon removal from the solution, X-ray reflectivity was taken of the sample and fitted with two box models to determine the changes in the molecular structure of the film.....	43
Figure 3. 6. Electron density profiles and summarized results corresponding to the data fits for (G)C18S:C18OH monolayer. (G)C18S:C18OH monolayer was compressed to 20 mN/m and then transferred to Si substrate. After LB deposition on Si, samples were placed into hexane and cyclohexane solutions for different amount of time. Upon removal from the solution, X-ray reflectivity was taken of the sample and fitted with two box models to determine the changes in the molecular structure of the film.....	45
Figure 3. 7. Electron density profile and summarized result corresponding to the data fits for (G)C18S:NaphC18 monolayer. (G)C18S:NaphC18 monolayer were compressed to 20 mN/m and then transferred to Si substrate. After LB deposition on Si, (G)C18S:NaphC18 monolayers were placed into cyclohexane solutions for different amount of time respectively. Upon removal from the solution, X-ray reflectivity was taken of the sample to determine the changes in the molecular structure of the	

film.....	46
Figure 3. 8. Summarized electron density profiles for (G)C18S-based Langmuir-Blodgett films.....	47
Figure 3. 9. The electron density profiles and summarized results corresponding to the data fits for (G)C18S guest-free monolayers. (G)C18S guest-free monolayer was compressed to 20 mN/m and then transferred onto Si substrate. After LB deposition, samples were placed into two different solutions of CholC18 and NaphC18 in cyclohexane for different amount of time. Upon removal from the solution, X-ray reflectivity was taken of the sample and fitted with two box models to determine the changes in the molecular structure of the film.....	48
Figure 3. 10. The electron density profiles and summarized results corresponding to the data fits for (G)C18S-CholC18. (G)C18S:CholC18 monolayer were compressed to 20 mN/m and then transferred to Si substrate. After LB deposition on Si, (G)C18S:CholC18 monolayers were placed in the naphthyl stearate solution in cyclohexane for different amount of time respectively. Upon removal from the solution, X-ray reflectivity was taken of the sample to determine the changes in the molecular structure of the film.....	49
Figure 4. 1. Schematic illustration of the formation of a low-density self-assembled monolayers (LDSAMs) formed by host-molecules with integral spacer groups.....	56
Figure 4. 2. Schematic of low-density self-assembled host-monolayers on hydroxylated Si (100) substrates. 1A(H,Ph,C10), 1A(Ph,C16), and 1B(Ph,C16) are formed in a one-step process using secondary alcohol and amine precursors. 2B(C16), 3B(C8), 3B(C16), 4B(C14OH), and 4B(C18) are formed in a stepwise fashion by forming a monolayer of the bulky anthracene precursors and then subsequently adding a long alkane tail.....	61
Figure 4. 3. FTIR-ATR spectra for monolayers of (a) triethoxychlorosilane (coupling layer), (b) 1A-H,Ph,C10, and (c) 4B-C18, respectively.....	62
Figure 4. 4. XPS survey spectra for monolayers of (a) pure silicon treated with Piranha solution, (b) triethoxychlorosilane, (c) 1A-H,Ph,C10, (d) 1A-Ph,C16, (e) 1B-Ph,C16, (f) 3B-C16 through grignard reaction, and (g) 4B-C18.....	64
Figure 4. 5. XPS spectra of the Si 2p and the C 1s regions of (a) pure silicon, (b) coupling layer of triethoxychlorosilane, (c) 1B-Ph,C16, (d) 1A-Ph,C16, and (e) 4B-C18.....	66
Figure 4. 6. X-ray reflectivity curves of six different LDSAMs (2A, 1A-H,Ph,C10, 1A-Ph,C16, 1B-	

Ph,C16, 3B-C16, and 4B-C14OH). .....	69
Figure 4. 7. Box model of the normalized electron density of (a) 1A-H,Ph,C10 and (b) 3B-C16 monolayer. The layer thickness estimated was determined to be 11.3 and 19.5 for (a) and (b) respectively.....	69
Figure 4. 8. Schematic drawing of anticipated monolayer structure of (a) 1BPhC16 and (b) 3BC16. The 1BPhC16 monolayer can have a densely-packed structure, whereas low-density SAMs such as 3BC16 allow alkane chains to tilt or bend to fill the cavities. This leads to a decrease in the thickness and the electron density of the films. ....	71
Figure 5. 1. Schematic illustration of host-guest assemblies for functional interfaces: Low-density SAMs provide well-ordered structures with nanometre-scale precision. Externally regulated host-guest interactions allow the versatile functionalization on surfaces via the intercalation of functional guests. ....	77
Figure 5. 2. Schematic illustration of non-covalently bonded host-guest assemblies via intercalation of stearic acid into host-cavities; interactions between host-guest, host-solvent, and guest-solvent are responsible for the formation of host-guest assemblies. ....	78
Figure 5. 3. Surface pressure ( $\pi$ ) - molecular area (A) isotherm for the compression of host molecules at air-aqueous interface. Mean area per molecule (extrapolated to zero pressure) is obtained using 10-octadecyl-9-anthracenethiol solution of 0.1 mg/ml .....	82
Figure 5. 4. Schematic drawing of the model proposed for the ordered structure of 9-mercaptoanthracene (MA) on Au(111), where a, b, and $\alpha$ are approximately 22.5 Å, 12.7 Å, and 51°, respectively. * This image was copied from reference 9. ....	82
Figure 5. 5. Frequency shift (fifth overtone - $\Delta f_5/5$ ) and dissipation shift $\Delta D_5$ ( ) vs time a bare gold crystal (a) and a host-coated crystal (b) exposed to a 25 mM solution of stearic acid in ethanol. (c) Dissipation-Frequency (D-f) plots based on the data of $\Delta f_5/5$ and $\Delta D_5$ . Black arrows indicate break points where the slope changes. After the break point, the direction of arrow 2 for the host-coated sample indicates that there is a loss of mass from host-guest assembly. The shallow slope indicates that the host-guest assembly is rigid. (d) The number of adsorbed guest molecules per area and the calculated thickness of the adsorbed films (further details are given in Table 5.1) .....	84
Figure 5. 6. Schematic drawing of the ordered structure of OAT host-SAMs on Au(111). Considering the	

cross-sectional area of alkane chain ( $21 \text{ \AA}^2$ ), one host molecule in a unit cell is 34-39 $\text{ \AA}^2$ in area.....	87
Figure 5. 7. Frequency shift (fifth overtone - $\Delta f_{5/5}$ ) and dissipation shift ( $\Delta D_5$ ) vs time for a bare gold crystal (a) and a host-coated crystal (b) exposed to a 25 mM solution of naphthyl stearate in ethanol. (c) Dissipation-Frequency (D-F) plots based on the data of $\Delta f_{5/5}$ and $\Delta D_5$ . The arrows indicate break points where the slope changes. The direction of arrow 2 suggests an increase in mass with a corresponding increase in rigidity, i.e., less dissipation per added molecule during the second adsorption phase. (d) The number of adsorbed guest molecules per area and the calculated thickness of the adsorbed films (further details are given in Table 5.2) .....	89
Figure 5. 8. (a) Frequency shift (fifth overtone - $\Delta f_{5/5}$ ) and dissipation shift ( $\Delta D_5$ ) as a function of time for the adsorption of stearic acid (A) followed by naphthyl stearate (B) on host-coated surface. The Dissipation-frequency (D-f) plot for (b) stearic acid and (c) naphthyl stearate. (d) The number of adsorbed guest molecules per area and the calculated thickness of the adsorbed films (further details are given in Table 5.3) .....	91
Figure 5. 9. Kinetically favored intercalation of the prefluoroalkyl end of the alcohols results in a hydrophilic surface substituted with hydroxyl group at early time of the adsorption process. At longer times, thermodynamically preferred intercalation of the alcohol end results in a perfluoroalkane interface. * This image was copied from reference 15.....	92
Figure 5. 10. XPS spectra of (a) blank Au (bottom), (b) host monolayer (middle), and (c) host-guest (stearic acid) assembly (top). The host monolayer and host-guest assembly show sulfur signals in the region of 160 to 170 eV. The reference Au shows no sulfur peak in this region. Note that the molecular structures of host and guest are depicted, respectively.....	94
Figure 5. 11. High resolution C 1s spectra for host-guest assemblies prepared in the guest solution of (a) stearic acid, (b) 2-naphthyl stearate, (c) 1-octadecylamine, and (d) 1-bromooctadecane in benzene, respectively.....	95
Figure 5. 12. High resolution C 1s XPS spectra for (a) blank Au, (b) host SAM, and (c) host-guest assembly with stearic acid on gold surface. The experimental spectra are shown together with curve fittings (solid lines). The vertical lines (red) indicate the position of C=C, C-C, and C-C*, respectively. Note that unbound C-C peaks are observed around 285.6 eV.....	97
Figure 5. 13. High resolution XPS spectra for C 1s for host-guest assembly with (a) stearic acid or (b) naphthyl stearate each. Host-SAMs were immersed in stearic acid solution in various solvent for 12	

hrs. Solid lines indicate deconvoluted peaks for each component. Two vertical lines correspond to the position of C-C* (blue, 285.4 eV) and C-C (red, 284.7 eV), respectively. Red-colored regions in (b) indicates the intensity of C=C (284 eV).....	98
Figure 5. 14. The ratio of the C-C* (alkyl tail of host-guest assembly) to total peak area and calculated thickness for host-guest assemblies with (a) stearic acid and (b) naphthyl stearate in various solvents derived from XPS data. Red horizontal lines are the expected layer thickness for standing-up host monolayer. ....	100
Figure 6. 1. Nanowire-based detection of single viruses. Schematic shows two nanowire devices, 1 and 2, where the nanowires are modified with different antibody receptors. Specific binding of a single virus to the receptors on nanowire 2 produces a conductance change ( <i>Right</i> ) characteristic of the surface charge of the virus only in nanowire 2. When the virus unbinds from the surface the conductance returns to the baseline value. *This image was copied from Patolsky, F. et al. <i>PNAS</i> 2004,101, 14017. ....	108
S 1. LDSAM (1AC16) was immersed in hexadecane solution in different solvents or different guest solution in toluene. ....	109
S 2. LDSAM (3BC16) was immersed in hexadecane solution in different solvents or different guest solution in toluene. ....	110
S 3. Complete XPS data for host-guest assemblies with stearic acid in various solvents. (a) benzene, (b) cyclohexane, (c) dibutyl ether, (d) dichloromethane, (e) ethanol, (f) heptane, and (g) tetrahydrofuran. ....	114
S 4. Complete XPS data for host-guest assemblies with naphthyl stearate in various solvents. (a) benzene, (b) dibutyl ether, (c) dichloromethane, (d) cyclohexane, (e) heptane, (f) tetrahydrofuran, and (g) toluene. ....	117
S 5. Complete XPS data for host-guest assemblies with octadecyl amine in various solvents. (a) benzene, (b) cyclohexane, (c) dibutyl ether, (d) dichloromethane, (e) ethanol, (f) heptane, (g) tetrahydrofuran, and (h) toluene. ....	121
S 6. Complete XPS data for host-guest assemblies with 1-bromooctadecane in various solvents. (a) benzene, (b) cyclohexane, (c) dibutyl ether, (d) dichloromethane, (e) ethanol, (f) heptane, and (g)	

tetrahydrofuran. ....	125
S 7. CC* extraction from the high resolution XPS spectra for C 1s for host-guest assemblies with stearic acid in various solvents. ....	126
S 8. CC* extraction from the high resolution XPS spectra for C 1s for host-guest assemblies with naphthyl stearate in various solvents. ....	127
S 9. CC* extraction from the high resolution XPS spectra for C 1s for host-guest assemblies with octadecyl amine in various solvents. ....	128
S 10. CC* extraction from the high resolution XPS spectra for C 1s for host-guest assemblies with 1-bromooctadecane in various solvents. ....	129
S 11. Summary of XPS data for host-guest assemblies with stearic acid in various solvents: the ratio of CC* to total peak area (red column) and film thickness (green column) ....	130
S 12. Summary of XPS data for host-guest assemblies with naphthyl stearate in various solvents: the ratio of CC* to total peak area (red column) and film thickness (green column) ....	130
S 13. Summary of XPS data for host-guest assemblies with octadecyl amine in various solvents: the ratio of CC* to total peak area (red column) and film thickness (green column) ....	131
S 14. Summary of XPS data for host-guest assemblies with 1-bromooctadecane in various solvents: the ratio of CC* to total peak area (red column) and film thickness (green column) ....	131
S 15. Schematic illustration of host-guest assemblies for stearic acid and naphthyl stearate respectively. 1:1 host-guest assembly for stearic acid and 1:2 host-guest assembly for naphthyl stearate. ....	132
S 16. Comparison of FTIR spectra between guest-free host-SAMs and host-guest assembly with stearic acid. After the formation of host-guest assembly with stearic acid, FTIR spectra show a strong absorption peak at 1730 c m-1 assigning to C=O for carboxylic acid. ....	133
S 17. The ratio of CC* to total C 1s peak area for host-guest assemblies depending on the polarity index of solvents. ....	134
S 18. The ratio of CC* to total C 1s peak area for host-guest assemblies depending on the dielectric constant of solvents. ....	135
S 19. The result of contact angle of water on host-guest assemblies in different guest molecules in various solvents for 12 hrs. ....	137
S 20. The result of contact angle of water for host-guest assembly depending on the time period of immersion in stearic acid solution in ethanol. ....	137

S 21. The comparison of the contact angle between guest-free LDSAMs, guest-included LDSAMs, and guest-removed LDSAMs. Guest-free LDSAMs prepared using anthracene-based thiol host-molecules were immersed in the 1-octadecanol solution in different solvent. Guest-included LDSAMs were then immersed in pure ethanol for 12 hrs and sonicated for 10 min. ....	138
S 22. The dependence of the frequency shifts on the concentration of stearic acid solution. At equilibrium, the frequency shift is close to each other.....	139

# List of Tables

Table 2. 1. Representative functional units introduced in Self-Assembled Monolayers.....	9
Table 4. 1. Peak frequencies of the CH <sub>2</sub> asymmetric and symmetric vibration mode obtained from FTIR-ATR measurement of various LDSAMs. ....	63
Table 4. 2. The surface chemical compositions determined by XPS quantitative analysis of each LDSAMs.....	65
Table 4. 3. Static contact angles, ellipsometric thickness, and thickness and electron density determined from X-ray reflectivity profiles with 2 or 3 boxes model. The thickness of host monolayer is shown in bold.....	71
Table 5. 1. Parameters for stearic acid calculated using the Sauerbrey equation for (a) bare gold and (b) host-coated surface: the adsorbed mass per unit area (cm <sup>2</sup> ), the number of molecule per unit area (nm <sup>2</sup> ), and the thickness (Å) of the monolayer. *The estimated cavity area is approximately 0.34-0.39 nm <sup>2</sup> . ....	86
Table 5. 2. Parameters for naphthyl stearate calculated using the Sauerbrey equation for (a) bare gold and (b) host-coated surface: the adsorbed mass per unit area (cm <sup>2</sup> ), the number of molecule per unit area (nm <sup>2</sup> ), and the layer thickness (Å). * The estimated cavity area is approximately 0.34-0.39 nm <sup>2</sup> . ....	90
Table 5. 3. Parameters for naphthyl stearate calculated using the Sauerbrey equation for (a) bare gold and (b) host-coated surface: the adsorbed mass per unit area (cm <sup>2</sup> ), the number of molecule per unit area (nm <sup>2</sup> ), and the layer thickness (Å). * The estimated cavity area is approximately 0.63 nm <sup>2</sup> . ....	93
Table 5. 4. Characteristic XPS binding energies and relative area of C-C* and C-C for the host-guest assemblies with stearic acid and naphthyl stearate at various solvents, and the proposed CC*/CC ratios. The peak area ratio of the host-guest assemblies to the host monolayer is also listed. The thickness of host-guest assemblies is estimated from the C 1s to Au 4f intensity. ....	101

# Chapter 1

## Introduction

The functionality of surfaces plays an important role in many applications such as catalysis, sensing, and bio-compatibility, which can benefit from distinctive chemical and physical surface properties. Thus, careful design and control of surface properties can be of great interest in materials and surface sciences. SAMs, LB films, and other surface-confined assemblies have long been acknowledged as a practical strategy for creating tailor-made functional surfaces.

Ternary host-guest Langmuir monolayers with inherent inclusion cavities, affording hosts for non-amphiphilic guest molecules, can permit the introduction of various functionalities via the intercalation of guest molecules at air-water interface that otherwise may not be achievable. Unfortunately, these Langmuir-Blodgett films suffer from an inherent lack of stability due to their weak interactions with the solid surface. SAMs are highly desirable for use in a wide range of applications due to the flexibility in design of their molecular structures and properties. For these reasons, SAMs have been widely used to prepare well-defined, stable structures and functional surfaces. The main disadvantage of the SAM method comes from the time-consuming and complex synthesis of the  $\alpha$ - $\omega$  molecules

needed to form functionalized surfaces.

An alternative to  $\alpha\text{-}\omega$  molecules for SAM formation is the use of surface host-guest assemblies. This approach can provide flexibility in tailoring interfaces and the potential ability to regenerate functional surfaces via intercalation of various functional guests. The method can also provide nanometer-scale precision via the well-controlled arrangement of organic molecules on surfaces over an extended length scale. There are two general strategies available for the construction of surface host-guest assemblies. One is to use an ordered array of template molecules on a surface and then add functionality via specific host-guest interactions between the template and a functional guest. The second is to use two-dimensional open structures with well-defined cavities as a template. Functional guest molecules can then be trapped in the repetitive and spatially ordered cavities on the surface. In both cases, host-guest interactions make it possible to add versatile functionalities to the surface via host-guest assembly.

This thesis reports on the development and characterization of host-guest assemblies and the feasibility for alteration and regeneration of surface properties via intercalation of functional guests. The final structure of the thin films is determined by the shape and properties of the molecules that are used. In our work, 2-dimensional host structures with pores were constructed on solid substrates using Langmuir-Blodgett deposition and self-assembly from solution. By adopting the fundamental concept of host-guest interactions from supramolecular chemistry, we hypothesized that structurally homologous guest molecules with attached functional groups could be intercalated into the pores between hydrophobe arrays at the liquid-solid interface under the well-regulated external conditions. This approach offers the potential of separating the functionality of the monolayer surface from the inherent structure of the host.

The work was based on the following primary hypothesis: thin films consisting of alkane chains separated by spacer groups in order to create a low-density framework can be used to intercalate alkane substituted guest molecules from solution, thereby creating functionalized surfaces.

The research goals for the main results chapters are described below:

**Chapter 3:** The structure of guanidinium sulfonate based Langmuir monolayers

formed from alkane sulfonate (anions) amphiphiles and guanidinium cations have been well studied at the air-aqueous interface, however, none of the prior studies of **GS** host-guest monolayers have addressed the structure and properties of the films after transfer to a solid substrate, a necessary step to allow their use in a variety of application. The objectives of the work were to **(1)** investigate the structure of the deposited host-guest assemblies consisting of guanidinium, octadecylsulfonate and various alkane tethered guest molecules; **(2)** to evaluate the stability of the host-guest assemblies under exposure to non-polar organic solvent environments; and **(3)** to study the feasibility of guest insertion and exchange from **GS**-based LB films in order to generate the functional surfaces and regenerate the functionality of surface.

**Chapter 4:** The **GS** based LB films discussed in Chapter 2 exhibited poor stability in most conditions, so we decided to examine low-density host monolayers based on covalently bound self-assembled monolayers (SAMs). The objectives of the work were **(1)** to demonstrate effective methodologies to prepare low-density self-assembled monolayer (LDSAM) system possessing integral ‘spacer’ moieties and reactive groups that bind to a substrate; and **(2)** examine various integral spacer molecules and determine whether they can create low-density structures for the inclusion of complementary guest molecules.

**Chapter 5:** The disadvantage of the formation of host-guest assemblies using LDSAMs is that it is not possible to deposit preformed host-guest assemblies on the surface. Instead self-assembly of the host monolayer must occur in the absence of guest molecules, followed by intercalation of the functional molecule. The objectives of the work were **(1)** to investigate the intercalation processes of guest molecules in host-LDSAMs with well-defined cavities using *in-situ* and *ex-situ* techniques; and **(2)** to demonstrate the feasibility using LDSAMs as host monolayers in order to add functionality to, or to regenerate the functionality of surfaces via the intercalation of functional guests.

The first part of this thesis, **Chapter 2**, provides background on the formation of thin films at interfaces, described prior efforts in host-guest assemblies at surfaces, and provides background into several of the experimental techniques employed in our work. **Chapter 3** investigates host-guest assemblies consisting of **G**, octadecylsulfonate and various alkanes tethered guest molecules formed at the air-aqueous interface and transferred to solid

substrates via the Langmuir-Blodgett technique using grazing-angle incidence X-ray diffraction and specular X-ray reflectivity technique. In particular we examined the stability of the host-guest assemblies and the feasibility of intercalation and exchange of molecular guest under exposure to non-polar organic solvent environments using X-ray reflectivity measurements. **Chapter 4** focuses on the development of low-density self-assembled monolayers (LDSAMs) with built-in spacer groups, such as anthracene-derivatives, that create inclusion cavities. Structural characteristics of the low-density self-assembled monolayers were examined using infrared spectroscopy, X-ray photoelectron spectroscopy (XPS), and X-ray reflectivity (XRR). The potential of LDSAMs for the formation of host-guest assemblies is also described. **Chapter 5** describes a study of the intercalation of several guest molecules into a LDSAM with well-defined cavity from various solvents. The success of guest intercalation or exchange will be determined using *in-situ* quartz crystal microbalance with dissipation (QCM-D) and *ex-situ* X-ray photoelectron spectroscopy (XPS) measurements. We demonstrate the feasibility using LDSAMs as host monolayers in order to add functionality to, or to regenerate the functionality of surfaces via the intercalation of functional guests. **Chapter 6** provides a summary of the work and discusses potential avenues for further investigation and application of the LDSAM systems developed during this work.

The research has resulted in a new, simple method for adding surface functionality to a wide variety of materials and devices. This has the potential to impact a number of areas of current technological and societal interest including: biomaterials engineering and biocompatibility (medical implants and devices); the creation of new catalytic surfaces and particles (environmental remediation, creation of new materials); the separation of chemical and biological components (pharmaceuticals, fine chemicals); and chemical and biological sensing (threat detection, process control, and diagnostics).

# Chapter 2

## Literature Review

### **2.1. Fundamental structure – functional organic molecules**

Molecular devices that are sensitive to external stimuli: light, electricity, magnetism, heat, different molecules, and the like, can manifest diverse functions in the fields of material transport, energy conversion, and sensors. For the fabrication of molecular devices with elemental molecules it is important to understand how to arrange molecules and control their size and shape. Diverse attempts have been made to develop new nano-structured materials as interest in their unique properties has grown. Among the many approaches, a bottom-up method has received attention. The bottom-up method is a self-assembly process via non-covalent bonds that exploits various intermolecular interactions. In particular, tuning of the pattern, directivity, and flexibility of non-covalent bonding makes it possible to control the surface properties, size, dimension, and interior space of nano-structured materials.

### **2.2. Functional organic molecules**

Molecules have different properties depending on their constituent atoms, binding

between molecules, their spatial arrangement, and so on. The synthesis of molecules with diverse and sophisticated forms: basket-like, cylindrical, spherical, and the like, is theoretically possible via a stepwise fashion. Recently it has been noted that non-covalent bonds can be utilized to construct complicated supramolecular structures that otherwise may not be achievable. Thus this approach greatly facilitates the fabrication of multi-functional molecular devices by permitting the design of various modules and the combination of modules in a multitude of different ways.<sup>1</sup>

As mentioned above, material properties rely heavily on molecular shape and structure. Investigation of the correlation between molecular structure and material function provides new insight into molecular design and paves the way for the development of new nano-materials. Organic molecules are ideal components as they have flexibility in structure and diversity in functionality.

### **2.3. Functional monolayers on a surface**

For many years organic molecular films at the nanometer-scale have shown significant technological promise across a wide range of potential applications. They have also provided useful templates for investigating diverse interfacial phenomena with the development of various experimental tools for the elucidation of molecular ordering. In particular, various attempts have been made to control surface properties via the formation of functional films on gold substrate. One approach for the formation of organic functional films is the Langmuir-Blodgett technique. Langmuir-Blodgett films (LB films) are defined as one or more monolayers of water-insoluble amphiphilic molecules deposited from a liquid surface onto a solid substrate. The film obtained can be highly organized and the formation can be controlled to produce anything from a monomolecular film to multilayer structures built up of hundreds of monolayers. Irving Langmuir and Katherine Blodgett founded the science of LB films early in the 20<sup>th</sup> century. Unfortunately, the instability of LB films on antipathic substrates precludes wide application of the technique despite their ability to form highly ordered structures.

Another approach for the formation of organic functional films is molecular self-assembly. Molecular self-assembly is the spontaneous assembly of molecules without extended guidance or management. In 1980, Sagiv reported that aliphatic compounds with trimethoxysilyl or trichlorosilyl formed highly ordered structures on a hydroxylated substrate and their structure had much more affinity with substrate than those obtained using the Langmuir-Blodgett technique.<sup>2</sup> In 1983, Allara discovered that alkanethiols formed highly oriented structures on Au. After the discovery of the formation of crystalline-like monolayers on metal surfaces, self-assembled monolayers (SAMs) have received significant research attention.

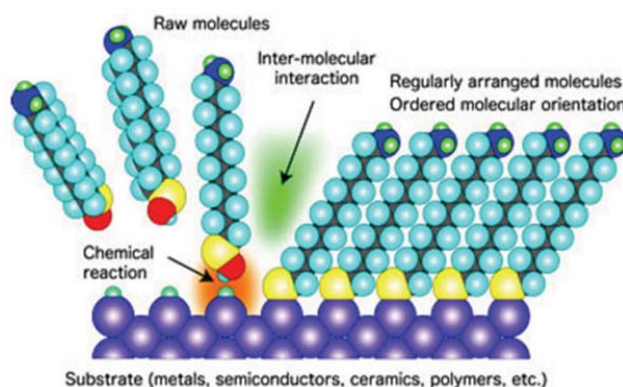


**Figure 2. 1.** Self-assembled monolayer, <http://www.mtl.kyoto-u.ac.jp/groups/sugimura-g/index-E.html>

A molecule for self-assembly can be thought of as containing 3 parts: a binding group for attachment to surface, a spacer chain (typically composed of methylene group), and a functional head group. The binding groups, such as thiol or silane, and the spacer groups,  $(\text{CH}_2)_n$ , act as the main driving forces for molecular assembly. The head group provides a platform where any desired group can be used to produce surfaces of any type of chemistry. By simply changing the head group, thus surface can be created to be hydrophobic, hydrophilic, protein resistant, or allow further chemical binding. This work, thus, enables a researcher to design a surface to serve any desired function.<sup>3</sup>

### 2.3.1. Functional monolayers on Au

Sulfur has a strong affinity for the gold surface. Researchers have found that the sulfur-gold interaction is on the order of 45 kcal/mol,<sup>4</sup> forming a stable, semi-covalent bond. Recent studies of thiol-based SAMs demonstrated that various binding group: disulfide, selenol, and isocyano, can be utilized on Au.<sup>5</sup> In addition, SAMs can be prepared on various surfaces ranging from metals to semiconductor.<sup>6</sup> Various techniques: contact angle measurement, ellipsometry, scanning tunneling microscopy, electrochemical measurement, X-ray photoelectron spectroscopy, infrared and Raman spectroscopy, have characterized those thiol-based SAMs.

As mentioned above, tailoring surface properties became possible via incorporation of wide range of functional units within these alkanethiol SAMs on Au surface. By substituting terminal methyl group with carboxylic or hydroxyl group, for example, hydrophobic surface can be tuned to hydrophilic one. Besides, terminally-introduced reactive groups enable to construct complex structures and immobilize metallic particle or functional polymeric material on Au surface. In this way thiol-based SAMs have been utilized for studies and applications in many areas, e.g., catalyst,<sup>7</sup> charge transfer, redox reaction,<sup>8,9</sup> luminescence,<sup>10</sup> molecular recognition via host-guest interaction,<sup>11</sup> and so on. The significant functional units introduced in SAMs are summarized in Table 1.1.

### 2.3.2 Functional Monolayer on Silicon

As was the case in the thiol-based SAMs, silane-based molecules for functional SAMs can be synthesized via  $\omega$ -substitution of alkyltrichloro- and alkyltrialkoxo-silanes with terminal functional units. However, the synthesis of functional organosilane compounds is restricted as functional groups incorporated into organosilane molecule should be unreactive toward trichlorosilyl or trialkoxysilyl groups. Thus few researches for functionalization of silicon surface via the formation of SAMs has been reported, while the mechanism of self-assembly of organosiloxane compounds and the structure of silane-based SAMs have been

well studied and elucidated.

**Table 2. 1.** Representative functional units introduced in Self-Assembled Monolayers

Function	Functional group
Electrochemical	Ferrocene, quinine, Ru[(NH <sub>3</sub> ) <sub>6</sub> <sup>2+</sup> ]
Photochemical	Porphyrin, Ru[(bpy) <sub>3</sub> <sup>2+</sup> ]
Catalytic	Ferrocene, Ni(cyclam), metal porphyrin
SHG (second harmonic generation)	Ferrocenyl nitro phenyl ethylene
Sensor	Quinone, cyclodextrine, enzymes
Structural isomerization	Azobenzene, spiropyrans
Mediator	Ferrocene, pyridine
Hydrophilic, hydrophobic	Carboxylic, hydroxyl, sulfonic, methyl
Combinative	Carboxylic, amine, phosphoric, thiol

## 2.4. Low-density LB films based on H-bonded network

Molecules in crystalline solids arrange in a regular order with close packing and minimal voids. Some molecules, however, cannot pack closely but tend to attain close packing by interpenetration or by adopting different molecules in the voids, which is known as host-guest inclusion compounds. The host-guest compounds are broadly categorized into cavitands, molecular host compounds with intra-molecular cavities and clathrate compounds with extra-molecular cavities that result from the aggregation of two or more molecules. In both categories host and guest molecules are connected via non-covalent interactions. Discoveries of inclusion compounds were made during crystallization from various solvents. In some instances, the solvent used in crystallization was entrapped into the crystal lattice of a substance. The presence of solvent molecules in the crystal lattice conferred unique physical properties to the solvate form.<sup>12</sup> For example, solubility and dissolution rates of a solvate are different from those of the corresponding anhydrate and can result in differences

in properties. Hence, the study of crystallization in various conditions and the resultant solid phase has been critical for understanding molecular arrangements in crystals.

Since the initial discoveries and structural determinations of the earliest inclusion compounds, a great deal of effort has been directed toward the design of open host frameworks capable of including molecular guests. Particularly, interests in host compounds with open molecular frameworks and their associated guests have been driven by developments in the synthesis and application of inorganic zeolites capable of accommodating organic compounds with suitable size and functionality. The shape and size of void supplied by inorganic porous materials are, however, determined by rigid frameworks that are not readily amenable to the precise chemical modification required for many applications. Hence the interest toward organic molecular analogs of inorganic porous frameworks has emerged in that the structure of organic host frameworks and their properties can be altered at the molecular level via synthetic organic chemistry. This modular strategy is based on molecular building blocks that assemble into supramolecular motifs via directional non-covalent bonding.

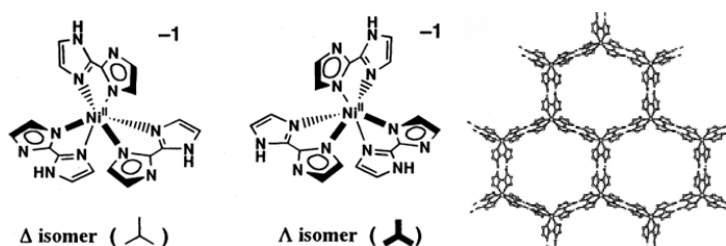


**Figure 2. 2.** The structure of [Ni(Hbim)<sub>3</sub>]<sup>-</sup>. Six [Ni(Hbim)<sub>3</sub>]<sup>-</sup> can form the micro-porous structure with a large channel. \* This image was copied from reference **13**.

Large porous or channel structure can be generated under the presence of large counter-ions. One such example involves the cryptand- or crown-encapsulated potassium salts of octahedral [Ni(Hbim)<sub>3</sub>]<sup>-</sup>. The pseudo-hexagonal networks leave a large amount of space, created via self-complementary HBim hydrogen bonds.<sup>13</sup> Another 2-dimensional host framework is the host system of porphyrins containing peripheral hydrogen bonding substituent. Zn(II) porphyrin complexes have been synthesized by Goldberg<sup>14</sup> that include carboxylic acid, carboxamide, and diaminotriazine-substituted porphyrins.<sup>15,16,17,18</sup>

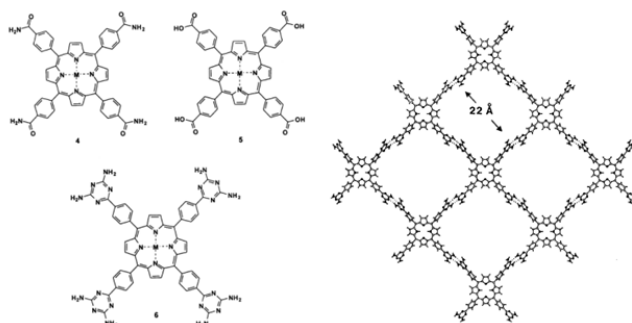


**Figure 2. 3.** Supramolecular networks of the large Zn<sup>II</sup> porphyrin complex sustained by multiple hydrogen bonds. \* This image was copied from reference 14.

Structurally dependable porous host-framework allows crystalline structure to separate from functions that guests included may introduce and thus such host-guest compounds can be inherently versatile.<sup>19</sup> The diversity of host-guest compounds for materials applications has been established via the demonstration of porosity,<sup>20</sup> magnetic behavior,<sup>21</sup> nonlinear optical effects,<sup>22</sup> chemical storage,<sup>23</sup> catalysis,<sup>24</sup> etc. However, the open host-frameworks confront structural disruption as weak long-range interaction between building components precludes molecular assembly from maintaining its solid state.<sup>25,26</sup> In many such cases, the molecular assembly is only host-host frameworks, i.e., it is closely packed and does not provide enough space for guest inclusion. Hence, the guest molecules are co-crystallized parallel to the crystal growth, otherwise the structure will collapse for energetic reasons.<sup>27</sup> In addition, it is not straightforward to chemically alter building components of molecular assembly as minor alternation involves the disruption of fundamental structure for guest inclusion. Consequently, the application of open host-framework via systematic modification of molecular components is considerably limited.

The design of robust molecular hosts facilitates the modification of inclusive framework, thereby stabilizing the assembly of molecules into larger structure. One reliable suggestion for the construction of crystalline structure is to regulate the assembly process at air-solution interface via strong directional interaction based on a robust hydrogen-bonded structural motif: its shape and dimensionality allow the construction of diverse H-bonded framework. Such framework interconnected via strong H-bonding can have high modifiability and flexibility.<sup>28</sup> Thin interdigitated film proposed by Kuzmenko et al. has

been extended to other two-component system of water-insoluble amphiphiles and water-soluble counterparts.

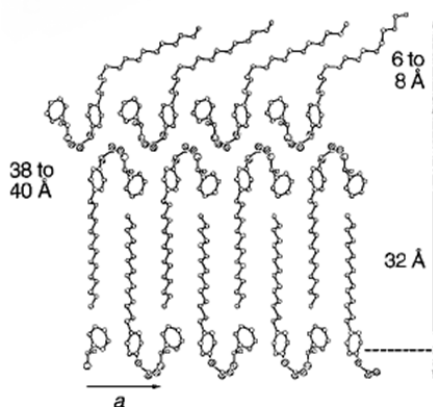


**Figure 2. 4.** Packing arrangement of the interdigitated (R-pentadecylmandelic acid, R-phenylethylamine) trilayer. \*This image was copied from reference **28**.

Based on above observations, further studies have shown that amphiphiles capable of binding water-soluble guest molecule together at air-aqueous interface are able to form host-guest compounds. An amphiphile containing cholesterol hydrophobe and water-soluble chiral amino acid affords a crystalline monolayer structure, which exhibits host-like property: cholesterol hydrophobes create low-density lattice via selective incorporation of amino acid from aqueous subphase.<sup>29</sup> Another interdigitated molecular system has been obtained upon deposition of organosulfonate amphiphile over an aqueous subphase containing guanidinium, studied by Ward and co-worker.<sup>30,31</sup> This acid-base system allows the intercalation of the guanidinium  $[C(NH_2)_3^+]$  cations between the octadecanesulfonate  $[(C_{18}H_{37}SO_3)^-]$  anions into a 2-dimensional hydrogen-bonded network.<sup>32</sup> This interdigitated molecular system suggests that monomolecular film equipped with spacer molecules at the air-aqueous interface can have inherent inclusion cavities between pre-expanded hydrophobe arrays, affording hosts for non-amphiphilic guest molecules and generating two-dimensional inclusion compounds at the air-aqueous interface. Plaut et al suggest that guest intercalation in this fashion can permit the introduction of functionality that otherwise may not achievable at air-aqueous interface.<sup>33</sup>

## 2.5. Low-density SAMs

The functionality of surfaces plays an important role in many applications such as catalysis, sensing, and bio-compatibility,<sup>34</sup> which can benefit from distinctive chemical and physical surface properties. Thus, careful design and control of surface properties can be of great interest in materials and surface sciences. Self-assembled monolayers (SAMs), Langmuir-Blodgett films, and other surface-confined assemblies have long been acknowledged as a practical strategy for creating tailor-made functional surfaces. Ternary host-guest Langmuir monolayers with inherent inclusion cavities, affording hosts for non-amphiphilic guest molecules, can permit the introduction of various functionalities via the intercalation of guest molecules at air-water interface that otherwise may not be achievable, notwithstanding their instability.<sup>35</sup> SAMs are highly desirable methods for use in a wide range of applications due to the flexibility in designing their molecular structures and properties. For these reasons, SAMs have been widely used to prepare well-defined, stable structure and functional surfaces. Considering time-consuming and complex synthesis of  $\alpha$ - $\omega$  molecules, however, this approach has a restricted extension in many cases.

As an alternative to satisfy the requirements of expandability and stability, surface host-guest assemblies have attracted a lot of research interest. This approach can provide not only a high flexibility to tailor interfaces and regenerate new functional surfaces via the intercalation of various functional guests but also the nanometer-scale precision via well-controlled arrangement of organic molecules on surfaces over an extended length scale.<sup>36</sup> There are two general strategies available for the construction of surface host-guest assemblies. One is to use an ordered array of template molecules obtained on surfaces and then fabricate functional structure via specific host-guest interactions between the template and functional guest. Another way is to use two-dimensional open structures with defined size as template. Functional guest molecules can then be trapped in repetitive and spatially ordered cavities on surfaces. In both cases, host-guest interactions make it possible to add versatile functionalities to the surface with host-guest assembly.<sup>37,38,39,40</sup> In particular, two-

dimensional porous structures at a surface can be generated by means of several types of supra-molecular interactions: hydrogen bond-directed homo- and hetero-assembly of organic molecules, the coordination of metal centres to organic ligands, dipole-dipole, van der Waals, or a combination of several interactions.<sup>41</sup>

## 2.6. Surface characterization

### 2.6.1. Specular X-ray Reflectivity<sup>42</sup>

Specular X-ray reflectivity (XRR) is an X-ray scattering techniques for characterizing thin-film structure that can measure film thickness, electron density, and interface roughness. This technique has the virtues of high spatial sensitivity, high penetration, straightforward analysis and simple sample preparation. In XRR, the reflected intensity of X-rays from an interface is measured as a function of the angle,  $\theta$ , of the incident X-ray beam, which is related to the  $z$  component of the wavevector transfer ( $q_z = 2k \sin \alpha$ , where  $\mathbf{k}$  is the wavevector). The magnitude of  $\mathbf{k}$  defines the length-scale of the measurement, ranging from atomic dimensions for large  $\mathbf{k}$  ( $\geq 2\pi/a$ , where  $\mathbf{a}$  is a lattice parameter) to mesoscopic dimensions (1 to 100 nm) for smaller  $\mathbf{k}$ . The direction of  $\mathbf{k}$  with respect to the sample surface determines the direction where structural information is obtained. For specular X-ray reflectivity techniques, the incident angle is equal to the outgoing angle so that  $\mathbf{k}$  is oriented for probing the electron density distribution normal to the surface of thin films at interfaces (Figure 2.5.).

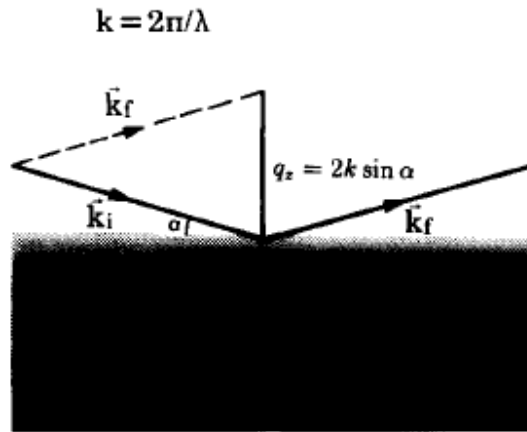


**Figure 2. 5.** Schematic illustration of the density variation across the interface. \*This image was copied from reference 42.

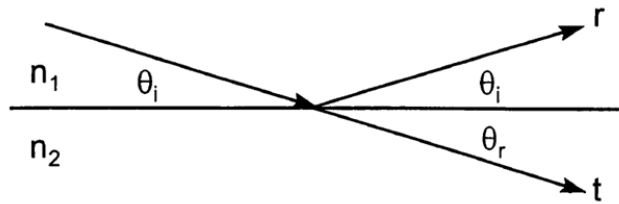


**Figure 2. 6.** Geometry used for calculation of XRR from a perfect interface between regions having indices of refraction  $n_1$  and  $n_2$  showing angles of incidence  $\theta_i$  and refraction  $\theta_r$ .

The amplitude of the transmitted and reflected wave relative to the incident amplitude are given by the Fresnel equations:

$$r_s = \frac{n_1 \sin(\theta_i) - n_2 \sin(\theta_r)}{n_1 \sin(\theta_i) + n_2 \sin(\theta_r)}$$

$$r_p = \frac{n_2 \sin(\theta_i) - n_1 \sin(\theta_r)}{n_2 \sin(\theta_i) + n_1 \sin(\theta_r)}$$

The relationship between the angles defining the incident and outgoing wave vectors is given by Snell's law:

$$\frac{\cos(\theta_i)}{\cos(\theta_r)} = \frac{n_2}{n_1}$$

The index of refraction for X-rays can be obtained from the classical theory of

dispersion, which treats the electron as a mass bound to the atom by a spring with a resonant frequency  $\omega_0$ . When exposed to an incident electromagnetic field of frequency  $\omega$ , the electron oscillates and gives rise to a scattered wave. Relating the induced field to the incident field allows us to determine the dielectric constant of a bound electron, and from that, the index of refraction,  $n$ :

$$n = 1 - \frac{2\pi\rho_{el}e^2}{m\omega^2}f$$

where  $\rho_{el}$  is the electron density of the medium,  $e$  and  $m$  are the electron charge and mass, and  $f$  is the scattering factor of the atom, defined as the ratio of scattering from the bound electron to that of a free electron under the same conditions. In general,  $f$  is complex

$$f = f_0 + \Delta f' + i\Delta f''$$

where  $f_0 + \Delta f'$  and  $\Delta f''$  are the real and imaginary part of  $f$ . For the small angles used in XRR,  $f_0$  is approximately equal to the atomic number  $Z$ . The parameters and are often called the real and imaginary parts of the anomalous absorption. Then,  $n$  is expressed as

$$n = 1 - \delta - i\beta$$

where

$$\delta = \frac{2\pi\rho_{el}e^2}{m\omega^2}(f_0 + \Delta f') \quad \text{and} \quad \beta = \frac{2\pi\rho_{el}e^2}{m\omega^2}\Delta f''$$

The imaginary part of  $n$  is related to the linear absorption coefficient,  $\mu$ , by

$$\mu = \frac{2\omega\beta}{c} = \frac{4\pi\rho_{el}e^2}{mc\omega}\Delta f''$$

The magnitude of  $\delta$  and  $\beta$  are related to the electron density of the material, and are on the order of  $10^{-5}$  and  $10^{-7}$ , respectively.

Since the real part of  $n$  is less than 1 for most materials in the X-ray regime, a wave passing from vacuum into the material will be refracted with an angle less than the angle of incidence. Below some critical value of the incidence angle,  $\theta_c$ , defined by

$$\cos(\theta_c) = n_2/n_1$$

there are no propagating solutions for the transmitted beam so that the incident wave vector is said to exhibit *total external reflection*. Since  $\theta_c$  is small, the cosine can be expanded to second order in  $\theta$ , and one can show that

$$\theta_c = (2\delta)^{1/2}$$

and from the relationship given by Snell's law

$$\theta_i^2 = \theta_r^2 + \theta_c^2$$

For typical X-ray energies of ~5-10 keV, the critical angle is in the range of 0.1°-0.6° for most materials, and depends on the electron density. For values of  $\theta$  near  $\theta_c$  the Fresnel reflection coefficients can be approximated by

$$r_s = \frac{\theta_i - \theta_r}{\theta_i + \theta_r}, \quad r_p = \frac{\theta_r - \theta_i}{\theta_i + \theta_r}$$

and for  $\theta > \theta_c$ , the reflectivity reduces to the simple asymptotic form

$$R = r^2 \approx \left(\frac{2\theta}{\theta_c}\right)^{-4}$$

In order to show the dependence of the reflectivity on angle and energy, the reflectivity is expressed as a function of scattering vector,  $\mathbf{k}$ :

$$R \approx \left(\frac{2k}{k_c}\right)^{-4}$$

where  $k = 4\pi/\lambda \sin(\theta)$  and  $k_c = 4\pi/\lambda \sin(\theta_c)$ . The reflectivity for an ideal surface given above is called the Fresnel reflectivity.

Als-Nielsen developed the diffraction approach consisting of partitioning the structure into infinitesimal layers and superimposing the reflectivity from each slice to obtain the full reflectivity. Als-Nielsen gives the reflectivity from non-ideal surfaces as:

$$R(\mathbf{k}) = R_F(\mathbf{k}) \left| \int \frac{d\rho}{dz} e^{ikz} dz \right|^2$$

where  $d\rho/dz$  is the electron density gradient normal to the surface.

It is convenient to model the in-plane averaged electron density of a simple surface by a Gaussian smeared step from  $\rho = 0$  to  $\rho = \rho_\infty$ .

$$\rho(z) = \frac{\rho_\infty}{2} \left[ 1 + \operatorname{erf} \left[ \frac{z}{2\sigma} \right] \right]$$

The average normal derivative is given by the Gaussian form

$$\frac{d\rho}{dz} = \rho_\infty \frac{1}{(2\pi\sigma^2)^{1/2}} e^{-z^2/2\sigma^2}$$

Where  $\sigma$ , the root-mean-square average of the surface width, result from both the intrinsic width of the interface and the mean-square average of the roughness of the surface. The Fourier transform then yields

$$R(k) = R_F(k) e^{-\sigma^2 k^2/2}$$

The parameters can be determined from XRR spectra: layer thickness ( $d$ ), surface roughness ( $\sigma_s$ ), interface roughness ( $\sigma_i$ ), and average layer density ( $\rho$ ). These parameters are obtained by fitting the spectra to calculations of different model structures and optimizing by least-squares minimization to obtain a set of best-fit parameters. Two layer films are routinely analyzed, and more complex structures can be measured and calculated. However, as the number of layers increases, the difficulty of obtaining a unique set of parameters by fitting increases significantly.

### 2.6.2. Quartz Crystal Microbalance<sup>43</sup>

A quartz-crystal microbalance (QCM) is an extremely useful technique to directly study quantitative kinetics of molecular adsorption by measuring the in situ resonance frequency change due to changes in mass on the electrode at the nano-gram level in both air<sup>44,45</sup> and solution phases.<sup>46,47</sup> The mass change on surface of the quartz crystal is calculated through the relationship between mass changes and frequency changes, given by Sauerbrey.<sup>48</sup>

$$\Delta f = -2f_0^2(\mu_q\rho_q)^{-1/2}\Delta m/A \quad (1)$$

where  $\Delta f$  is the measured frequency shift,  $f_0$  is the frequency of the quartz crystal before a mass change,  $\Delta m$  is the mass change,  $A$  is the piezo-electrically active area,  $\rho_q$  is the density of the quartz ( $=2.648 \text{ g/cm}^3$ ), and  $\mu_q$  is the shear modulus ( $=2.947 \times 10^{11} \text{ gcm}^{-1}\text{s}^{-2}$ ). Hence, the frequency shift is directly proportional to the adsorbed mass on the surface of QCM electrodes. The Sauerbrey equation assumes that acoustic impedance is identical for the film and quartz and that the frequency shift resulting from a mass deposited at some radial distance from the center of crystal will be the same regardless of the radial distance. The negative sign in Eq. (1) indicates that addition of mass to the resonator results in a decrease in its resonant frequency and vice versa. Equation (1) is frequently presented in the following form:

$$\Delta f = -C_f\Delta m \quad (2)$$

where  $C_f=17.7 \text{ ng}\cdot\text{Hz}^{-1}\cdot\text{cm}^{-2}$  for a 5 MHz quartz crystal. When mass is deposited or removed, this linear relationship very accurately describes the frequency change for very small mass loading. When the layer is thick, Eq. (2) is no longer linear and corrections for this case have been developed. In Eq. (2) it is assumed that the added mass is evenly distributed over the electrode and that the mass is rigidly attached to the electrode, with no slip or deformation to the oscillatory motion. It is also possible to get an estimation of the thickness ( $d$ ) of the adhering layer:

$$d_{\text{eff}} = \Delta m/\rho_{\text{eff}} \quad (3)$$

When the QCM crystal is transferred from air into the solution, the shear wave damping occurs, causing large changes in resonant frequency. Kanazawa and Gordon provided an equation that the frequency change induced by immersion in a solution is related to the density  $\rho_L$  and viscosity  $\eta_L$  of that solution:

$$\Delta f = -f_0^{\frac{3}{2}}(\eta_L\rho_L/\pi\mu_q\rho_q)^{1/2} \quad (4)$$

In most situations the adsorbed film is not rigid and the Sauerbrey relation becomes invalid. A film that is soft will not fully couple to the oscillation of the crystal; hence the Sauerbrey relation will underestimate the mass at the surface. A soft film dampens the crystal's oscillation. The damping or energy dissipation (**D**) of the crystal's oscillation reveals the film's viscoelasticity. D is defined as follows:

$$D = E_{\text{lost}} / 2\pi E_{\text{stored}} \quad (5)$$

where  $E_{\text{lost}}$  is the energy lost during oscillation cycle and  $E_{\text{stored}}$  is the total energy stored in the oscillator. The energy lost of the crystal is measured by recording the response of a freely oscillating sensor that has been vibrated at its resonance frequency. This gives the chance to jump between the fundamental frequency and overtones. By measuring at multiple frequencies and applying a viscoelastic model, the adhering film can be characterized in detail; viscosity, elasticity and correct thickness may be extracted. For viscoelastic film, Reed et al.<sup>49</sup> derived Eq. (6) for the case when both the shear modulus and the viscosity of the film are taken into account:

$$\Delta f = -2f_0^2 / (\rho_q \mu_q)^{1/2} [(\Delta m/A) + \{\Delta(\eta_L \rho_L)^{1/2} / (4\pi f_0)^{1/2}\}] \quad (6)$$

The resonant frequency change of the shear vibration of a quartz crystal with the piezoelectrically active area  $A$  characterized by a shear modulus  $\mu_q$ , a density  $\rho_q$ , and the resonant frequency  $f_0$  in contact with a liquid of density  $\rho_L$  and viscosity  $\eta_L$  not only is affected by rigid mass changes  $\Delta m$  but also viscosity change  $\eta_L \rho_L$  in the interface. When a transversal velocity of the quartz surface is equal to the adjacent liquid layer, non-slip boundary conditions can be assumed. In such a case, a viscous penetration depth is proportional to the viscosity, because liquid films show no elasticity. The mass of this liquid layer with a thickness equal to the thickness of the decay layer of the acoustic wave  $\delta$ ;

$$\delta = (2\eta_L / \omega \rho_L)^{1/2} \quad (7)$$

where  $\omega$  is the angular frequency of the thickness shear mode vibrations of the piezoid and causes the vibrating mass to increase and the resonant frequency to decrease.<sup>50</sup> The resonant

resistance change of the crystal, on the other hand, is solely determined by the viscosity change,  $\Delta(\eta_L\rho_L)^{1/2}$  and allows one to discriminate between viscosity and mass change.<sup>51</sup> Reed et al. presented a general model of the viscoelastic over-layer from which limiting cases should be retrievable. Their expression for the electrical admittance agrees exactly with that obtained by Benes.<sup>52</sup>

### **2.6.3. X-ray Photoelectron Spectroscopy<sup>53</sup>**

Of all the contemporary surface characterization methods, X-ray Photoelectron Spectroscopy (XPS), also called electron spectroscopy for chemical analysis (ESCA), is the most widely used technique. The popularity of XPS as a surface analysis technique is attributed to its high information content, its flexibility in addressing a wide variety of samples, and its sound theoretical basis.

Using angle resolved XPS (ARXPS), it is possible to characterize ultra-thin films without sputtering. In most cases, ARXPS can be considered to be a non-destructive technique. It therefore has the potential to probe sub-surface chemical states that would be destroyed by sputtering. From ARXPS data, it is possible to calculate the thickness and depth of ultra-thin layers and to construct a concentration depth profile. The technique relies upon the fact that the information depth of XPS is less than 10 nm, depending upon the material and the kinetic energy of the electron being measured.

There are two important quantities in ARXPS, the inelastic mean free path (IMFP) and the attenuation length (AL). The inelastic mean free path is the average distance an electron travels between successive inelastic collisions. An electron may undergo elastic collisions between inelastic events and so trajectory between the events may not be a straight line. The attenuation length can be applied to any radiation passing through any material. Essentially, it is a measure of the transparency of the material to the radiation. There is a quantity,  $\mu$ , the attenuation coefficient, which describes the proportion of the radiation removed as it passes through a thickness  $\Delta x$  of the material. This is defined as:

$$\mu = \lim_{\Delta x \rightarrow 0} \frac{1 - (I/I_0)}{\Delta x}$$

where  $I_0$  and  $I$  are the intensities of the incident and emergent radiation respectively. The reciprocal of this term is known as the attenuation length,  $\lambda$ :

$$\lambda = 1/\mu$$

In many cases this leads to an equation of the general form:

$$I/I_0 = \exp(-\Delta x/\lambda)$$

This can be applied to XPS where electrons of a given energy are considered as they pass through a material. If the intensity of the electron flux in a given material is measured in a particular direction, then the intensity is affected by both elastic and inelastic collisions. Only electrons which have not been scattered or which have been scattered elastically can contribute to the intensity of a photoelectron peak. Under these conditions, the IMFP is a constant term but AL can change with angle. It is, however, the attenuation length that must be used in equations similar to that shown above.

There is a layer of material of thickness  $dt$  at a depth  $t$ , as shown in Figure 2.7.

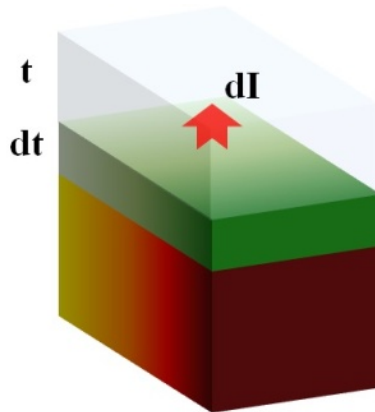


**Figure 2. 7.** A layer of material, thickness  $dt$ , at a depth  $t$  emits photoelectrons with an intensity  $dI$  in a direction parallel to the surface normal.

The photoelectron intensity emitted from this layer ( $dI$ ) in a direction parallel to the

surface normal is:

$$dI = Cdt$$

where  $C$  is constant involving X-ray flux density, sensitivity factors, geometric factors etc. Using the Beer-Lambert law the intensity reaching the surface from this thin layer parallel to the surface normal will be:

$$dI = C \exp(-t/\lambda) dt \quad (1)$$

Integrating between zero and infinity, this becomes

$$I = C\lambda$$

By letting  $C\lambda = I^\infty$  and integrating above equation between  $t$  and infinity:

$$I = I^\infty \exp(-t/\lambda) \quad (2)$$

where  $I$  is the photoelectron signal coming from all depths greater than  $t$ . This equation assumes emission at an angle normal to the surface.

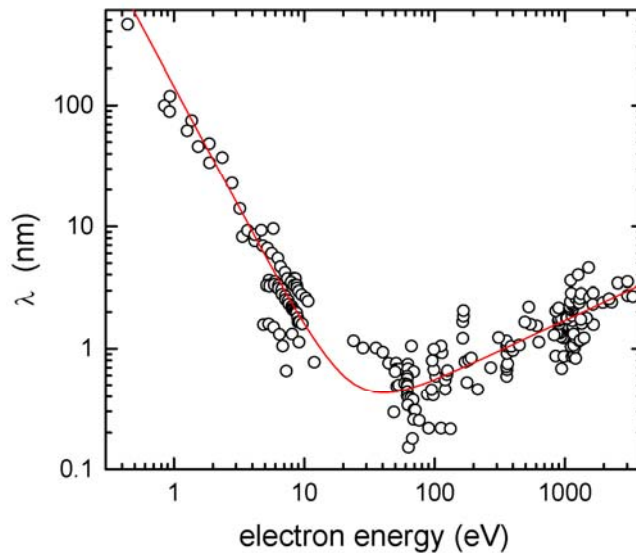


**Figure 2. 8.** Attenuation length as a function of kinetic energy.

The attenuation length for electrons varies with their kinetic energy, as shown in Figure 2.8. The attenuation length increases with increasing kinetic energy in the energy range of interest in XPS (above a few tens of electron volts). Figure 2.9 shows a plot of intensity of a photoelectron peak as a function of depth by considering electrons that emerge parallel to the sample normal. About 65% of the signal in electron spectroscopy will emanate from a depth of less than  $\lambda$ , 85% from a depth of less than  $2\lambda$ , and 95% from a depth of less than  $3\lambda$ .

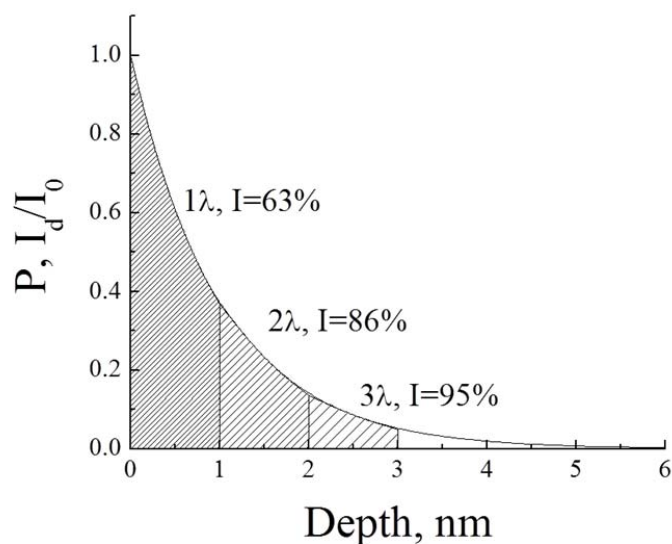


**Figure 2. 9.** Relative intensity as a function of depth for Si 2p electrons emitted from silicon as a result of Al K $\alpha$  radiation.

If electrons are collected at angles other than  $0^\circ$  with respect to the surface normal, these depth are decreased by a factor of  $\sin\theta$ , as can be seen in Figure 2.10. Equation (2) above becomes:

$$I = I^\infty \exp(-d/\lambda \sin\theta)$$

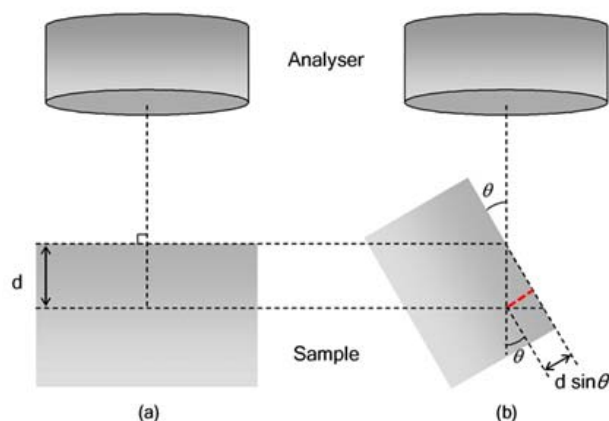


**Figure 2. 10.** The effect of varying the take-off-angle in XPS. (a) shows detection of photoelectrons normal to the surface. By rotating the sample to glancing angles, as in (b), the escape depth  $d$  is reduced and hence the XPS spectra are more surface specific.

If XPS signal is collected over a range of angles from near normal emission to near grazing emission then the analysis depth changes. Figure 2.11 shows schematically the analysis of a thin metal oxide on a metal substrate. In this example, XPS data are collected from the metal at two angles, near normal (bulk angle) and near grazing (surface angle). Near normal emission produces a spectrum in which the metal peak dominates while the oxide peak dominates in the spectrum from the grazing emission. This is the basis for angle resolved XPS measurements.

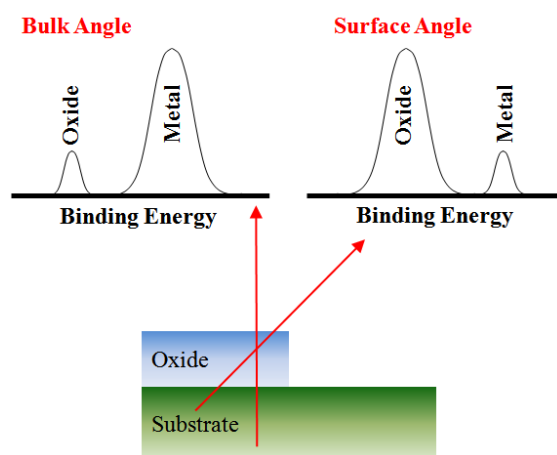


**Figure 2. 11.** An illustration of the analysis of a thin metal oxide on a metal. The diagrammatic spectra show the effect of the collection angle on the elemental and oxide

peaks of the metal.

ARXPS can be used quantitatively to measure layer thickness. Consider a thin layer, thickness  $d$ , of material A on a substrate B. To obtain an expression for the signal from A, equation (1) must be integrated between 0 and  $d$  and becomes:

$$I_A = I_A^\infty [1 - \exp(-d/\lambda_{AA}\sin\theta)]$$

The signal from B arriving at the B-A interface is  $I_B^\infty$ , assuming layer B is thick in comparison with  $\lambda_{BB}$ . This signal is then attenuated by passing through layer A. The signal emerging is therefore given by:

$$I_B = I_B^\infty \exp(-d/\lambda_{BA}\sin\theta)$$

The term  $\lambda_{BA}$  is the attenuation length in layer A for electrons emitted from layer B. Taking the ratio of these signals:

$$\frac{I_A}{I_B} = R = R^\infty \frac{1 - e^{-d/\lambda_{AA}\sin\theta}}{e^{-d/\lambda_{BA}\sin\theta}}$$

where  $R^\infty = I_A^\infty/I_B^\infty$ .

## 2.7. References

- 
- <sup>1</sup> Lehn, J. M. *Supramolecular chemistry: Concepts and Perspective*, VCH, **1995**
  - <sup>2</sup> Sagiv, J. *J. Am. Chem. Soc.* **1980**, *102*, 92
  - <sup>3</sup> Boeckl, M.; Graham, D. *Material Matters* **2006**, *1*, 3
  - <sup>4</sup> Dubois, L. H.; Nuzzo, R. G. *Annu. Rev. Phys. Chem.* 1992, *43*, 437
  - <sup>5</sup> Love, J. C.; Estroff, L. A.; Kriebel, J. K.; Nuzzo, R. G.; Whitesides, G. M. *Chem. Rev.* **2005**, *105*, 1103
  - <sup>6</sup> Buriak, J. M. *Chem. Rev.* **2002**, *102*, 1271
  - <sup>7</sup> Sato, Y.; Itoigawa, H.; Uosaki, K. *Bull. Chem. Soc. Jpn.* **1993**, *66*, 1032
  - <sup>8</sup> Chidsey, C. E. D.; Bertozzi, C. R.; Putvinski, T. M.; Mujisce, A. M. *J. Am. Chem. Soc.* **1990**, *112*, 4301
  - <sup>9</sup> Cooke, G. *Angew. Chem. Int. Ed.* **2003**, *42*, 4860
  - <sup>10</sup> Sato, Y.; Uosaki, K. *J. Electroanal. Chem.* **1995**, *384*, 57
  - <sup>11</sup> Ye, S.; Sato, Yashiro, A.; Sato, Y.; Uosaki, K. *J. Chem. Soc., Faraday Trans.* **1996**, *92*,

3813

- <sup>12</sup> Kumar, T. L.; Guleria, P.; Vishweshwar, P.; Sivalakshmidēvi, A.; Babu, J. M.; Vyas, K.; Acharyulu, P. V. R.; Sekhar, N. M.; Kumar, B. S. *J. Incl. Phenom. Macrocycl. Chem.* **2010**, *66*, 261
- <sup>13</sup> Tadokoro, M.; Nakasuji, K. *Coord. Chem. Rev.* **2000**, *198*, 205
- <sup>14</sup> Goldberg, I. *Chem. Eur. J.* **2000**, *6*, 3863
- <sup>15</sup> Dastidar, P.; Stein, Z.; Goldberg, I.; Strouse, C. E. *Supramol. Chem.* **1996**, *7*, 257
- <sup>16</sup> Kumar, R. K.; Balasubramanian, S.; Goldberg, I. *Chem. Commun.* **1998**, 1435
- <sup>17</sup> Dahal, S.; Goldberg, I. *J. Phys. Org. Chem.* **2000**, *13*, 382
- <sup>18</sup> Aakerōy, C. B.; Beatty, A. M.; Leinen, D. S. *Angew. Chem. Int. Ed.* **1999**, *38*, 1815
- <sup>19</sup> Holman, K. T.; Pivovar, A. M.; Swift, J. A.; Ward, M. D. *Acc. Chem. Res.* **2001**, *34*, 107
- <sup>20</sup> Li, H.; Eddaoudi, M.; O’Keeffe, M.; Yaghi, O. M. *Nature* **1999**, *402*, 276
- <sup>21</sup> Soegiarto, A. C.; Yan, W.; Kent, A. D.; Ward, M. D. *J. Mater. Chem.* **2011**, *21*, 2204
- <sup>22</sup> Ramamurthy, V.; Eaton, D. F. *Chem. Mater.* **1994**, *6*, 1128
- <sup>23</sup> Toda, F.; Hyoda, S.; Okada, K.; Hirotsu, K. *J. Chem. Soc., Chem. Commun.* **1995**, 1531
- <sup>24</sup> Endo, K.; Koike, T.; Sawaki, T.; Hayashida, O.; Masuda, H.; Aoyama, Y. *J. Am. Chem. Soc.* **1997**, *119*, 4117
- <sup>25</sup> Miao, X.; Xu, L.; Li, Y.; Li, Z.; Zhou, J.; Deng, W. *Chem. Commun.* **2010**, *46*, 8830
- <sup>26</sup> Beatty, A. M. *Chem. Rev.* **2003**, *246*, 131
- <sup>27</sup> Griessl, S.; Lackinger, M.; Edelwirth, M.; Hietschold, M.; Heckl, W. M. *Single Mol.* **2002**, *3*, 25
- <sup>28</sup> Kuzmenko, I.; Buller, R.; Bouwman, W. G.; Kjaer, K.; Als-Nielsen, J.; Lahav, M.; Leiserowitz, L. *Science* **1996**, *274*, 2046
- <sup>29</sup> Alonso, C.; Eliash, R.; Jensen, T. R.; Kjaer, K.; Lahav, M.; Leiserowitz, L. *J. Am. Chem. Soc.* **2001**, *123*, 10105
- <sup>30</sup> Russell, V. A.; Ward, M. D. *J. Mater. Chem.* **1997**, *7*, 1123
- <sup>31</sup> Russell, V. A.; Evans, C. C.; Li, W.; Ward, M. D. *Science* **1997**, *276*, 575
- <sup>32</sup> Frostman, L. M.; Ward, M. D. *Langmuir* **1997**, *13*, 330
- <sup>33</sup> Plaut, D. J.; Martin, S. M.; Kjaer, K.; Weygand, M. J.; Lahav, M.; Leiserowitz, L.; Weissbuch, I.; Ward, M. D. *J. Am. Chem. Soc.* **2003**, *125*, 15922
- <sup>34</sup> (a) Berggren, K. K.; Bard, A.; Wilbur, J. L.; Gillaspay, J. D.; Helg, A. G.; McClelland, J. J.; Rolston, S. L.; Philips, W. D.; Prentiss, M.; Whitesides, G. M. *Science* **1995**, *269*, 1255. (b) Kim, E.; Whitesides, G. M.; Lee, L. K.; Smith, S. P.; Prentiss, M. *Adv. Mater.* **1996**, *8*, 139. (c) Hodneland, C. D.; Mrksich, M. *J. Am. Chem. Soc.* **2000**, *122*, 4235. (d) Aswal, D. K.; Lenfant, S.; Guerin, D.; Yakhmi, J. V.; Vuillaume, D. *Anal. Chim. Acta* **2006**, *568*, 84. (e) Phares, N.; White, R. J.; Plaxco, K. W. *Anal. Chem.* **2009**, *81*, 1095
- <sup>35</sup> Plaut, D. J.; Martin, S. M.; Kjaer, K.; Weygand, M. J.; Lahav, M.; Leiserowitz, L.; Weissbuch, I.; Ward, M. D. *J. Am. Chem. Soc.* **2003**, *125*, 15922
- <sup>36</sup> Love, J. C.; Estroff, L. A.; Krebel, J. K.; Nuzzo, R. G.; Whitesides, G. M. *Chem. Rev.* **2005**, *105*, 1103
- <sup>37</sup> Miao, X.; Xu, L.; Li, Y.; Li, Z.; Zhou, J.; Deng, W. *Chem. Commun.* **2010**, *46*, 8830
- <sup>38</sup> Furukawa, S.; Tahara, K.; De Schryver, F. C.; Van der Auweraer, M.; Tobe, Y.; De Feyter, S. *Angew. Chem. Int. Ed.* **2007**, *46*, 2831

- 
- <sup>39</sup> Theobald, J. A.; Oxtoby, N. S.; Phillips, M. A.; Champness, N. R.; Benton, P. H. *Nature* **2003**, *424*, 1029
- <sup>40</sup> Stepanow, S.; Lingenfelder, M.; Dmitriev, A.; Spillmann, H; Delvigne, E.; Lin, N.; Deng, X.; Cai, C.; Barth, J. V. Kern, K. *Nature Mater.* **2004**, *3*, 229
- <sup>41</sup> Kudernac, .; Lei, S.; Elemans, J. A. A. W.; De Feyter, S. *Chem. Soc. Rev.* **2009**, *38*, 402
- <sup>42</sup> In Situ Real-Time Characterization of Thin Films, ed. Auciello, O.; Krauss, A. R. 2001, New York: John Wiley & Sons, Inc.
- <sup>43</sup> Interfacial Electrochemistry: theory, experiment, and applications, ed. Wieckowski, A. 1999, New York: Mareel Dekker, Inc.
- <sup>44</sup> (a) Okahata, Y.; Shimizu, O. *Langmuir* **1987**, *3*, 1171. (b) Okahata, Y.; Matsuura, K.; Ito, K.; Ebara, Y. *Langmuir* **1996**, *12*, 1023.
- <sup>45</sup> Schierbaum, K. D.; Weiss, T.; Thoden von Velzen, E. U.; Engbersen, J. F. J.; Reinhoudt, D. N.; Göpel, W. *Science* **1994**, *265*, 1413.
- <sup>46</sup> (a) Ebara, Y.; Okahata, Y. *J. Am. Chem. Soc.* **1994**, *116*, 11209. (b) Ebara, Y.; Ebato, H.; Ariga, K.; Okahata, Y. *Langmuir* **1994**, *10*, 2267 (c) Ariga, K.; Okahata, Y. *Langmuir* **1994**, *10*, 2272, 3255.
- <sup>47</sup> (a) Ebersole, R. C.; Ward, M. D. *J. Am. Chem. Soc.* **1988**, *110*, 8623. (b) Ebersole, R. C.; Miller, J. A.; Moran, J. R.; Ward, M. D. *J. Am. Chem. Soc.* **1990**, *112*, 3239.
- <sup>48</sup> Sauerbrey, G. *Z Phys.* **1959**, *155*, 206
- <sup>49</sup> Reed, C. E.; Kanazawa, K. K.; Kaufman, J. H. *J. Appl. Phys.* **1990**, *68*, 1993
- <sup>50</sup> Kanazawa, K. K.; Gordon, J. G. *Anal. Chim. Acta.* **1985**, *175*, 99
- <sup>51</sup> Hager, H. *Chem. Eng. Commun.* **1986**, *43*, 25
- <sup>52</sup> Benes, E. *J. Appl. Phys. Chem.* **1984**, *56*, 608
- <sup>53</sup> Application note 31014 Thermo Scientific

# Chapter 3

## Host-Guest Assemblies for Functional Surfaces at the Air-Aqueous Interface

### 3.1. Introduction

The structure of guanidinium sulfonate based Langmuir monolayers formed from alkane sulfonate (anionic) amphiphiles and guanidinium cations have been well studied at the air-aqueous interface, however, none of the prior studies of GS host-guest monolayers have addressed the structure and properties of the films after transfer to a solid substrate, a necessary step to allow their use in a variety of application. The objectives of the work were (1) to investigate the structure of the deposited host-guest assemblies consisting of guanidinium, octadecylsulfonate and various alkane tethered guest molecules; (2) to evaluate the stability of the host-guest assemblies under exposure to non-polar organic solvent environments; (3) to study the feasibility of guest insertion and exchange from GS-based LB films in order to generate functional surface and to regenerate the functionality of a surface.

Molecules in crystalline solids are arranged in a regular structure and are close packed with minimal voids. In order to achieve this close-packing, some molecules form

interpenetrated structures or structures in which different molecules, or guest molecules, fill the voids. These are known as host-guest inclusion compounds. Host-guest compounds are broadly categorized into cavitands, molecular host compounds with intra-molecular cavities, and clathrate compounds with extra-molecular cavities that result from the aggregation of two or more molecules. In both categories host and guest molecules are connected via non-covalent interactions. Inclusion compounds are usually created by crystallization from various solvents. In some instances, the solvent used in crystallization is also entrapped into the crystal lattice of a substance, and the presence of solvent molecules in the crystal lattice confers unique physical properties to the solvate form.<sup>1</sup> For example, solubility and dissolution rates of a solvate are different than those of the corresponding anhydrate and can result in differences in properties. Hence, the study of crystallization in various conditions and the resultant solid phase has been critical for understanding molecular arrangements in crystals.

Since the initial discovery and structural determination of the earliest inclusion compounds, a great deal of effort has been directed toward the design of open host frameworks capable of including molecular guests. In particular, interest in host compounds with open molecular frameworks and their associated guests have been driven by developments in the synthesis and application of inorganic zeolites capable of accommodating organic compounds with suitable size and functionality. The shape and size of voids supplied by inorganic porous materials are, however, determined by rigid frameworks that are not readily amenable to the precise chemical modification required for many applications. Hence interest in organic molecular analogs of inorganic porous frameworks has emerged because the structure of organic host frameworks and their properties can be altered at the molecular level via synthetic organic chemistry. This modular strategy is based on molecular building blocks that assemble into supramolecular motifs via directional non-covalent bonding.

Large porous or channel structures can be generated under the presence of large counter-ions. One such example involves the cryptand- or crown-encapsulated potassium salts of octahedral  $[\text{Ni}(\text{Hbim})_3]^-$  depicted in Figure 2.1. The pseudo-hexagonal networks result in large amount of space, created via self-complementary of the HBim hydrogen

bonds.<sup>2</sup> Another 2-dimensional host framework is the host system of porphyrins containing peripheral hydrogen bonding substituent (Figure 2.2). Zn(II) porphyrin complexes have been synthesized by Goldberg<sup>3</sup> that include carboxylic acid, carboxamide, and diaminotriazine-substituted porphyrins.<sup>4,5,6,7</sup>

Host-frameworks that form a consistent porous structure allow crystalline structure to be separate from the function that guests included may introduce, and thus such host-guest compounds can be inherently versatile.<sup>8</sup> The diversity of host-guest compounds for materials applications has been established via the demonstration of porosity,<sup>9</sup> magnetic behavior,<sup>10</sup> nonlinear optical effects,<sup>11</sup> chemical storage,<sup>12</sup> catalysis,<sup>13</sup> etc. However, the open host-frameworks confront structural disruption as weak long-range interactions between building components can preclude the molecular assemblies from maintaining their solid form.<sup>14,15</sup> In many cases, guest-free porous molecular assemblies consist only of host-host frameworks, i.e., the structure is closely packed and does not provide enough space for guest inclusion. In order to prevent the collapse of the porous structure due to energetic considerations, the guest molecules are co-crystallized with the host structure.<sup>16</sup> In addition, it is often not straightforward to chemically alter the components of the molecular assembly as minor changes can cause disruption of the fundamental structure necessary for guest inclusion. Consequently, the creation of open host-framework for specific application via the systematic modification of molecular components is considerably limited.

The design of robust molecular hosts facilitates the creation of guest inclusion frameworks, and result in stable assemblies of molecules. One suggestion for the control of crystalline structure is to limit the assembly process to two dimensions by trapping molecules at an air-solution interface. The host framework can then be constructed via strong directional interactions based on a robust hydrogen-bonded structural motif: various geometrical shapes and dimensionality allow the construction of diverse hydrogen-bonded frameworks. Such strongly hydrogen-bond interconnected frameworks can have high modifiability and flexibility.<sup>17</sup> Thin interdigitated films proposed by Kuzmenko et al. have been extended to other two components system of water-insoluble amphiphiles and water-soluble counterparts. Based on these observations, further studies have shown that amphiphiles capable of binding water-soluble guest molecules at the air-aqueous interface

are able to form host-guest compounds. An amphiphile containing cholesterol hydrophobe and water-soluble chiral amino acid affords a crystalline monolayer structure, which exhibits host-like properties: cholesterol hydrophobes create a low-density lattice via selective incorporation of amino acid from the aqueous subphase.<sup>18</sup> Another interdigitated molecular system has been obtained upon deposition of an organosulfonate amphiphile over an aqueous subphase containing guanidinium, studied by Ward and co-worker.<sup>19,20</sup> This acid-base system allows the intercalation of guanidinium  $[\text{C}(\text{NH}_2)_3^+]$  cations between octadecanesulfonate  $[(\text{C}_{18}\text{H}_{37}\text{SO}_3)^-]$  anions and results in the formation of a 2-dimensional hydrogen-bonded network.<sup>21</sup> This interdigitated molecular system suggests that monomolecular films with spacer molecules at the air-aqueous interface can have inherent inclusion cavities between pre-expanded hydrophobe arrays, affording hosts for non-amphiphilic guest molecules and generating two-dimensional inclusion compounds at the air-aqueous interface. Plaut et al suggest that guest intercalation in this fashion can permit the introduction of functionality that otherwise may not be achievable at the air-aqueous interface.<sup>22,23</sup>

The structure of guanidinium sulfonate based Langmuir monolayers formed from alkylbiphenyl sulfonate or alkane sulfonate amphiphiles and guanidinium counter-ions have been well studied at the air-aqueous interface, however, none of the prior studies of GS host-guest monolayers have addressed the structure and properties of the films after transfer to a solid substrate, a necessary step to allow their use in a variety of applications. Herein, we investigate the structure of the deposited host-guest assemblies consisting of guanidinium (**G**), octadecylsulfonate (C18S) and various alkane tethered guest molecules using grazing angle incidence X-ray diffraction (GIXD) and specular X-ray reflectivity (XRR) techniques. GIXD and XRR measurements can provide the unit cell parameters, unit cell area, film thickness, and averaged electron density of the structures. In particular we evaluate the stability of the host-guest assemblies under exposure to non-polar organic solvent environments using X-ray reflectivity measurements. The stability studies will provide us with stability windows for host-LB films in which we can tune the solvent conditions for optimal guest solubility. Finally, we study the feasibility of guest insertion and exchange from GS-based LB films in order to generate the functional surfaces and regenerate the

functionality of surface.

## 3.2. Experimental Section

### 3.2.1. Materials

Sodium 1-octadecanesulfonate (C18S, >99%), guanidine carbonate (G, 99%), hexadecane (C16, >99%), 1-bromooctadecane (C18Br, 97%), 1-octadecanol (C18OH, 99%), 2-naphthyl stearate (NaphC18), cholesteryl stearate (CholC18), 1-phenyl-1-hexadecaneol (PhOC16), N-phenylhexadecylamine (PhNC16), 1-phenyltetradecane (PhC14), hexane(C6), cyclohexane(CH), and chloroform were purchased from Sigma-Aldrich and used without further purification. Deionized water (purified to 18.2 MΩcm with a Barnstead water purifier) was used as an aqueous subphase. A silicon wafer (p-type, boron doped, resistivity < 1 Ωcm, single polished) as a substrate for LB film deposition was purchased from Wafer World (West Palm Beach, FL).

### 3.2.2. Surface Pressure-Area (II-A) Isotherm and Langmuir-Blodgett Films

II-A isotherms were recorded on Nima Langmuir trough (Model No. 312d) with a filter paper Wilhelmy balance at a compression rate of 5cm<sup>2</sup>min<sup>-1</sup>. Targeted surface pressure for deposition of LB film on pre-cut silicon substrate was determined from collected isotherms and was maintained constant by controlling the barrier. All depositions were carried out at a speed of 2mmmin<sup>-1</sup>. Prior to the deposition, silicon substrates were treated in concentrated H<sub>2</sub>SO<sub>4</sub>/H<sub>2</sub>O<sub>2</sub> (3:1 by volume) for 15 min at 100°C (**caution:** Piranha solution is highly explosive, and care should be taken while using this mixture), then washed with deionized water thoroughly. For the formation of 1:1 hydrogen-bonded network between guanidinium (G) ions and sulfonate moieties (S), a subphase concentration of 2.5×10<sup>-3</sup>M with guanidinium ions was prepared. All GS monolayers (guest-free and host-guest) were prepared by spreading the chloroform solutions containing 5% methanol (v/v), C18S (0.37mg/ml, 1.0×10<sup>-3</sup>M), and an equimolar amount of C16, C18Br, C18OH, and NaphC18 (if any). Sterically hindered host-guest monolayers were also prepared by the chloroform

solution of PhOC16 and PhNC16 ( $0.48 \times 10^{-3} \text{M} - 1.74 \times 10^{-3} \text{M}$ ) as a host, and an equimolar amount of C16 and PhC14. About 15min was allowed for the solvents to evaporate entirely before compression was initiated.

### **3.2.3. Grazing-angle incidence X-ray diffraction and X-ray Reflectivity**

GIXD and XRR data were measured using synchrotron radiation at the bending magnet X-ray diffraction beamline BL2-1 of the Stanford Synchrotron Research Lightsource (Menlo Park, CA). By use of a Si (111) double crystal monochromator, a wavelength,  $\lambda$ , of 0.154nm was selected with  $\Delta E/E = 5 \times 10^{-4}$ . X-rays were focused onto the sample by Rh-coated mirror and the sample was mounted on a Huber 2-circle goniometer and a high resolution crystal-analyzer detector was used. The reflectivity data were analyzed using a non-linear least-square fitting program, StochFit, with a multi-box model and the minimum number of constraints and the thickness of the host-monolayers was obtained in the direction normal to the surface.

### 3.3. Results and Discussion

#### 3.3.1. $\Pi$ -A isotherms for guest-free monolayers

Surface pressure-area ( $\Pi$ -A) isotherm of sodium octadecane sulfonate (NaC18S) on a pure water subphase revealed the formation of close-packed monolayer phase with a molecular area of  $A_{\text{mol}} = 24 \text{ \AA}^2/\text{sulfonate}$  (from extrapolating the linear part of the  $\Pi$ -A isotherm in Figure 3.1a), albeit showing the influence of the sulfonate head group when compared to the cross sectional area of close-packed alkane chains ( $21 \text{ \AA}^2$ ).<sup>24,25,26</sup> On the other hand, the  $\Pi$ -A isotherm in Figure 3.1b acquired on an aqueous subphase containing 0.025 M guanidinium carbonate ( $\text{G}_2\text{CO}_3$ ) gives a molecular area of  $A_{\text{mol}} = 44 \text{ \AA}^2/\text{sulfonate}$ . This extended area indicates the formation of **GS** hydrogen-bonded network at the air-aqueous interface, sufficient for intercalation of structurally homologous functional guest molecules.<sup>27,28,29,30</sup> The alkanes of C18S cannot achieve a close-packed arrangement of alkane chains because of the intervening **G** ions. These observations are consistent with the results in crystalline **GS** compounds observed by Plaut et al.<sup>22,23</sup>

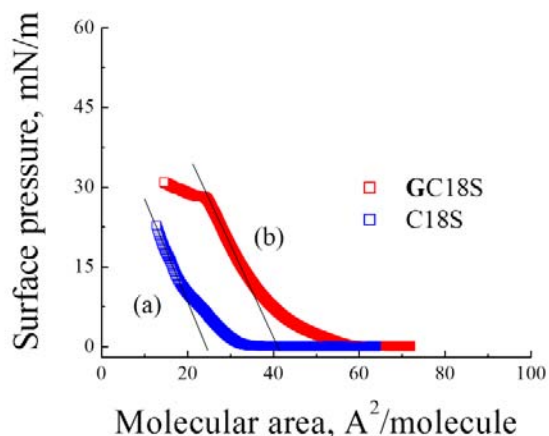


**Figure 3. 1.**  $\Pi$ -A isotherms of NaC18S (a) on a pure water subphase and (b) on an aqueous subphase containing 0.025M  $\text{G}_2\text{CO}_3$ . The molecular area is  $A_{\text{mol}} = 27 \text{ \AA}^2/\text{sulfonate}$  for NaC18S over pure water and  $A_{\text{mol}} = 44 \text{ \AA}^2/\text{sulfonate}$  for NaC18S over 0.025 M  $\text{G}_2\text{CO}_3$  aqueous subphase.

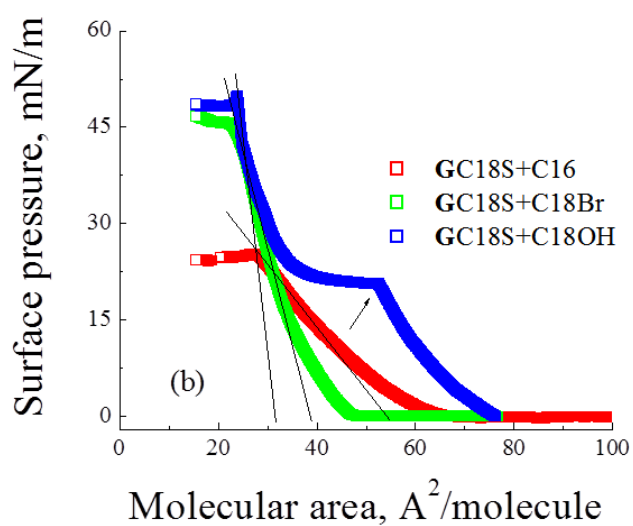
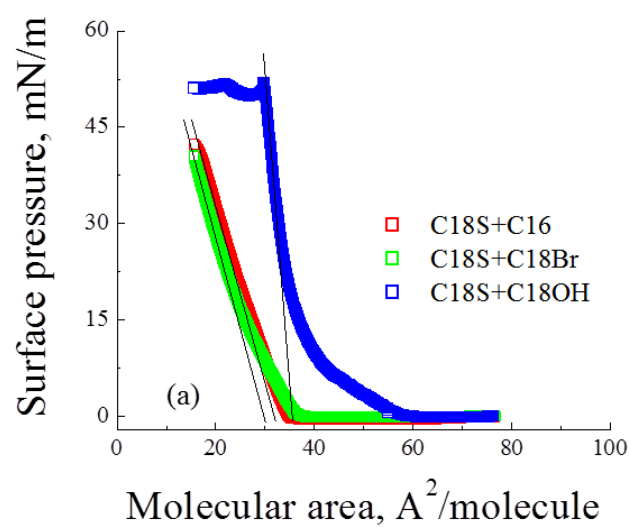


**Figure 3. 2.**  $\Pi$ -A isotherms for 1:1 mixture of (a) C18S on pure water, and (b) C18S monolayers on an aqueous subphase containing 0.025M  $\text{G}_2\text{CO}_3$  with guest molecules, such as C16, C18Br, and C18OH, respectively.

### 3.3.2. $\Pi$ -A isotherms for host-guest monolayers

In order to probe the contribution of host-guest interactions on the stability of host-guest mixed monolayers at an air-aqueous interface, the  $\Pi$ -A behaviors of the Langmuir monolayers of 1:1 mixtures of NaC18S and various guest molecules spread over both a pure water and a 0.025 M  $G_2CO_3$  aqueous subphase were studied. First, the isotherms of the C18S:C16, C18S:C18Br, and C18S:C18OH mixed monolayer in the absence of **G** ion show similar patterns with a molecular area of  $A_{mol} = 30\sim 35 \text{ \AA}^2/\text{molecule}$ , larger than that of guest-free C18S monolayer, which indicates an increase of packing density and thus the formation of robust 1:1 mixed monolayer. In particular, a steep rise of surface pressure upon compression reflects an increase in the stiffness of monolayer due to the development of a close-packed arrangement of alkane chains (Figure 3.2a).<sup>31,32,33</sup> For example, it has been reported that 1-octadecanol behaves like host amphiphiles, thereby forming a monolayer on its own.<sup>34</sup> Thus the steep slope on the isotherm reflects the formation of a crystalline structure on an air-aqueous interface.

The  $\Pi$ -A isotherms of the same guest molecules on an aqueous subphase of  $G_2CO_3$ , were different than the isotherms on a pure water. As shown in Figure 3.2b, the isotherms rose less steeply. A gradual rise in surface pressure in the beginning indicates the formation of a loosely-packed monolayer phase due to the presence of **GS** hydrogen-bonded network. The isotherm of (**G**)C18S:C16 mixed monolayer reveals a collapse pressure of  $\pi = 25 \text{ mN/m}$ , lower compared to the collapse pressure (45 mN/m) for (**G**)C18S:C18Br and (**G**)C18S:C18OH mixed monolayers, indicating that the (**G**)C18S:C16 monolayer is less stable than the others. We believe that hexadecane, hydrophobic molecule, tends to aggregate in an air-aqueous interface. Thus it is reasonable to suggest that hexadecane interrupts the formation of close-packed arrangement and is expelled from the (**G**)C18S monolayer upon further compression. It is interesting to note that the molecular area of (**G**)C18S:guest mixed monolayer varies considerably with the guests. This suggests that **GS** hydrogen-bonded motif is altered upon compression, i.e., functional end groups on the alkane guests produce different **GS** hydrogen-bonded motif by interrupting the **GS** hydrogen bonding.<sup>35,36,37,38</sup>

### 3.3.3. Stability of (G)C18S-based Langmuir-Blodgett films

(G)C18S-based monolayers containing a variety of guests were transferred to clean silicon substrates at a surface pressure of  $\pi = 20$  mN/m using the Langmuir-Blodgett (LB) technique. This pressure was selected as it is below the collapse pressure of all of the Langmuir monolayers (except the guest-free C18S monolayer on pure water), as shown by the  $\Pi$ -A isotherm depicted in Figure 3.3. The resulting LB monolayers were immersed in non-polar solvents either hexane, a straight-chain alkane, or cyclohexane, a cyclic alkane, and were examined via grazing-angle incidence X-ray diffraction (GIXD), specular X-ray reflectivity (XRR) and contact angle measurements. Only non-polar solvents were used, as the LB films proved to be completely unstable in aqueous or other polar solvents.

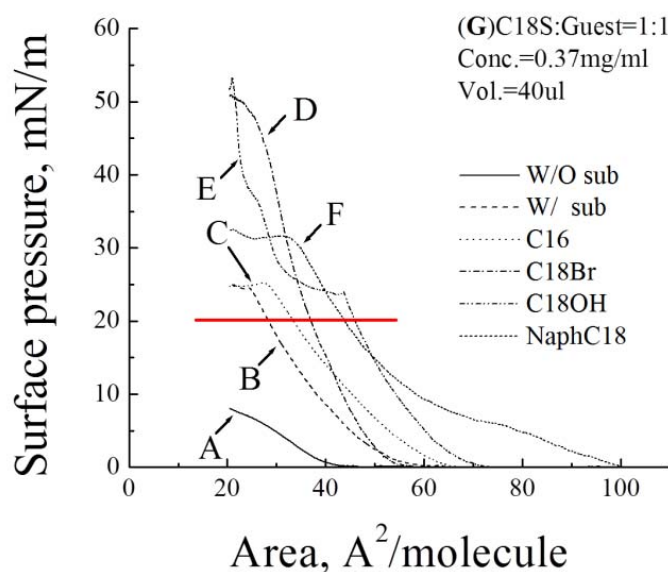


**Figure 3. 3.**  $\Pi$ -A isotherms of (a) C18S on pure water and (G)C18S with (b) guest-free, (c) C16, (d) C18Br, (e) C18OH, and (f) NaphC18 on 0.025M  $G_2CO_3$  aqueous subphase. The host-guest mixed monolayers at air-aqueous interface are transferred to a clean Si substrate at the surface pressure of  $\pi = 20$  mN/m.

XRR data were analyzed using StochFit software based on a Levenberg-Marquardt non-linear least-squares fit.<sup>39</sup> Based on the molecular structure and its physical parameters,

the structure is divided into a fixed number of the XRR model consists of a set of layers characterized by a thickness, electron density, and roughness, respectively.<sup>40</sup> The electron density of each layer is normalized with respect to the electron density of Si. All fits for (G)C18S-based monolayers were obtained using a two-box model (SiO<sub>2</sub> layer and amphiphilic monolayer). Generally two boxes provided an adequate description of the host-guest assemblies while minimizing the number of fitted parameters, as the simplest structural interpretation of an amphiphilic monolayer is a division into a hydrophobic and hydrophilic slab.<sup>41</sup>

### 3.3.3a. Guest-free (G)C18S monolayer

Figure 3.4 shows the two-box model-fitting of the normalized electron density for a guest-free (G)C18S LB monolayer soaked in hexane (C6) for 0, 0.5, and 2 hrs. Prior to immersion in hexane, the XRR fitting results in a film thickness of 16.2 Å, less than the length (ca. 25 Å) expected for octadecane based on the maximum extension of an aliphatic chain in the all-*trans* configuration.<sup>42</sup> Assuming straight chains, this would require that the alkane chains be tilted 49.6° from the normal to the surface. A projected area of 32.4 Å<sup>2</sup> of an alkane chain estimated from the degree of tilt and the cross-sectional area of an alkane chain (~21 Å<sup>2</sup>) corresponds closely to the measured molecular area of  $A_{\text{mol}} = 30 \text{ Å}^2/\text{molecule}$  at the deposition surface pressure of  $\pi = 20 \text{ mN/m}$ . In addition, the normalized electron density is 0.395 ( $=\rho/\rho_{\text{Si}}$ ), which is larger than the density of liquid alkanes ( $\rho/\rho_{\text{Si}} = 0.32, 0.75 \text{ g/cm}^3$ ) but similar to the density of crystalline alkanes ( $\rho/\rho_{\text{Si}} = 0.399, 0.93 \text{ g/cm}^3$ ).<sup>43</sup> This suggests that the monolayer maintains a densely-packed structure of alkane chains. As immersion time in hexane increases, a significant decrease in the film thickness and the electron density of the monolayer was observed. This suggests that the guest-free (G)C18S LB monolayer is not entirely stable in hexane and is losing material, resulting in alkane chains that are more tilted toward less densely packed.<sup>44</sup>

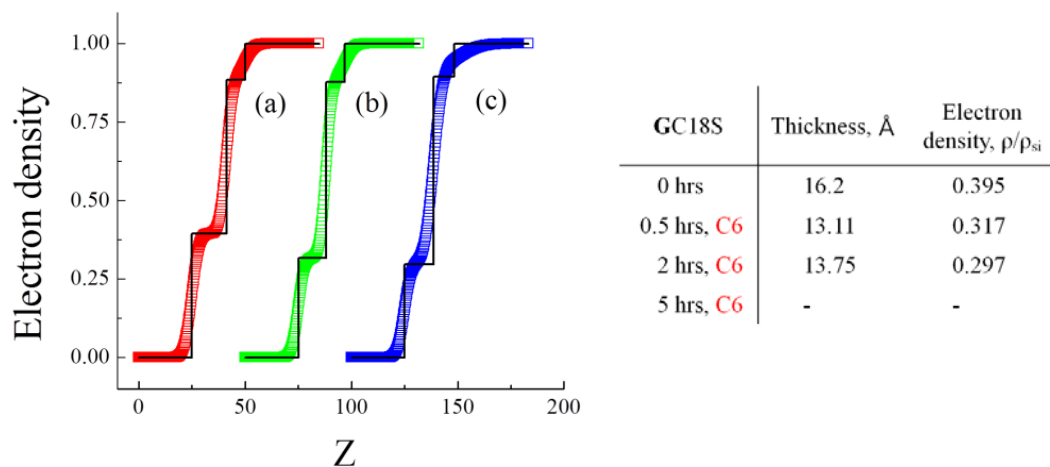


**Figure 3. 4.** The electron density profile and summarized results corresponding to the data fits for (G)C18S guest-free monolayer. (G)C18S guest-free monolayer was compressed to 20 mN/m and then transferred to Si substrate. After LB deposition, samples were placed into hexane for different amount of time. Upon removal from hexane, X-ray reflectivity data was taken of the sample and fitted with two box models to determine the changes in the molecular structure of the film.

GIXD measurements on the (G)C18S LB film resulted in no discernible scattering peaks, indicating that there was no long-range lateral ordering of (G)C18S monolayer at the interface. This suggests the formation of an amorphous structure of the monolayer.<sup>45,46,47</sup> Guest-free (G)C18S monolayers at the air-aqueous interface have been shown to be crystalline using liquid surface GIXD measurements, however, it is likely that this weak structure is disrupted during the LB deposition process. The absence of in-plane structure is attributed to an imbalance between competing interactions in the film: hydrogen bonding in the GS network, electrostatic interactions at the interfaces between SiO<sub>2</sub> and neighboring sulfonate moieties, and van der Waals interactions among alkane chains.<sup>48</sup> In this regard, Garnaes et al reported that the transfer process was accompanied by an increase of the unit cell area (about 17 percent) and by an increase of the average domain diameter of nanometer-scale domains (about three times) due to the cross-sectional mismatch between head and tail groups of octadecylthio-1,4-benzoquinone.<sup>49</sup>

### 3.3.3b. (G)C18S:C18Br monolayer.

As shown in Figure 3.5, the electron density profile for (G)C18S:C18Br mixed monolayer immersed in hexane (C6) demonstrates that there are no significant changes in the electron density despite a decrease in the film thickness, indicating that the structure of the monolayer immersed in hexane (C6) is maintained. The increased stability compare to the guest-free monolayer is attributed to the more closely packed and less-tilted host-guest structure, thereby increasing the effective contact area between alkane chains. In contrast, the profile for (G)C18S:C18Br mixed monolayer immersed in cyclohexane (CH) shows that the electron density significantly decreases from 0.37 to 0.285, indicating a structural change within the monolayer caused by discharge of guest molecules (C18Br). This suggests that cyclohexane act against a stabilization of the structure of the monolayer, unlike hexane. In this context, Jiang et al reported that with the increase of the chain length or ring size of alkane guests, the van der Waals interactions increase and thus the steric energy differences between  $\beta$ -cyclodextrin and alkane guests decrease. According to them, cyclohexane is more suitable for an inclusion process than hexane.<sup>50</sup>

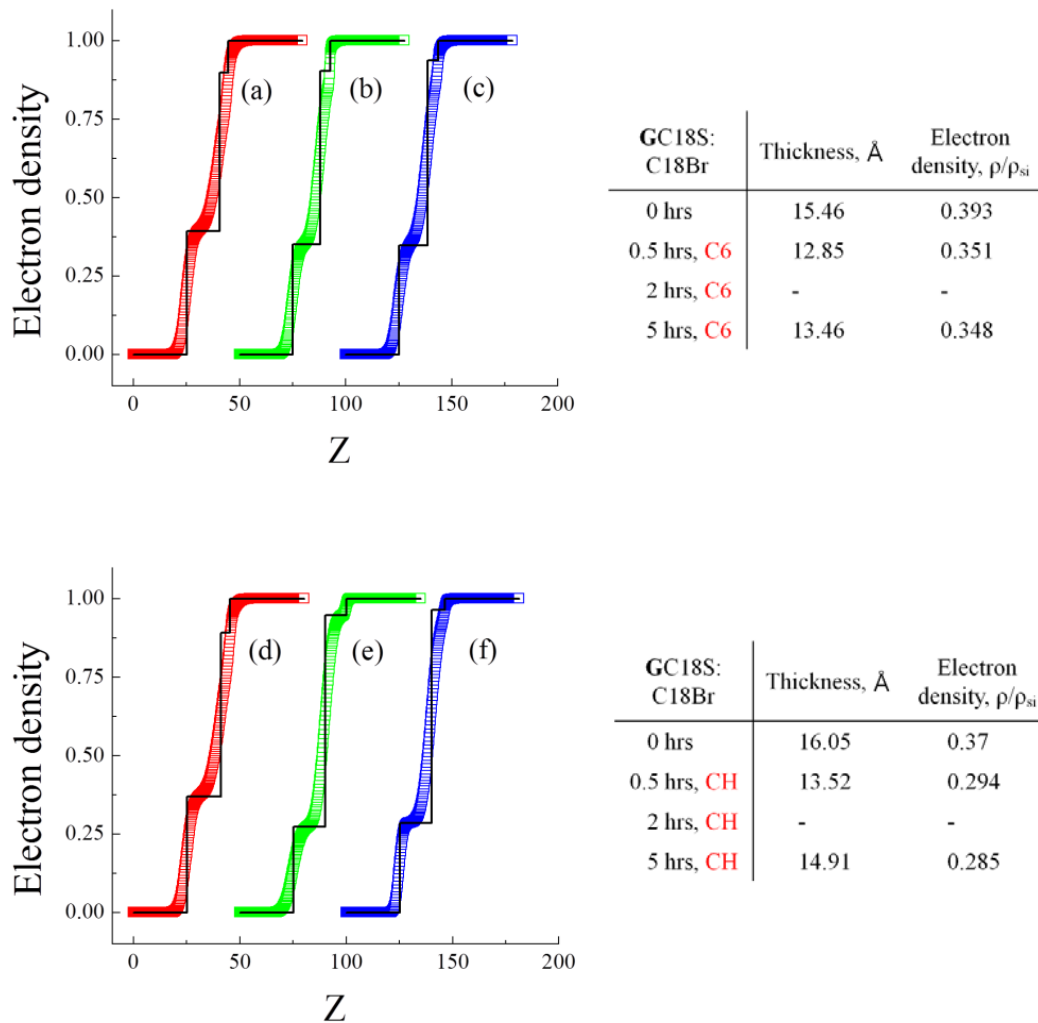


**Figure 3. 5.** Electron density profiles and summarized results corresponding to the data fits for (G)C18S:C18Br monolayer. (G)C18S:C18Br monolayer was compressed to 20 mN/m and then transferred to Si substrate. After LB deposition on Si, samples were placed into pure hexane and cyclohexane solutions for different amount of time. Upon removal from the solution, X-ray reflectivity was taken of the sample and fitted with two box models to determine the changes in the molecular structure of the film.

### 3.3.3c. (G)C18S:C18OH monolayer.

As shown in Figure 3.6, the electron density profile reveals that the initial thickness of (G)C18S:C18OH mixed monolayer is 24~27 Å before immersion in a solvent, corresponding

to the value of fully extended alkane chain length of octadecane. This suggests that the alkane chains are almost vertically oriented with respect to the interface. However, the vertical orientation of alkane chains cannot be achieved under the presence of **G** ions as the cross-sectional area of the alkane chain ( $21 \text{ \AA}^2$ ) is less than that of the cavity ( $44 \text{ \AA}^2$ ). In this context, Mayya et al reported that electrically neutral octadecanol acts as a spacer molecule in the octadecylamine Langmuir film, thereby minimizing repulsive electrostatic interactions between the protonated amine groups. As such, we believe that the presence of octadecanol in the host film precludes **G** ions from intervening between organosulfonate. It is reasonable to suggest that there is no **GS** hydrogen-bonded network in the (G)C18S:C18OH LB monolayer. After immersion of (G)C18S:C18OH LB films in hexane and cyclohexane, the electron density profiles show a substantial decrease in both thickness and electron density, indicating that the structure of the monolayer is disrupted by a dissolution of host-guest assemblies. When combined with the previous result, this suggests that hydroxy or bromine end group of guests can disrupt the formation of the **GS** hydrogen-bonded network and decrease the stability of the LB film. In other words, **GS** hydrogen-bonded network in the host-guest LB film also contributes to the stability of the host-guest LB films.

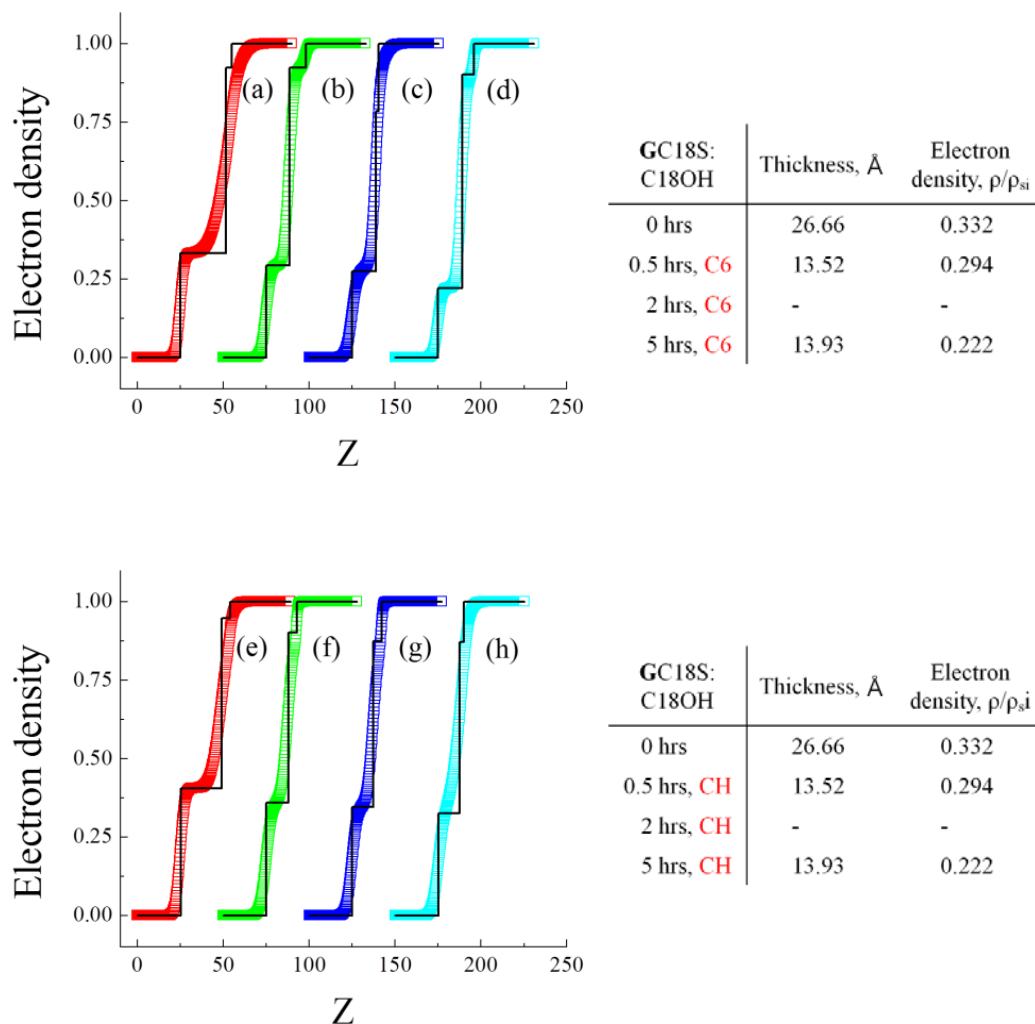


**Figure 3. 6.** Electron density profiles and summarized results corresponding to the data fits for (G)C18S:C18OH monolayer. (G)C18S:C18OH monolayer was compressed to 20 mN/m and then transferred to Si substrate. After LB deposition on Si, samples were placed into hexane and cyclohexane solutions for different amount of time. Upon removal from the solution, X-ray reflectivity was taken of the sample and fitted with two box models to determine the changes in the molecular structure of the film.

### 3.3.3d. (G)C18S:NaphC18 monolayer.

As shown in Figure 3.3, the isotherm of (G)C18S:NaphC18 mixed monolayer exhibits a liftoff pressure at  $A_{\text{lif-off}} > 100 \text{ \AA}^2/\text{sulfonate}$  followed by a steady increase in surface

pressure. Further compression results in a steep increase in the surface pressure that approaches a liquid-like expanded-phase with a molecular area at  $A_{\text{mol}} = 62 \text{ \AA}^2/\text{sulfonate}$  where the alkane chains are conformationally disordered. The monolayer collapsed at  $\pi = 30 \text{ mN/m}$ , but upon further compression the surface pressure increased steadily, suggesting that the plateau region is in the phase transition towards a condensed phase. A deposition surface pressure of  $\pi = 30 \text{ mN/m}$  corresponds to  $A_{\text{mol}} = 42 \text{ \AA}^2/\text{sulfonate}$  which suggests an intercalated host-guest monolayer containing C18Naph molecules. As shown in Figure 3.7, the electron density profile for a (G)C18S:NaphC18 LB film immersed in cyclohexane (C6) for 0.5 and 5 hrs reveals no significant change in either film thickness or electron density, indicating stable host-guest assembly.<sup>51,52</sup>

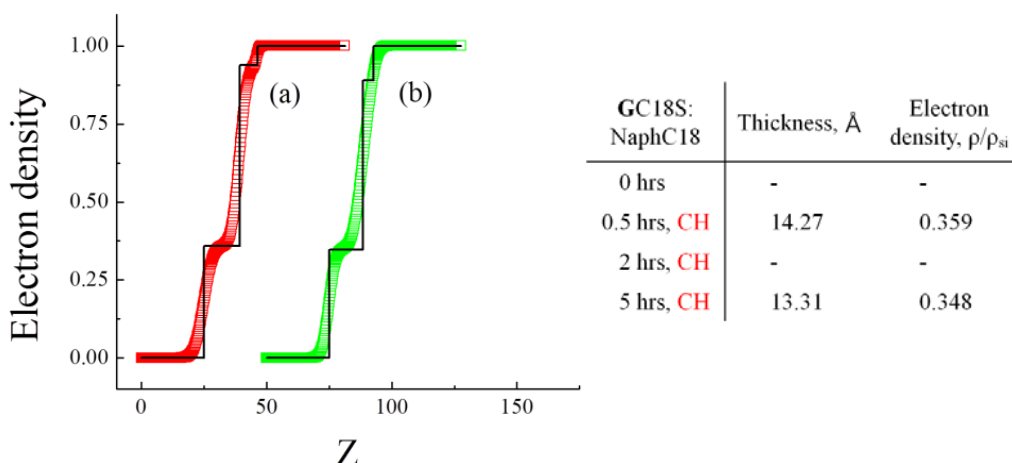


**Figure 3. 7.** Electron density profile and summarized result corresponding to the data fits for (G)C18S:NaphC18 monolayer. (G)C18S:NaphC18 monolayer were compressed to 20 mN/m and then transferred to Si substrate. After LB deposition on Si, (G)C18S:NaphC18 monolayers were placed into cyclohexane solutions for different amount of time respectively. Upon removal from the solution, X-ray reflectivity was taken of the sample to determine the changes in the molecular structure of the film.

Figure 3.8 summarizes the electron density profiles for the (G)C18S-based LB films studied. Based on the results of stability experiments conducted on as-deposited guest free and host-guest monolayers, we draw the following conclusions: (i) host monolayers based on the hydrogen-bonded GS network provide cavities capable of accommodating guest

molecules; (ii) stable host-guest assemblies cannot be achieved permanently via the Langmuir-Blodgett technique; (iii) the nature of functional end group on the alkane guest has an effect on the stability of the host-guest LB film by altering the GS hydrogen-bonded motif or blocking the formation of GS hydrogen-bonding; (iv) exposure to non-polar solvents can cause disruption of the hydrogen-bonded GS network even though host-guest assembly achieves densely-packed structure.

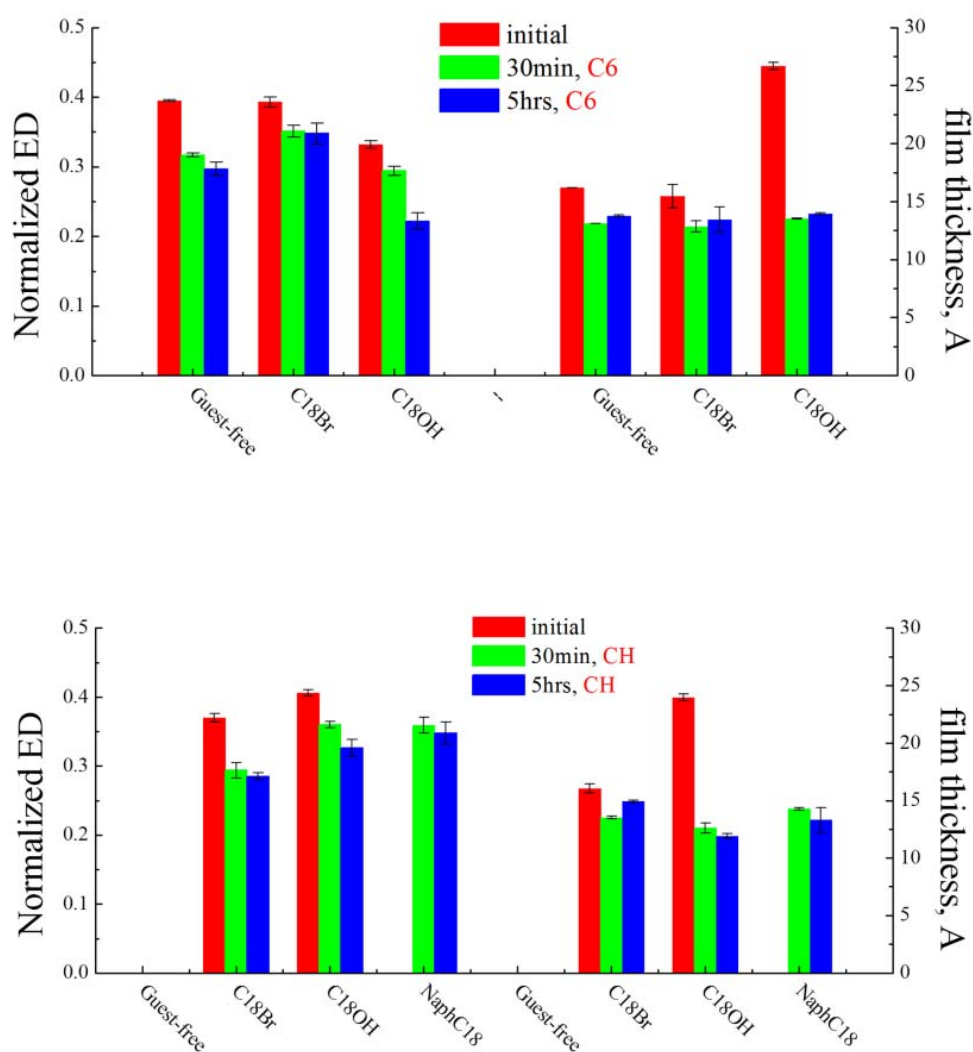


**Figure 3. 8.** Summarized electron density profiles for (G)C18S-based Langmuir-Blodgett films.

### 3.3.3e. Guest intercalation and exchange based on (G)C18S monolayer

(G)C18S LB monolayers were immersed in 5 mM solutions of naphthyl stearate and cholesteryl stearate respectively, in order to probe the intercalation of guest molecules into the cavities of a guest-free host monolayer. As shown in Figure 3.9, the electron density profiles show an increase in the film thickness and a decrease in the electron density of each film after immersion. As mentioned in section 3.3.3b, the driving force for host-guest complexation is dominated by non-covalent van der Waals interaction between the host and the guest. In addition, the molecular size and shape of the guest are crucial factors in the inclusion. Considering the size and shape of naphthyl stearate, naphthyl stearate is expected to be intercalated into the host cavities. This suggests that an optimal packing of the host-guest assembly can be achieved via intercalation of the guests. This can also be interpreted as collapse of the host monolayer and then deposition of a poorly packed guest layer at the surface. Unfortunately, there is no evidence to support these suggestions in this study.

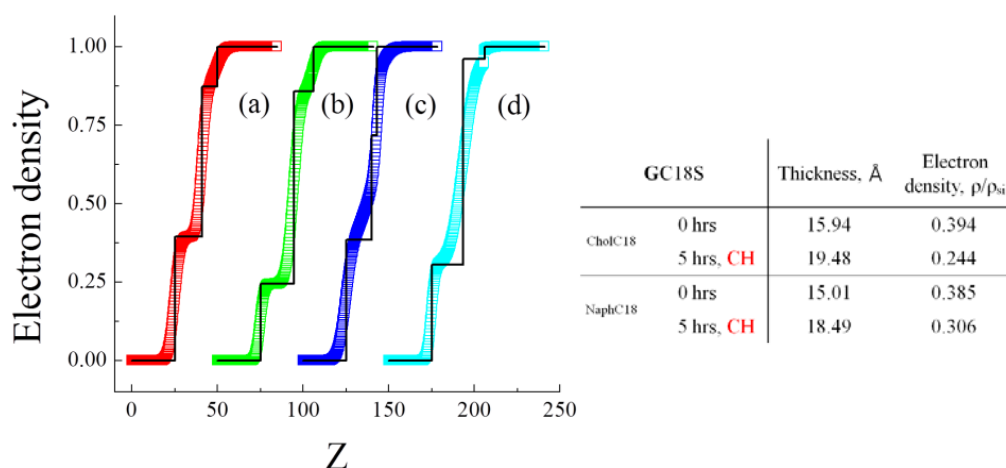


**Figure 3. 9.** The electron density profiles and summarized results corresponding to the data fits for (G)C18S guest-free monolayers. (G)C18S guest-free monolayer was compressed to 20 mN/m and then transferred onto Si substrate. After LB deposition, samples were placed into two different solutions of CholC18 and NaphC18 in cyclohexane for different amount of time. Upon removal from the solution, X-ray reflectivity was taken of the sample and fitted

with two box models to determine the changes in the molecular structure of the film.

The replacement of cholesteryl stearate within a (G)C18S LB film by immersion in a solution of naphthyl stearate was also examined. The electron density profile for (G)C18S:CholC18 monolayers immersed in NaphC18 solution in cyclohexane shows no significant change in either the film thickness or the electron density, indicating the integrity of the host-guest assembly in cyclohexane. However, there is also no evidence that cholesteryl stearate was replaced by naphthyl stearate.

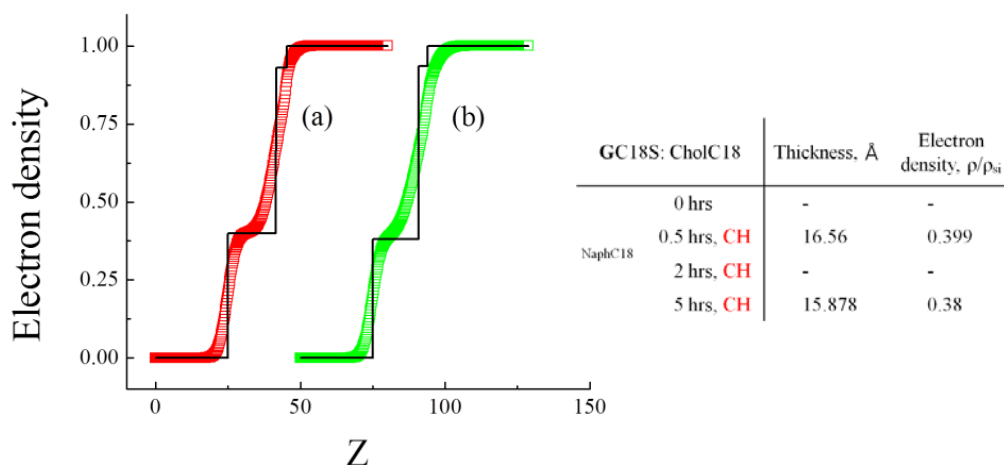


**Figure 3. 10.** The electron density profiles and summarized results corresponding to the data fits for (G)C18S-CholC18. (G)C18S:CholC18 monolayer were compressed to 20 mN/m and then transferred to Si substrate. After LB deposition on Si, (G)C18S:CholC18 monolayers were placed in the naphthyl stearate solution in cyclohexane for different amount of time respectively. Upon removal from the solution, X-ray reflectivity was taken of the sample to determine the changes in the molecular structure of the film.

### 3.4. Conclusion

Two-dimensional host-guest monolayers based on hydrogen-bonded network of guanidinium (G) cations, octadecylsulfonate (S) anions, and various guest molecules were generated at the air-aqueous interface and transferred to silicon substrates using the

Langmuir-Blodgett technique. The stability of host-guest assemblies with various guest molecules was studied by immersion in hexane or cyclohexane.

No GIXD Bragg peaks were observed for any of (G)18S-based monolayers, indicating that there was no long-range 2-D lateral ordering in the in-plane direction at the interface and thus (G)C18S-based monolayer is generally amorphous. Prior studies of guest-free (G)C18S monolayers at the air-aqueous interface have shown the formation of crystalline structure using liquid surface GIXD measurements, however, it is likely that this weak structure is disrupted during the LB deposition process

XRR analysis via box-model fitting revealed that permanent stability of the host-guest assembly cannot be achieved via Langmuir-Blodgett technique.  $\Pi$ -A isotherms and XRR data combined showed that a nature of functional end group on the alkane guests has a considerable implication for the formation of GS hydrogen-bonding. For example, hydroxy end group on the alkane guest acts as a spacer, thereby blocking the formation of GS hydrogen-bonding. The absence of in-plane GS hydrogen-bonding results in easy dissolution of the host-guest assembly in non-polar solvents. The study on guest insertion or exchange did not show an evidence to support the presence of intercalated guests in the LB film.

Despite the ease of the fabrication of host-guest assembly for a functional surface, this approach has a restricted extension in application due to the stability problem. This suggests an approach for the immobilization of host monolayer with cavity structure on a solid surface. The size and shape of host cavity can be controlled by introduction of bulky spacer molecule. This approach offers the potential of separating the functional of the monolayer from the inherent structure of the host.

### **3.5. Summary**

Host-guest assemblies composed of a two-dimensional GS host network with inherent cavities and alkane guests with various functional end groups were generated at the air-aqueous interface and deposited on to solid substrates to create functional surfaces. Alkane guests with the following functional groups were intercalated within pre-expanded cavities

between hydrophobes of **GS** host framework at air-aqueous interface: hexadecane, 1-bromooctadecane, 1-octadecanol, naphthyl stearate, and cholesteryl stearate. After deposition of the host-guest assembly onto a solid substrate, the integrity of the host-guest assembly and its ability to replace guest molecule were examined by immersion in the non-polar organic solvents, hexane and cyclohexane. The structural changes of the host-guest assemblies in organic solvents were characterized using grazing-angle incidence X-ray diffraction (GIXD) and X-ray reflectivity (XRR). No GIXD Bragg peaks were observed for any of the (**G**)18S monolayers with or without guest molecules, indicating the formation of amorphous structure. XRR analysis showed that a nature of functional end group on the alkane guests has a considerable implication for the formation of **GS** hydrogen-bonding. For example, hydroxy end group on the alkane guest acts as a spacer, thereby blocking the formation of **GS** hydrogen-bonding. The absence of in-plane **GS** hydrogen-bonding results in easy dissolution of the host-guest assembly in non-polar solvents. The study on guest insertion or exchange did not show an evidence to support the presence of intercalated guests in the LB film.

Despite the ease of the fabrication of host-guest assembly for a functional surface, this approach has a restricted extension in application due to the stability problem. This suggests an approach for the immobilization of host monolayer with cavity structure on a solid surface. The size and shape of host cavity can be controlled by introduction of bulky spacer molecule. This approach offers the potential of separating the functional of the monolayer from the inherent structure of the host.

### 3.6. References

- 
- <sup>1</sup> Kumar, T. L.; Guleria, P.; Vishweshwar, P.; Sivalakshmidēvi, A.; Babu, J. M.; Vyas, K.; Acharyulu, P. V. R.; Sekhar, N. M.; Kumar, B. S. *J. Incl. Phenom. Macrocycl. Chem.* **2010**, *66*, 261
  - <sup>2</sup> Tadokoro, M.; Nakasuji, K. *Coord. Chem. Rev.* **2000**, *198*, 205
  - <sup>3</sup> Goldberg, I. *Chem. Eur. J.* **2000**, *6*, 3863
  - <sup>4</sup> Dastidar, P.; Stein, Z.; Goldberg, I.; Strouse, C. E. *Supramol. Chem.* **1996**, *7*, 257
  - <sup>5</sup> Kumar, R. K.; Balasubramanian, S.; Goldberg, I. *Chem. Commun.* **1998**, 1435
  - <sup>6</sup> Dahal, S.; Goldberg, I. *J. Phys. Org. Chem.* **2000**, *13*, 382

- 
- <sup>7</sup> Aakerōy, C. B.; Beatty, A. M.; Leinen, D. S. *Angew. Chem. Int. Ed.* **1999**, *38*, 1815
- <sup>8</sup> Holman, K. T.; Pivovar, A. M.; Swift, J. A.; Ward, M. D. *Acc. Chem. Res.* **2001**, *34*, 107
- <sup>9</sup> Li, H.; Eddaoudi, M.; O'Keeffe, M.; Yaghi, O. M. *Nature* **1999**, *402*, 276
- <sup>10</sup> Soegiarto, A. C.; Yan, W.; Kent, A. D.; Ward, M. D. *J. Mater. Chem.* **2011**, *21*, 2204
- <sup>11</sup> Ramamurthy, V.; Eaton, D. F. *Chem. Mater.* **1994**, *6*, 1128
- <sup>12</sup> Toda, F.; Hyoda, S.; Okada, K.; Hirotsu, K. *J. Chem. Soc., Chem. Commun.* **1995**, 1531
- <sup>13</sup> Endo, K.; Koike, T.; Sawaki, T.; Hayashida, O.; Masuda, H.; Aoyama, Y. *J. Am. Chem. Soc.* **1997**, *119*, 4117
- <sup>14</sup> Miao, X.; Xu, L.; Li, Y.; Li, Z.; Zhou, J.; Deng, W. *Chem. Commun.* **2010**, *46*, 8830
- <sup>15</sup> Beatty, A. M. *Chem. Rev.* **2003**, *246*, 131
- <sup>16</sup> Griessl, S.; Lackinger, M.; Edelwirth, M.; Hietschold, M.; Heckl, W. M. *Single Mol.* **2002**, *3*, 25
- <sup>17</sup> Kuzmenko, I.; Buller, R.; Bouwman, W. G.; Kjaer, K.; Als-Nielsen, J.; Lahav, M.; Leiserowitz, L. *Science* **1996**, *274*, 2046
- <sup>18</sup> Alonso, C.; Eliash, R.; Jensen, T. R.; Kjaer, K.; Lahav, M.; Leiserowitz, L. *J. Am. Chem. Soc.* **2001**, *123*, 10105
- <sup>19</sup> Russell, V. A.; Ward, M. D. *J. Mater. Chem.* **1997**, *7*, 1123
- <sup>20</sup> Russell, V. A.; Evans, C. C.; Li, W.; Ward, M. D. *Science* **1997**, *276*, 575
- <sup>21</sup> Frostman, L. M.; Ward, M. D. *Langmuir* **1997**, *13*, 330
- <sup>22</sup> Plaut, D. J.; Martin, S. M.; Kjaer, K.; Weygand, M. J.; Lahav, M.; Leiserowitz, L.; Weissbuch, I.; Ward, M. D. *J. Am. Chem. Soc.* **2003**, *125*, 15922
- <sup>23</sup> Martin, S. M.; Kjaer, K.; Weygand, M. J.; Weissbuch, I.; Ward, M. D. *J. Phys. Chem. B.* **2006**, *110*, 14292
- <sup>24</sup> Kitaigorodsky, A. I. *Molecular Crystals and Molecules*; Academic Press: New York, **1973**, 58
- <sup>25</sup> Gerson, A. R.; Roberts, K. J.; Sherwood, J. N. *Acta. Cryst.* **1991**, *B47*, 280
- <sup>26</sup> Ulman, A. *Adv. Mater.* **1990**, *2*, 572; Ulman, A.; Scaringe, R. P. *Langmuir* **1992**, *8*, 894
- <sup>27</sup> Plaut, D. J.; Holman, K. T.; Pivovar, A. M.; Ward, M. D. *J. Phys. Org. Chem.* **2000**, *13*, 858
- <sup>28</sup> Holman, K. T.; Pivovar, A. M.; Swift, J. A.; Ward, M. D. *Acc. Chem. Res.* **2001**, *34*, 107
- <sup>29</sup> Holman, K. T.; Martin, S. M.; Parker, D. P.; Ward, M. D. *J. Am. Chem. Soc.* **2001**, *123*, 4421
- <sup>30</sup> Soegiarto, A. C.; Comotti, A.; Ward, M. D. *J. Am. Chem. Soc.* **2010**, *132*, 14603
- <sup>31</sup> Porter, M. D.; Bright, T. B.; Allara, D. L.; Chidsey, C. E. D. *J. Am. Chem. Soc.* **1987**, *109*, 3559
- <sup>32</sup> Conboy, J. C.; Messmer, M. C.; Richmond, G. L.; *Langmuir* **1998**, *14*, 6722
- <sup>33</sup> Heinz, H.; Vaia, R. A.; Farmer, B. L. *Langmuir* **2008**, *24*, 3727
- <sup>34</sup> Alonso, C.; Kuzmenko, I.; Jensen, T. R.; Kjaer, K.; Lahav, M.; Leiserowitz, L. *J. Phys. Chem. B* **2001**, *105*, 8563
- <sup>35</sup> Swift, J. A.; Reynolds, A. M.; Ward, M. D. *Chem. Mater.* **1998**, *10*, 4159
- <sup>36</sup> Plaut, D. J.; Martin, S. M.; Kjaer, K.; Weygand, M. J.; Lahav, M.; Leiserowitz, L.; Weissbuch, I.; Ward, M. D. *J. Am. Chem. Soc.* **2003**, *125*, 15922
- <sup>37</sup> Alonso, C.; Kuzmenko, I.; Jensen, T. R.; Kjaer, K.; Lahav, M.; Leiserowitz, L. *J. Phys. Chem. B* **2001**, *105*, 8563

- 
- <sup>38</sup> Modak, S.; Datta, A. *J. Phys. Chem.* **1994**, *98*, 1
- <sup>39</sup> Marquardt, D. W. *J. Soc. Ind. Appl. Math.* **1963**, *11*, 431
- <sup>40</sup> Danauskas, S. M.; Li, D.; Meron, M.; Lin, B.; Lee, K. Y. C. *J. Appl. Cryst.* **2008**, *41*, 1187
- <sup>41</sup> Schalke, M.; Lösche, M. *Adv. Colloid Interface Sci.* **2000**, *88*, 243
- <sup>42</sup> Wasserman, S. R.; Whitesides, G. M.; Tidswell, I. M.; Ocko, B. M.; Pershan, P. S.; Axe, J. D. *J. Am. Chem. Soc.* **1989**, *111*, 5852; Richter, A. G.; Durbin, M. K.; Yu, C.-J.; Dutta, P. *Langmuir* **1998**, *14*, 5980
- <sup>43</sup> Nyburg, S. C.; Lüth, H. *Acta Crystallogr. B* **1972**, *28*, 2992
- <sup>44</sup> Tidswell, I. M.; Ocko, B. M.; Pershan, P. S.; Wasserman, S. R.; Whitesides, G. M.; Axe, J. D. *Phys. Rev. B* **1990**, *41*, 1111
- <sup>45</sup> Kulovesi, P.; Telenius, J.; Koivuniemi, A.; Brezesinski, G.; Rantamäki, Viitala, T.; Puukilainen, E.; Ritala, M.; Wiedmer, S. K.; Vattulainen, I.; Holopainen, J. M. *Biophys J.* **2010**, *99*, 2559
- <sup>46</sup> Stenger, P. C.; Wu, G.; Miller, C. E.; Chi, E. Y.; Frey, S. L.; Lee, K. Y. C.; Majewski, J.; Kjaer, K.; Zasadzinski, J. A. *Biophys J.* **2009**, *97*, 777
- <sup>47</sup> Hodges, C. S.; Neville, F.; Konovalov, O.; Hammond, R. B.; Gidalevitz, D.; Hamley, I. W. *Langmuir* **2006**, *22*, 8821
- <sup>48</sup> Vaknin, D.; Kelley, M. S.; Ocko, B. M. *J. Chem. Phys.* **2001**, *115*, 7697
- <sup>49</sup> Garnaes, J.; Larsen, N. B.; Bjørnholm, Jørgensen, M. Kjaer, K.; Als-Nielsen, M. Jørgensen, J. F.; Zasadzinski, J. A. *Science* **1994**, *264*, 1301
- <sup>50</sup> Jiang, P.; Sun, H.; Shen, R.; Shi, J.; Lai, C. *J. Mol. Struct. Theochem* **2000**, *528*, 211
- <sup>51</sup> Koga, T.; Kawazumi, H.; Nagamura, T.; Ogawa, T. *Anal. Sci.* **1992**, *8*, 259.
- <sup>52</sup> Song, C.; Ma, X.; Schmitz, A. D.; Schobert, H. H. *Appl. Catal. A-Gen.* **1999**, *182*, 175

# Chapter 4

## Low-Density Self-Assembled Monolayers Based on Integral Spacer

### 4.1. Introduction

The GS based LB films discussed in Chapter 2 exhibited poor stability in most conditions, so we decided to examine low-density host monolayers based on covalently bound self-assembled monolayers (SAMs). The objectives the works were (1) to demonstrate effective methodologies to prepare low-density self-assembled monolayer (LDSAM) systems possessing integral spacer molecules and reactive groups that bind to a substrate; and (2) examine various integral spacer molecules and determine whether they can create low-density structures for the inclusion of complementary guest molecules.

The functionality of surfaces plays an important role in many applications such as catalysis, sensing, and bio-compatibility,<sup>1</sup> which can benefit from distinctive chemical and physical surface properties. Thus, careful design and control of surface properties can be of great benefit in materials and surface sciences. Self-assembled monolayers (SAMs), Langmuir-Blodgett films (LB films), and other surface-confined assemblies have long been

acknowledged as a practical strategy for creating tailor-made functional surfaces. Current techniques for surface functionalization range from the very simple – random physical adsorption of functional molecules – to more complex methods requiring the synthesis of  $\alpha$ - $\omega$  molecules possessing the desired functional moiety at one end and another moiety designed to interact with the substrate at the other end – either a hydrophilic head group (LB films) or a reactive group (SAMs) designed to covalently bond with the surface. While the development of methods for synthetically preparing surfaces with specific physical or chemical properties would be of significant benefit, it has limitations: (i) difficult organic synthesis required to produce  $\alpha$ - $\omega$  molecules with a reactive head group at one end of the molecule and the desired functional group at the opposite end; and (ii) incapability of regenerating the surface properties of a substrate which depends on the terminal functional group. More simplified and improved concepts could be borrowed from 3-D crystal engineering such as host-guest inclusion complexes.<sup>2</sup> Plaut et al. have established in their experiments that it is possible to form ternary host-guest Langmuir monolayers at the air-water interface, wherein guanidinium spacer molecules from the aqueous subphase interact with alkane-sulfonate amphiphiles to form cavities.<sup>3</sup> Structurally homologous and diverse alkane substituted functional guest molecules can then be inserted into these cavities. These host-guest monolayers can be transferred to solid substrates through LB deposition in order to form functionalized surface, however, surface coatings formed via Langmuir-Blodgett technique have several drawbacks despite precise control over film thickness. LB films are not strongly bound to the solid surface, usually relying on ionic interactions and van der Waal's forces to remain on the substrate; and LB films are limited to planar or near-planar substrates, limiting their application to materials and devices with more complex geometries. Thus, the creation of self-assembled host-guest complexes promises a solution to both of these issues, as they covalently bond with the substrate and assemble from solution, allowing them to coat surfaces that may possess extreme curvatures including micro- and nano-particles. These systems would act as interface templates without altering bulk performance and would have the capacity to regenerate the functionality of a surface through guest insertion and exchange after film formation is complete.

In this study, we demonstrate effective methodologies to prepare low-density self-

assembled monolayer (LDSAM) systems possessing integral 'spacer' moieties and reactive groups that bind to a substrate. For these systems, a bulky organic molecule such as an anthracene-derivative with an aldehyde group, an amine group or a hydroxyl group is immobilized on the reactive surface of silicon dioxide (SiO<sub>2</sub>) to form a low-density monolayer in the absence of guest molecules. With various integral spacer molecules, we studied whether they can create low-density structure for the inclusion of complementary guest molecules. The structural characteristics of LDSAMs were characterized using static water contact-angle measurements, FT-IR/ATR, ellipsometry, X-ray photoelectron spectroscopy (XPS), and X-ray reflectivity (XRR).

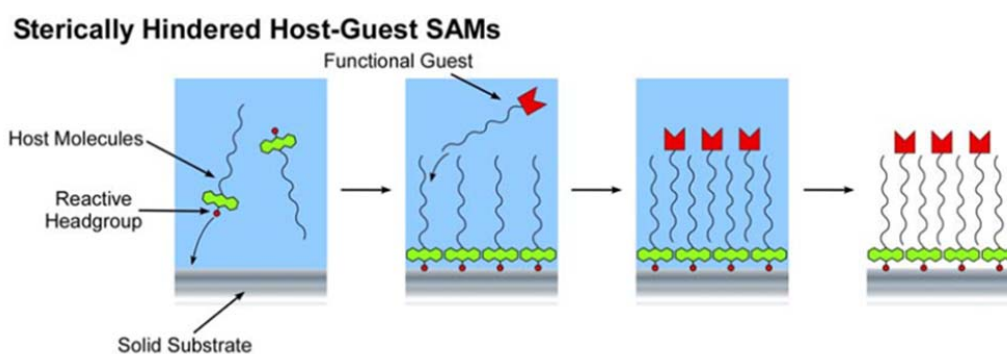


**Figure 4. 1.** Schematic illustration of the formation of a low-density self-assembled monolayers (LDSAMs) formed by host-molecules with integral spacer groups.

## 4.2. Experimental Section

### 4.2.1. Materials

1-bromooctane (99%), 1-bromohexadecane (97%), 1-octadecanol (99%), 1,2-tetradecanediol (90%), 1,8-dihydroxyanthraquinone (96%), 1-phenyl-1-hexadecanol, 4-decyylaniline (97%), 10-chloro-9-anthraldehyde (97%), N-phenylhexadecylamine, (2-methyl-9,10-dihydroanthracene-9,10-diyl)dimethanol, and triethoxychlorosilane (98%) were purchased from Sigma-Aldrich and used without further purification. A p-Si (100) wafer (boron doped, resistivity < 1  $\Omega\text{cm}$ , single polished) was purchased from Wafer World (West Palm Beach, FL).

### 4.2.2. Substrate Preparation

Reactive  $\text{SiO}_2$  surfaces were prepared by dipping pre-cut Si substrates in concentrated  $\text{H}_2\text{SO}_4/\text{H}_2\text{O}_2$  (3:1 by volume) for 15 min at  $100^\circ\text{C}$  (**caution:** Piranha solution is highly explosive, and care should be taken while using this mixture), washing with DI water ( $18\text{M}\Omega\text{cm}$ ), ultra-sonication in a solution of  $\text{HCl}/\text{H}_2\text{O}_2/\text{DI}$  water (1:1:6 by volume) for 30 min at  $50^\circ\text{C}$ , repeated washing with DI water, and heating in an oven at  $120^\circ\text{C}$ . After these procedures, the water contact angle is less than 15 degree.

### 4.2.3. Characterization of LDSAMs

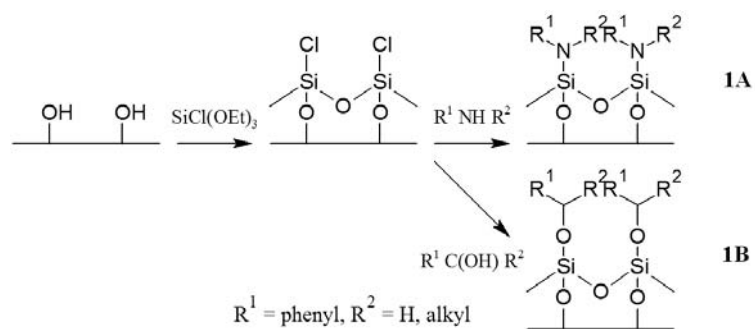
Static contact angles were measured at 5 different points on each sample w via image fitting using a KSV CAM200 contact-angle goniometer. The 5 values were averaged to obtain the reported value. Fourier transform infrared spectra of the organic thin films on Si (100) substrates were collected using a Perkin Elmer Spectrophotometer equipped with an ATR (attenuated total reflectance) attachment. Each spectrum was obtained using 100 scans

at a resolution of  $4 \text{ cm}^{-1}$ . The chemical composition of the host-monolayer was determined using a Perkin-Elmer PHI Quantera SXM-03 scanning X-ray photoelectron spectrometer (Al  $K_{\alpha}$  photon energy of 280 eV) located in the Nano-scale characterization and Fabrication Laboratory (NCFL) at Virginia Tech. The source was run at 48.1 W and electron-take-off angles of  $45^{\circ}$  to the normal surface were used. X-ray reflectivity data were measured using synchrotron radiation at the bending magnet X-ray diffraction beam line BL2-1 of the Stanford Synchrotron Research Light source (Menlo Park, CA). By use of a Si (111) double crystal monochromator, a wavelength,  $\lambda$ , of 0.154nm was selected with  $\Delta E/E = 5 \times 10^{-4}$ . X-rays were focused onto the sample by Rh-coated mirror and the sample was mounted on a Huber 2-circle goniometer and a high resolution crystal-analyzer detector was used. The sample was continuously translated to minimize the effect of beam damage on the sample. The reflectivity data were analyzed using a non-linear least-square fitting program, StochFit, with a multi-box model and the minimum number of constraints and the thickness of the host-monolayers was obtained in the direction normal to the surface.

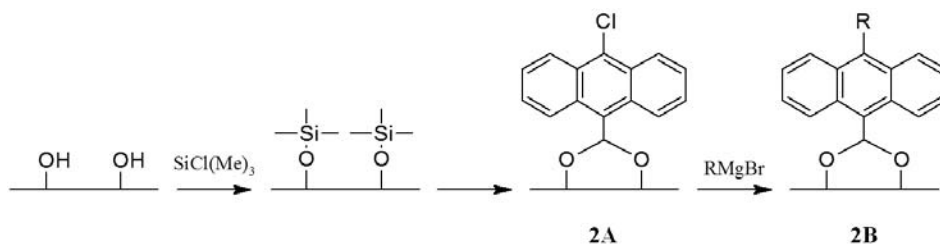
#### 4.2.4. Stepwise Reaction for the Formation of LDSAMs

LDSAMs are created in a stepwise fashion by first creating a monolayer of bulky anthracene derived spacer molecules and then attaching a long alkane chain to the spacer. Four strategies are employed to create LDSAMs on hydroxylated Si substrates: (1) treatment of the surface with trimethoxychlorosilane, followed by the reaction with secondary amine or secondary alcohol containing spacer groups and long alkane chains (**Scheme 4.1**); (2) acetalization of 10-chloro-9-anthraldehyde at the surface is followed by the Grignard addition of long alkane chains (**Scheme 4.2**); (3) treatment of the surface with triethoxychlorosilane followed by the reaction with 1,8-dihydroxyanthraquinone and the Grignard addition of long alkane chains (**Scheme 4.3**); (4) silyl ether attachment of (2-methyl-9,10-dihydroanthracene-9,10-diyl) dimethanol followed by the addition of long-alkane chains (**Scheme 4.4**)

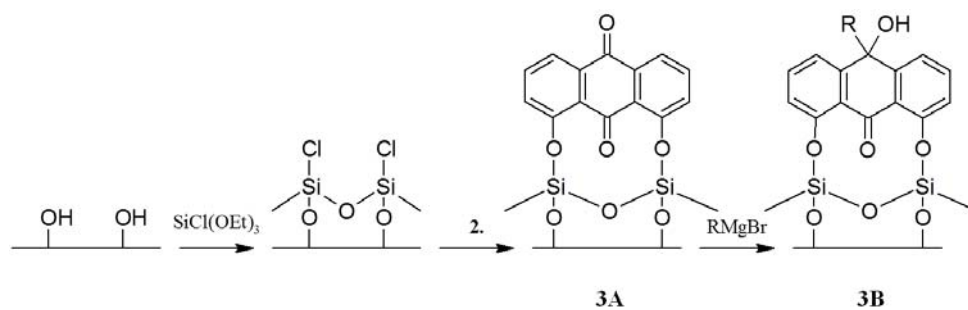
**Scheme 4.1.**



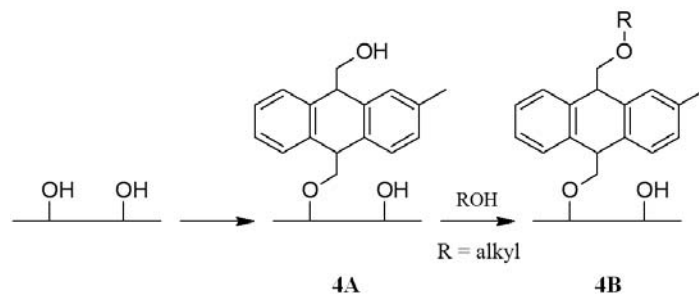
**Scheme 4.2.**



**Scheme 4.3.**



**Scheme 4.4.**



**1A:** hydroxylated SiO<sub>2</sub> substrates are immersed in a 1% solution of triethoxychlorosilane in anhydrous toluene for 18 hours at room temperature, followed by the immersion in a 10mM solution of R-NH<sub>2</sub>, R<sub>1</sub>, R<sub>2</sub>-NH, or R<sub>1</sub>, R<sub>2</sub>-CHOH.

**2A:** hydroxylated SiO<sub>2</sub> substrates are immersed in a 1% solution of chlorotrimethylsilane in anhydrous toluene for 1 hour at room temperature, followed by the immersion in a 10-chloro-9-anthraldehyde solution in anhydrous dichloromethane for 3 days at 150°C.

**3A:** hydroxylated SiO<sub>2</sub> substrates are immersed in a 1% solution of triethoxychlorosilane in anhydrous toluene for 18 hours at room temperature, followed by the immersion in a 10mM solution 1,8-dihydroxyanthraquinone in anhydrous toluene for 3 days at 150°C.

**4A:** hydroxylated SiO<sub>2</sub> substrates are immersed in a 5mM solution of (2-methyl-9,10-dihydroanthracene-9,10-diyl)dimethanol in anhydrous benzene for 3 days at 200°C.

Following the addition of the spacer group layer, the substrates are rinsed to remove residual chemicals on the surface as follows: (i) ultra-sonication in toluene for 15 min; (ii) sonication again in toluene for 15min; (iii) ultra-sonication in chloroform for 15min.

**2B, 3B:** 1-octanemagnesium bromide and 1-hexadecylmagnesium bromide Grignard reagents are prepared by dissolving 1-bromooctane (2.45g, 12.7mmoles, 99% pure) or 1-bromohexadecane (3.89g, 12.7mmoles, 97% pure) in 25ml of anhydrous diethyl ether. The solutions are then added to a 100ml round bottom flask containing magnesium powder (0.61g, 25.3mmoles). The mixture is heated slightly to initiate the reaction and refluxed under nitrogen with stirring for 4 hours. Grignard reactions are performed by transferring the Grignard reagent solution (0.5M in diethyl ether) via a metal cannula to a round bottom flask containing the chlorine- (**2A**) or carbonyl- (**3B**) terminated substrates and incubated for 2 days at 80°C under nitrogen. Following the Grignard reaction, the substrates are rinsed with tetrahydrofuran (THF) then with ethanol and dried under nitrogen.

**4B:** substrates with monolayer formed from 4A is immersed in a 25mM solution of 1-octadecanol or 1,2-tetradecanol in anhydrous benzene for 72 hrs at 200°C.

### 4.3. Results and Discussion

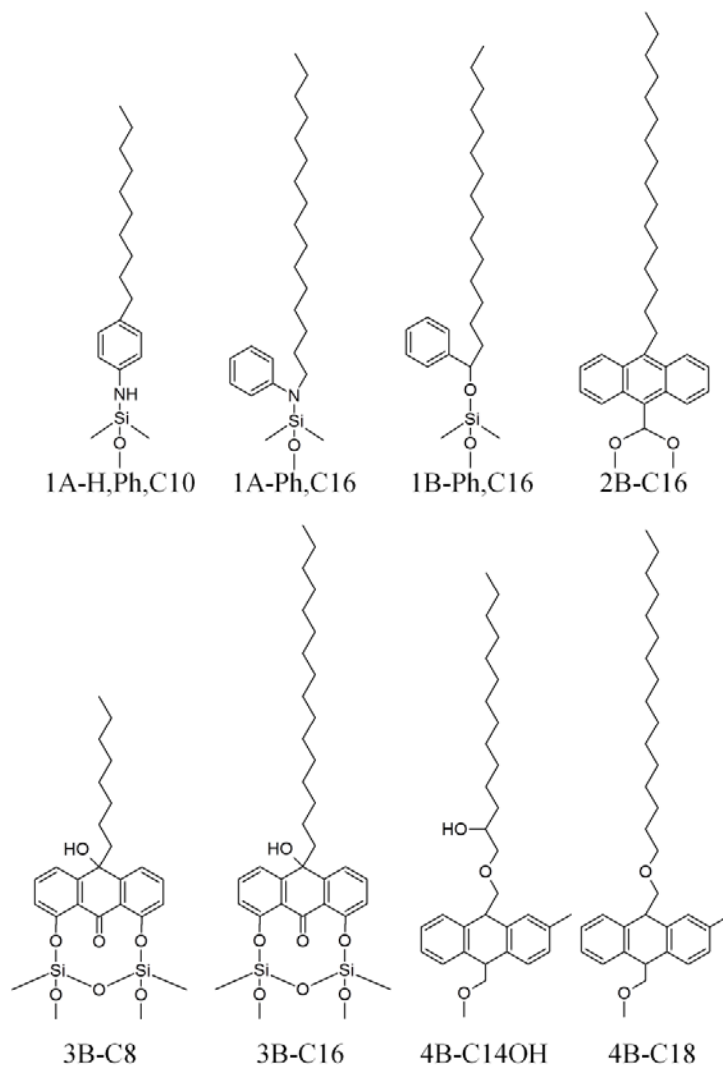


**Figure 4. 2.** Schematic of low-density self-assembled host-monolayers on hydroxylated Si (100) substrates. 1A(H,Ph,C10), 1A(Ph,C16), and 1B(Ph,C16) are formed in a one-step process using secondary alcohol and amine precursors. 2B(C16), 3B(C8), 3B(C16), 4B(C14OH), and 4B(C18) are formed in a stepwise fashion by forming a monolayer of the bulky anthracene precursors and then subsequently adding a long alkane tail.

Yam et al.'s<sup>4,5,6,7</sup> work has shown that an organosilicon-amine route can be used to construct densely packed thin films of chromophores. Based on their work, we prepared low-density self-assembled monolayers of primary amines, secondary amines, or secondary alcohols through the reaction of surface-anchored chlorosilane with 4-decylaniline (1A-

**H,Ph,C10**), 1-phenyl-1-hexadecanol (**1B-Ph,C16**), and N-phenylhexadecylamine (**1A-Ph,C16**) respectively (Scheme 3.1). The secondary amines and alcohols have both a phenyl spacer group and a long alkane-tail. The resulting monolayer molecules are depicted in Figure 4.2. Anthracene-derivatives containing reactive groups which are capable of binding to the chlorinated surface were used to form self-assembled monolayers to which alkane chains were subsequently added. Alkane chains were added to the halogen terminated 10-chloro-9-anthraldehyde monolayers and the carbonyl-terminated 1,8-dihydroxyanthraquinone monolayers using Grignard reactions to produce LDSAMs with 8 and 16 carbon tails (**2B-C16**, **3B-C8**, **3B-C16**)<sup>8,9</sup> as depicted in Figure 4.2 and schemes 3.2 and 3.3. Alkane chains were added to the hydroxyl-terminated (2-methyl-9,10-dihydroanthracene-9,10-diyl) dimethanol through a silyl ether linkage<sup>10</sup> (**4B-C14OH**, **4B-C18**) also depicted in Figure 4.2 and scheme 3.4.

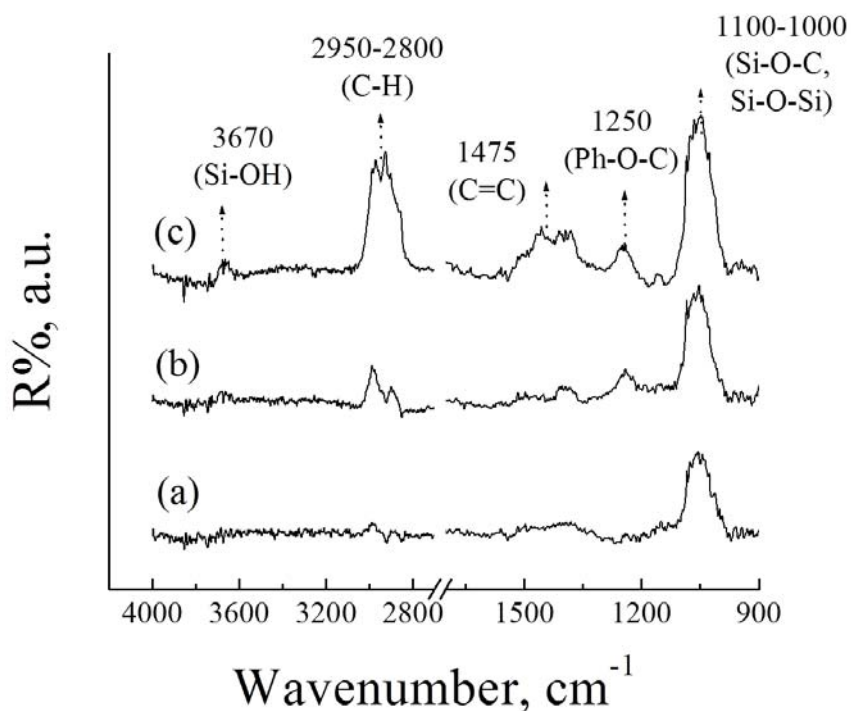


**Figure 4. 3.** FTIR-ATR spectra for monolayers of (a) triethoxychlorosilane (coupling layer), (b) 1A-H,Ph,C10, and (c) 4B-C18, respectively.

FTIR spectra were obtained for the LDSAMs and intermediates using an ATR geometry, and are shown in Figure 4.3. A hydroxyl-terminated Si (Si-OH) substrate was used as a background. The absorption peak corresponding to the Si-OH stretching mode is observed at around  $3670\text{ cm}^{-1}$ . After the formation of coupling layer of triethoxychlorosilane, the Si-OH absorption is decreased, and a broad band in the  $1130\sim 1000\text{ cm}^{-1}$  is observed, which is attributed to the vibrations of the -Si-O-Si- bridges and -Si-O- surface bonds.<sup>11</sup> All forms of SiO<sub>2</sub> show a strong band at  $1110\sim 1080\text{ cm}^{-1}$ , but no peaks are observed in this range. As siloxane chains become longer or branched, -Si-O-Si- absorption becomes broader and more complex, showing several overlapping bands. In the case of the 1A-H,Ph,C10 host monolayer, it is not easy to distinguish the -Si-O-Si- absorption from -Si-N-C- absorption as both bonds have a similar absorption peak in the  $1100\sim 1050\text{ cm}^{-1}$  range,<sup>12,13,14</sup> but the spectrum exhibits a peak at  $1243\text{ cm}^{-1}$  due to the stretching mode of aniline moiety. A strong band in the  $1100\sim 1000\text{ cm}^{-1}$  range for the 4B-C18 host is assigned to -Si-O-C- linkage as the 4B-C18 host monolayer was attached directly to a Si-OH substrate without the aid of a coupling layer. The FTIR results demonstrate that host monolayer is formed via a -Si-O-C- or -Si-N-C- linkage.<sup>15,16,17</sup>

**Table 4. 1.** Peak frequencies of the CH<sub>2</sub> asymmetric and symmetric vibration mode obtained from FTIR-ATR measurement of various LDSAMs.

Host-monolayer on Si (100)	$\nu_a(\text{CH}_2), \text{ cm}^{-1}$	$\nu_s(\text{CH}_2), \text{ cm}^{-1}$
-SiO <sub>2</sub> /coupling/2A *		
-SiO <sub>2</sub> /coupling/1A-H,Ph,C10		
-SiO <sub>2</sub> /coupling/1A-Ph,C16	2923	2853
-SiO <sub>2</sub> /coupling/1B-Ph,C16	2925	2853
-SiO <sub>2</sub> /coupling/3A*	2917	
-SiO <sub>2</sub> /coupling/3B-C8		
-SiO <sub>2</sub> /coupling/3B-C16	2929	2857
-SiO <sub>2</sub> /4A*	2932	2856
-SiO <sub>2</sub> /4B-C14OH	2924	2853
-SiO <sub>2</sub> /4B-C18	2926	

\* Intermediate host-monolayer before attaching the long-alkane chain

All LDSAM samples exhibit a CH<sub>2</sub> stretching vibration between 3000 and 2800 cm<sup>-1</sup>. The asymmetric CH<sub>2</sub> stretching vibration is generally observed between 3000 cm<sup>-1</sup> and 2900 cm<sup>-1</sup>, while the CH<sub>2</sub> symmetric stretch appears between 2900 cm<sup>-1</sup> and 2800 cm<sup>-1</sup>. Table 4.1 lists the wavenumbers at which the CH<sub>2</sub> absorption peaks were observed for various LDSAMs. The LDSAMs exhibit similar peak locations for  $\nu_a(\text{CH}_2)$  and  $\nu_s(\text{CH}_2)$  respectively, indicating similar densities of the alkane chains. The values of  $\nu_a(\text{CH}_2)$ , between 2923 cm<sup>-1</sup> and 2932 cm<sup>-1</sup>, and  $\nu_s(\text{CH}_2)$ , between 2853 cm<sup>-1</sup> and 2857 cm<sup>-1</sup>, are characteristic of liquid-like disordered chains rather than closely packed alkane chains (peaks at 2918 and 2850 cm<sup>-1</sup> are expected for an all-trans ordered crystalline phase).<sup>18,19,20</sup> The liquid-like values of the peak positions indicate that the alkane chains are unable to form a close-packed structure due to the presence of the aromatic spacer within the LDSAMs.

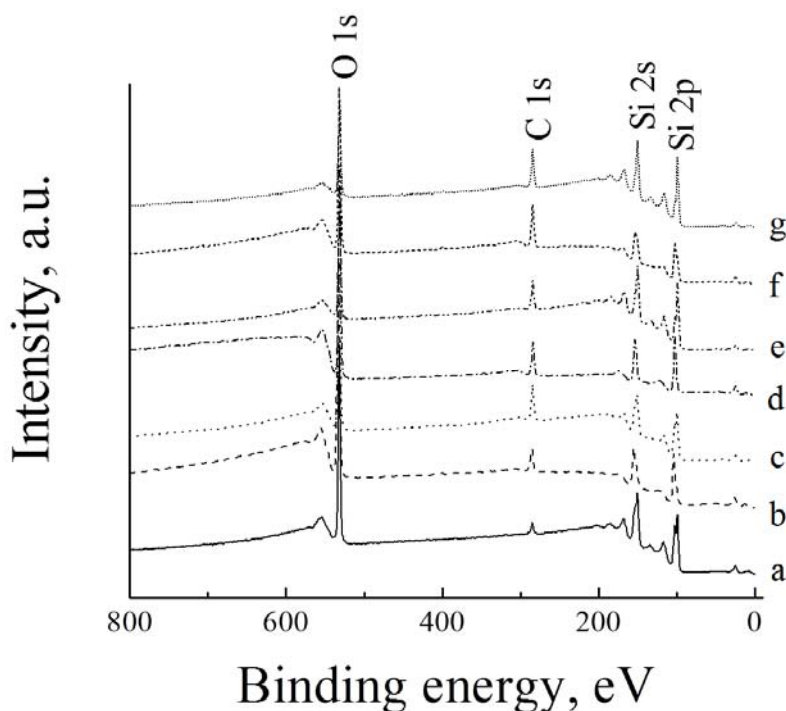


**Figure 4. 4.** XPS survey spectra for monolayers of (a) pure silicon treated with Piranha solution, (b) triethoxychlorosilane, (c) 1A-H,Ph,C10, (d) 1A-Ph,C16, (e) 1B-Ph,C16, (f) 3B-C16 through grignard reaction, and (g) 4B-C18.

Figure 4.4 depicts XPS survey scans for the hydroxylated-silicon substrate<sup>21,22,23</sup> and for the LDSAMs. The survey spectra shows three elements: silicon (2s, 150 eV; 2p, 99 eV), carbon (1s, 285 eV), and oxygen (1s, 532 eV).<sup>24,25</sup> When compared with the spectra of the hydroxylated substrate, the intensity of C 1s peak increases significantly following LDSAM fabrication, while the relative intensities of the O 1s and Si 2p peaks decrease as listed in Table 4.2.

**Table 4. 2.** The surface chemical compositions determined by XPS quantitative analysis of each LDSAMs.

Host-monolayer on Si (100)	XPS Quantitative Analysis, at %			
	C	O	Si	C/O
Clean Si wafer (SiO <sub>2</sub> )	7	52	40	<u>0.14</u>
-SiO <sub>2</sub> /SiCl(OEt) <sub>3</sub> *	15	59	26	<u>0.26</u>
-SiO <sub>2</sub> /1,2-tetradecanediol	<b>34</b>	35	30	<u>0.97</u>
-SiO <sub>2</sub> /coupling/2A *	-	-	-	
-SiO <sub>2</sub> /coupling/1A-H,Ph,C10	24	42	33	0.58
-SiO <sub>2</sub> /coupling/1A-Ph,C16	21	53	26	0.40
-SiO <sub>2</sub> /coupling/1B-Ph,C16	21	39	39	0.54
-SiO <sub>2</sub> /coupling/3A	29	48	23	0.60
-SiO <sub>2</sub> /coupling/3B-C8	-	-	-	
-SiO <sub>2</sub> /coupling/3B-C16	28	45	26	0.62
-SiO <sub>2</sub> /4A *	25	34	<b>40</b>	0.74
-SiO <sub>2</sub> /4B-C14OH	27	34	<b>38</b>	0.79
-SiO <sub>2</sub> /4B-C18	28	31	<b>40</b>	0.90

\* Intermediate host-monolayer before attaching the long-alkane chain

The small C 1s peak on a hydroxylated-Si substrate is due to surface contamination, which is similar for all surfaces exposed to air. As shown in Table 4.2, the XPS data for 4A exhibits a slight change in the surface concentration of the Si atoms as 4A is attached directly to the silicon substrate via a -Si-O-C- linkage. The surface oxygen concentrations of LDSAMs built on a coupling layer of triethoxychlorosilane (1A through 3B) are mostly less than those of the hydroxylated-silicon substrate, due to the presence of the thick coupling layer. It has been reported that silane coupling agents such as triethoxychlorosilane form

thick polymeric layers on the surface when there is a sufficient amount of water in the system.<sup>26</sup> It is interesting to note that the carbon concentrations in the LDSAMs are less than 30%, while the carbon concentrations of the 1,2-tetradecanediol SAM is ca. 34%. We believe that the linear alkane structure of 1,2-tetradecanediol results in a more closely packed SAM structure than in the LDSAMs containing a spacer group such as anthracene.

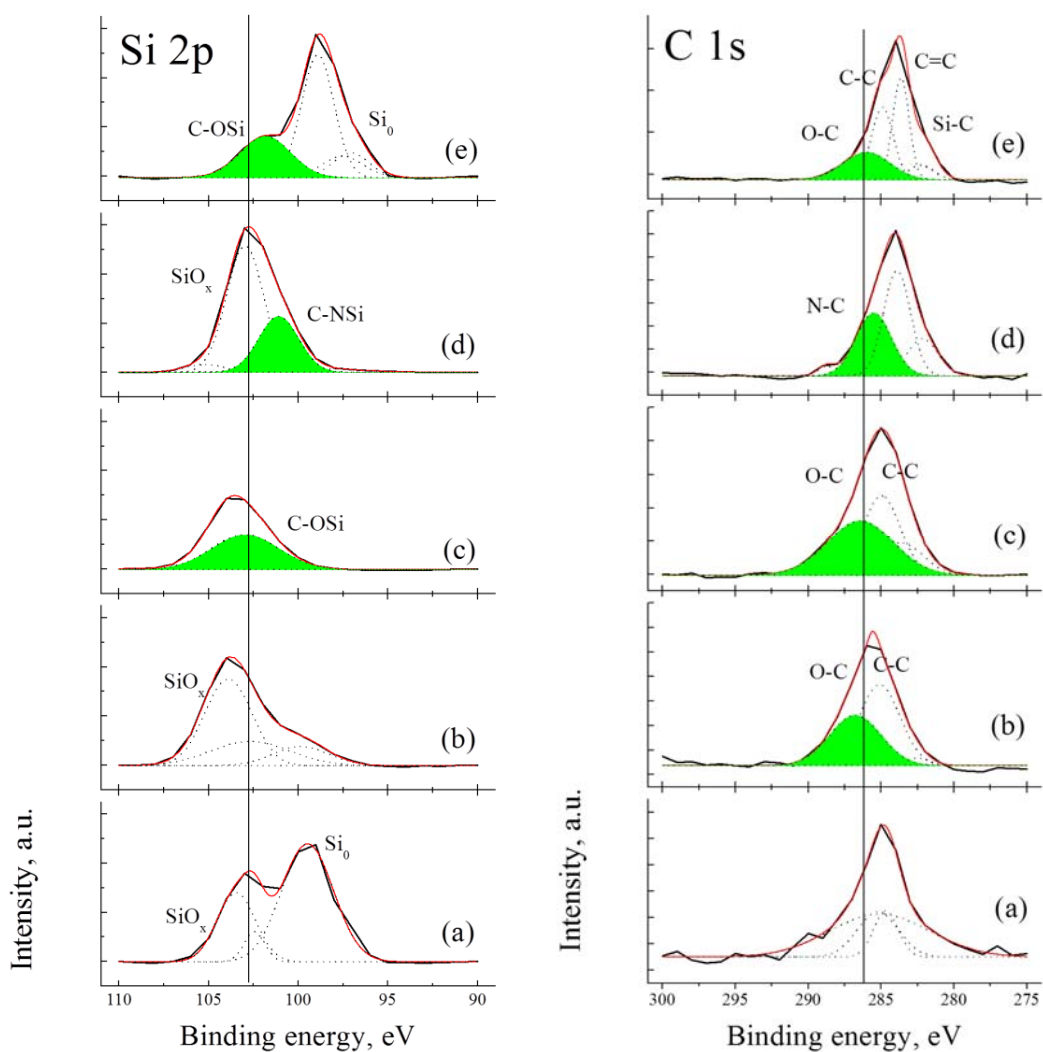


**Figure 4. 5.** XPS spectra of the Si 2p and the C 1s regions of (a) pure silicon, (b) coupling layer of triethoxychlorosilane, (c) 1B-Ph,C16, (d) 1A-Ph,C16, and (e) 4B-C18.

To confirm the presence of -Si-O-C- and -Si-N-C- bonds in the LDSAMs, the XPS spectra of the Si 2p and the C 1s region are deconvoluted by fitting the data with a number of Gaussian peaks. As shown in Figure 4.5b, the Si 2p peak for the coupling layer shows a noticeable decrease in the intensity of Si (at 99 eV), indicating the presence of a thick triethoxychlorosilane layer.<sup>27,28</sup> The C 1s peak for the coupling layer shows C-C (at 285 eV) and C-O (at 286.5 eV), suggesting an incomplete hydrolysis of triethoxychlorosilane. The formation of LDSAMs via -Si-O-C- or -Si-N-C- linkages is apparent in the Si 2p regions with peaks at 101.1 and 102.1 eV assigned to the -C-O-Si- and -C-N-Si- bonds, respectively. The presence of C-O (at 286.5 eV) and C-N (at 285.5 eV) bonds supports this conclusion.

Static contact angle measurements were performed to characterize the surfaces before and after LDSAM fabrication. The LDSAMs were also characterized using ellipsometry and X-ray reflectivity (XRR). The data obtained from contact-angle measurements, ellipsometry, and XRR for the LDSAMs depicted in Figure 4.2 is presented in Table 4.3. Prior to LDSAM fabrication, the hydroxylated Si substrates exhibited static water contact angles less than 15°. Following the formation of anthracene-derivative monolayers (**2A**, **3A/B**, or **4A/B**), the static water contact-angles increased to a value between 55° and 105°, depending on the nature of the surface functionality such as anthrylmethanol-, halogen-, carbonyl-, and methyl-groups respectively. Although these contact angles do not provide direct structural information about the monolayers, they are useful indicators of their quality.<sup>29</sup> For example, the static water contact angle of 105° obtained for the SAM formed using 1-phenyl-1-hexadecanol (**1B-Ph,C16**) is slightly lower than the value of 110° reported for the SAM of octadecyltrichlorosilane (**OTS**) on silica-based surfaces,<sup>30</sup> and is within the expected range for a surface containing densely packed alkane chains. In contrast the SAM formed using N-phenylhexadecylamine (**1A-Ph,C16**) exhibits a contact angle of 90°, suggesting a more open structure with a lower density packing of alkane chains. Similarly, the SAMs formed by alkylated 1,8-dihydroxyanthraquinone (**3B**) exhibit contact angles of 88° and 95° for a C8 and C16 chain, respectively. The lower contact angle of water on these SAMs may be due to the disordered and loosely packed structure of the alkane chains caused by the presence of the bulky spacer molecule. In addition, the contact angle increases as the length of the alkane tail increases. SAMs formed via an alkylated monolayer of (2-methyl-9,10-dihydroanthracene-

9,10-diyl) dimethanol (**4B**) exhibit contact angles of 91° and 87° for C14 and C18 chains respectively, also suggesting lower density packing of the alkane chains in the monolayer.

Ellipsometry was used to determine the LDSAM thicknesses and synchrotron X-ray reflectivity measurements were performed to determine the electron density in the vertical direction. Figure 4.6 shows X-ray reflectivity results for several SAMs. None of the reflectivity data exhibit a sharp minimum but an approximate value for film thickness can be calculated using the location of the first minimum,<sup>31</sup> which is caused by destructive interference between X-rays reflected from the top and bottom surfaces of the film. For example, the host-monolayer of 4-decylniline exhibits a critical wave vector of  $q_c \approx 0.023 \text{ \AA}^{-1}$  and the position of the first minimum is  $q = 0.0755 \text{ \AA}^{-1}$ . Taking the refraction correction ( $L(q^2 - q_z^2)^{0.5} = \pi$ ) into account,<sup>32</sup> the thickness for 4-decylniline corresponds to a thickness of 44 Å. This value is much thicker than the expected value of ca. 20 Å calculated using the expression  $L = 1.265n + 1.5 \text{ \AA}$  for a fully extended alkane chain, and including the aniline moiety. The corresponding ellipsometric data also shows that the film is thicker than expected for a monolayer film. The higher than expected thicknesses are common throughout all of the samples. The thickness of the coupling layer of triethoxychlorosilane was determined by ellipsometry to be ca. 80 Å, although this value is expected to vary between samples. This suggests that the calculated thicknesses using the primary minimum in the XRR curve, which vary from 30 to 200 Å, include the thickness of triethoxychlorosilane layer.

To obtain more accurate information about the film thickness, a detailed analysis of the XRR data was performed using StochFit and either a 2-box or 3-box model,<sup>33</sup> the results of which are presented in Table 4.3. As shown in Figure 4.7, the coupling layer of triethoxychlorosilane was considered to be part of the same layer as the native oxide for modeling purposes. Using a 2-box model, for example, a thickness of 11.3 Å with a normalized electron density of 0.109 ( $=\rho/\rho_{\text{Si}}$ ) was obtained for the host-monolayer of 4-decylniline (**1A-H,Ph,C10**). These values are significantly lower than the length of a fully extended chain length and the electron density of closely packed alkane chains ( $\rho/\rho_{\text{Si}} = 0.40$ ). In this case, the thickness of the coupling layer of triethoxychlorosilane estimated was ca. 47.3Å.

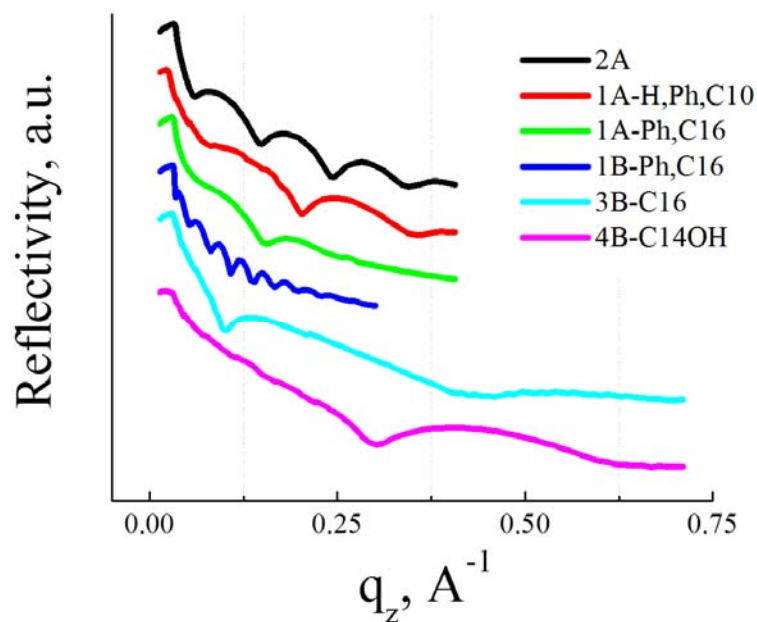


**Figure 4. 6.** X-ray reflectivity curves of six different LDSAMs (2A, 1A-H,Ph,C10, 1A-Ph,C16, 1B-Ph,C16, 3B-C16, and 4B-C14OH).

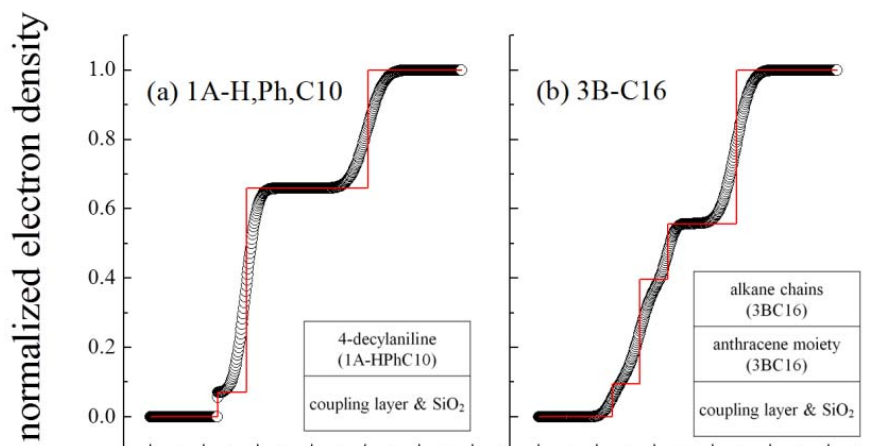


**Figure 4. 7.** Box model of the normalized electron density of (a) 1A-H,Ph,C10 and (b) 3B-C16 monolayer. The layer thickness estimated was determined to be 11.3 and 19.5 for (a) and (b) respectively.

The thickness of 1A-PhC16 and 1B-PhC16 monolayers, as shown in Table 4.3, corresponds to the expected length for fully extended alkane chains. As such, we believe that SAM structure with a single phenyl spacer group such as 1A-PhC16 or 1B-PhC16 does not result in a significantly expanded structure and would be unsuitable for accommodating guest molecules. In contrast, modeling of XRR data for the other LDSAMs studied resulted in both lower thicknesses and densities. These results are consistent with the formation of low-density films due to the presence of integral spacer groups in the monolayer structures. An n-alkane thiol or alkane siloxane monolayer with a small head group can be well-organized via van der Waals interactions between adjacent alkane-chains and can form a close-packed structure.<sup>34,35</sup> The thicknesses of such uniform films are generally a little less than the expected values for fully extended alkane chains normal to the surface. The long-alkane chains in the LDSAMs are sterically hindered from forming a close-packed structure, and are thermally disordered as the alkane chains attached to the bulky spacer groups severely tilt or bend to fill the void spaces (cavities) as depicted in Figure 4.8. This leads to the observed decrease in the thickness and the electron density of the films.

**Table 4. 3.** Static contact angles, ellipsometric thickness, and thickness and electron density determined from X-ray reflectivity profiles with 2 or 3 boxes model. The thickness of host monolayer is shown in bold.

Host-monolayer on Si (100)	CA <sub>H2O</sub> , deg	T <sub>E</sub> , Å	T <sub>X</sub> , Å	ρ/ρ <sub>Si</sub>
	±3°	±3	coupling / host ±1	
Clean Si wafer (SiO <sub>2</sub> )	12	-	-	-
-SiO <sub>2</sub> /coupling(SiCl(OEt) <sub>3</sub> ) *	83	77.6	30~200	-
-SiO <sub>2</sub> /coupling/2A*	88	88	64.4 / <b>12.9</b>	0.109
-SiO <sub>2</sub> /coupling/1A-H.Ph,C10	90	37.3 **	47.3 / <b>11.3</b>	0.069
-SiO <sub>2</sub> /coupling/1A-Ph,C16	93	-	64.2 / <b>18.2</b>	0.169
-SiO <sub>2</sub> /coupling/1B-Ph,C16	105	36.5 **	209.4 / <b>21.2</b>	0.126
-SiO <sub>2</sub> /coupling/3A*	88	65.5	45.5 / <b>8.2</b>	0.281
-SiO <sub>2</sub> /coupling/3B-C8	91	-	44.7 / <b>17.0</b>	0.096
-SiO <sub>2</sub> /coupling/3B-C16	95	-	23.4 / <b>19.5</b>	0.245
-SiO <sub>2</sub> /4A*	55	-	0 / <b>6.3</b>	0.341
-SiO <sub>2</sub> /4B-C14OH	91	29.3	0 / <b>14.0</b>	0.181
-SiO <sub>2</sub> /4B-C18	87	-	-	-

\* Intermediate host-monolayer before attaching the long-alkyl chain

\*\* The thickness of coupling layer was controlled by changing the immersion time

T<sub>E</sub>: thickness measure by ellipsometry

T<sub>X</sub>: thickness estimated using XRR data

ρ<sub>Si</sub>: electron density of silicon

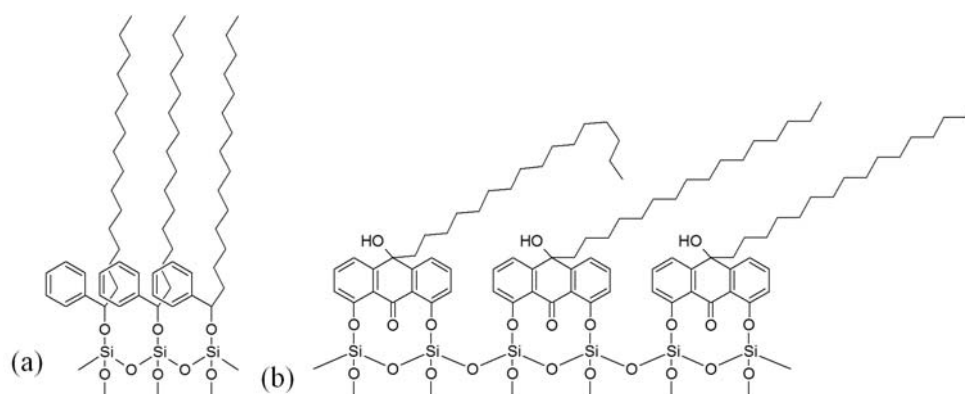


**Figure 4. 8.** Schematic drawing of anticipated monolayer structure of (a) 1BPhC16 and (b) 3BC16. The 1BPhC16 monolayer can have a densely-packed structure, whereas low-density SAMs such as 3BC16 allow alkane chains to tilt or bend to fill the cavities. This leads to a decrease in the thickness and the electron density of the films.

#### 4.4. Conclusions

We have fabricated low-density self-assembled monolayers (LDSAMs) on hydroxyl-terminated silicon (100) substrates using either one-step or multi-step synthetic approaches, based on molecules containing integral spacer moieties and long-alkane chains. The resulting monolayers were characterized using static water contact angle measurements, FTIR, ellipsometry, XPS, and XRR (X-ray reflectivity). These results confirmed that LDSAMs using an anthryl spacer have a -Si-O-C- linkage at the SAM/Si interface, and they do not have a densely packed monolayer quality as would be expected for a non-sterically hindered alkyltrichlorosilane on Si. Thus, the resulting LDSAMs (with voids) may be capable of accommodating other hydrocarbon chains (guest molecules) through intercalation for the formation of host-guest assemblies. Further study will be conducted to examine the capabilities of LDSAMs to intercalate guest molecules. These capabilities will lead to potential application area such as catalysis, sensing, and bio-compatibility.

#### 4.5. Summary

We have synthesized low-density self-assembled monolayers (LDSAMs) to act as hosts for the creation of functional host-guest thin films. LDSAMs containing pre-existing cavities between long alkane chains have been prepared on Si (100) (Si/SiO<sub>2</sub>) substrates via a stepwise reaction based on hydrolytic or silane chemistry. In a stepwise reaction, integral spacers are anchored to the substrates directly or using SiCl(OEt)<sub>3</sub> through the Si-O-C linkage, and then long alkane chains are attached to the spacers. The monolayer density is controlled through the inclusion of a bulky organic group such as an anthracene-derivative. The resultant monolayers were characterized by contact angle measurements, Fourier transform infrared spectroscopy, X-ray photoelectron spectroscopy, and X-ray specular reflectivity and the results confirm that low-density SAMs were produced on the substrates. The analysis of FTIR spectra in the 1100~1000 cm<sup>-1</sup> region confirms the formation of LDSAMs via -Si-O-C- or -Si-N-C- linkages, and the presence of -Si-O-C- or -Si-N-C-

linkages in the LDSAMs is also confirmed via a curve fitting of the Si 2p and the C 1s regions of the XPS spectra. In addition, structural analysis of the alkyl chains using FTIR indicates the presence of characteristic of liquid-like disordered alkane chains. XRR analysis for the LDSAMs also exhibits lower thicknesses and electron densities than expected for close-packed alkane chains. The results confirm the formation of low-density self-assembled monolayers with cavities. These cavities may be used to intercalate desired guest molecules from an external solution in a controllable method.

## 4.6. References

- 
- <sup>1</sup> (a) Berggren, K. K.; Bard, A.; Wilbur, J. L.; Gillaspay, J. D.; Helg, A. G.; McClelland, J. J.; Rolston, S. L.; Philips, W. D.; Prentiss, M.; Whitesides, G. M. *Science* **1995**, *269*, 1255. (b) Kim, E.; Whitesides, G. M.; Lee, L. K.; Smith, S. P.; Prentiss, M. *Adv. Mater.* **1996**, *8*, 139. (c) Hodneland, C. D.; Mrksich, M. *J. Am. Chem. Soc.* **2000**, *122*, 4235. (d) Aswal, D. K.; Lenfant, S.; Guerin, D.; Yakhmi, J. V.; Vuillaume, D. *Anal. Chim. Acta* **2006**, *568*, 84. (e) Phares, N.; White, R. J.; Plaxco, K. W. *Anal. Chem.* **2009**, *81*, 1095
  - <sup>2</sup> Weber, E. In *Topics in Current Chemistry*; Springer-Verlag: Berlin, **1987**; Vol 140
  - <sup>3</sup> Plaut, D. J.; Martin, S. M.; Kjaer, K.; Weygand, M. J.; Lahav, M.; Leiserowitz, L.; Weissbuch, I.; Ward, M. D. *J. Am. Chem. Soc.* **2003**, *125*, 15922
  - <sup>4</sup> Yam, C. M.; Tong, S. S. Y.; Kakkar, A. K. *Langmuir* **1998**, *14*, 6941
  - <sup>5</sup> Yam, C. M.; Kakkar, A. K. *Langmuir* **1999**, *15*, 3807
  - <sup>6</sup> Fessenden, R.; Fessenden, J. S. *Chem. Rev.* **1961**, *61*, 361
  - <sup>7</sup> Anderson, H. H. *J. Am. Chem. Soc.* **1952**, *74*, 1421
  - <sup>8</sup> Lockett, M. R.; Smith, L. M. *Langmuir* **2009**, *25*, 3340
  - <sup>9</sup> Nakayama, T.; Matsushima, T.; Murata, H. *Thin solid films* **2009**, *518*, 739
  - <sup>10</sup> Dion, M.; Rapp, M.; Rorrer, N.; Shin, D.; Martin, S. M.; Ducker, W. A. *Colloid Surface A* **2010**, *362*, 65
  - <sup>11</sup> Kim, N. Y.; Laibinis, P. E. *J. Am. Chem. Soc.* **1997**, *119*, 2297
  - <sup>12</sup> Park, Y.; Rhee, S. *J. Non-cryst. Solid.* **2004**, *343*, 33
  - <sup>13</sup> Fracassi, F.; d'Agostino, R.; Bruno, G. *Plasma Process Polym.* **1996**, *Vol. 1*, No. 1
  - <sup>14</sup> Zhang, G.; Fan, X.; Kong, J.; Liu, Y.; Wang, M.; Qi, Z. *Macromol. Chem. Phys.* **2007**, *208*, 541
  - <sup>15</sup> Yang, C.; Choi, C. *J. Korean. Phys. Soc.* **2004**, *45*, 642
  - <sup>16</sup> Kim, C.; Kim, S.; Navamathavan, R.; Choi, C.; Jeung, W. *Thin Solid Films* **2007**, *516*, 340
  - <sup>17</sup> Sano, H.; Maeda, H.; Ichii, T.; Murase, K.; Noda, K.; Matsushige, K.; Sugimura, H. *Langmuir* **2009**, *25*, 5516
  - <sup>18</sup> Tillman, N.; Ulman, A.; Schildkraut, J. S.; Penner, T. L. *J. Am. Chem. Soc.* **1988**, *110*,

---

6136

- <sup>19</sup> Bain, C. D.; Troughton, E. B.; Tao, Y.; Evall, J.; Whitesides, G. M.; Nuzzo, R. G. *J. Am. Chem. Soc.* **1989**, *111*, 321
- <sup>20</sup> Hacker, C. A.; Anderson, K. A.; Richter, L. J.; Richter, C. A. *Langmuir* **2005**, *21*, 882
- <sup>21</sup> Wasserman, S. R.; Tao, Y-T.; Whitesides, G. M. *Langmuir* **1989**, *5*, 1074
- <sup>22</sup> Wasserman, S. R.; Whitesides, G. M.; Tidswell, I. M.; Ocko, B. M.; Pershan, P. S.; Axe, J. *J. Am. Chem. Soc.* **1989**, *111*, 5852
- <sup>23</sup> Major, R. C.; Zhu, X. Y. *Langmuir* **2001**, *17*, 5576
- <sup>24</sup> Nuzzo, R. G.; Zegarski, B. R.; Dubois, L. H. *J. Am. Chem. Soc.* **1987**, *109*, 733
- <sup>25</sup> Castner, D. G. *Langmuir* **1996**, *12*, 5083
- <sup>26</sup> Fadeev, A. Y.; McCarthy, T. J. *Langmuir* **2000**, *16*, 7268
- <sup>27</sup> Lou, J. L.; Shiu, H. W.; Chang, L. Y.; Wu, C. P.; Soo, Y-L.; Chen, C-H. *Langmuir* **2011**, *27*, 3436
- <sup>28</sup> Boukherroub, R.; Morin, S.; Sharpe, P.; Wayner, D. D. M. *Langmuir* **2000**, *16*, 7429
- <sup>29</sup> Folkers, J. P.; Gorman, C. B.; Laibinis, P. E.; Buchholz, S.; Whitesides G. M.; Nuzzo, R. G. *Langmuir* **1995**, *11*, 813
- <sup>30</sup> Tillman, N.; Ulman, A.; Schildkraut, J. S.; Penner, T. L. *J. Am. Chem. Soc.* **1988**, *110*, 6136
- <sup>31</sup> Chason, E.; Mayer, T. M. *Solid State Mater. Sci.* **1997**, *22*, 1
- <sup>32</sup> Tidswell, I. M.; Ocko, B. M.; Pershan, P. S.; Wasserman, S. R.; Whitesides, G. M.; Axe, J. *D. Phys Rev B* **1990** *41* 1111
- <sup>33</sup> Danauskas, S. M.; Li, D.; Meron, M.; Lin, B.; Lee, K. Y. C. *J. Appl. Cryst.* **2008**, *41*, 1187
- <sup>34</sup> Porter, M. D.; Bright, T. B.; Allara, D. L.; Chidsey, C. E. D. *J. Am. Chem. Soc.* **1987**, *109*, 3559
- <sup>35</sup> Ulman, A. *Chem. Rev.* **1996**, *96*, 1533

# Chapter 5

## Host-Guest Assemblies via the Intercalation of Guest molecules on Low-Density Self-Assembled Monolayer

### 5.1. Introduction

The disadvantage of the formation of host-guest assemblies using LDSAMs such as those described in Chapter 4 is that it is not possible to deposit preformed host-guest assemblies, like the LB films discussed in Chapter 3, on the surface. Instead self-assembly of the host monolayer must occur in the absence of guest molecules, followed by intercalation of the functional molecule. The objectives of the works were (1) to investigate the intercalation processes of guest molecules in host-LDSAMs with well-defined cavities using in-situ and ex-situ techniques; and (2) to demonstrate the feasibility of using LDSAMs as host monolayer in order to add functionality to, or to regenerate the functionality of surfaces via the intercalation of functional guests.

The functionality of surfaces plays an important role in many applications such as

catalysis, sensing, and bio-compatibility,<sup>1</sup> which can benefit from distinctive chemical and physical surface properties. Thus, careful design and control of surface properties is of great interest in materials and surface sciences. Self-assembled monolayers (SAMs), Langmuir-Blodgett films, and other surface-confined assemblies have long been acknowledged as a practical strategy for creating tailor-made functional surfaces. Ternary host-guest Langmuir monolayers with inherent inclusion cavities, affording hosts for non-amphiphilic guest molecules, can permit the introduction of various functionalities via the intercalation of guest molecules at air-water interface that otherwise may not be achievable. Unfortunately, these Langmuir-Blodgett films suffer from an inherent lack of stability due to their weak interactions with the solid surface.<sup>2</sup> SAMs are highly desirable for use in a wide range of applications due to the flexibility in design of their molecular structures and properties. For these reasons, SAMs have been widely used to prepare well-defined, stable structures and functional surfaces. The main disadvantage of the SAM method comes from the time-consuming and complex synthesis of the  $\alpha$ - $\omega$  molecules needed to form functionalized surfaces.

An alternative to  $\alpha$ - $\omega$  molecules for SAM formation is the use of surface host-guest assemblies. This approach can provide flexibility in tailoring interfaces and the potential ability to regenerate functional surfaces via intercalation of various functional guests. The method can also provide nanometer-scale precision via the well-controlled arrangement of organic molecules on surfaces over an extended length scale.<sup>3</sup> There are two general strategies available for the construction of surface host-guest assemblies. One is to use an ordered array of template molecules on a surface and then add functionality via specific host-guest interactions between template and a functional guest. The second is to use two-dimensional open structures with well-defined cavities as a template. Functional guest molecules can then be trapped in the repetitive and spatially ordered cavities on the surface. In both cases, host-guest interactions make it possible to add versatile functionalities to the surface with host-guest assembly.<sup>4,5,6,7</sup> Two-dimensional porous structures at a surface can be generated by means of several types of supra-molecular interactions: hydrogen bond-directed homo- and hetero-assembly of organic molecules, the coordination of metal centres to organic ligands, dipole-dipole interactions, van der Waals interactions, or a combination of

several interactions.<sup>8</sup>

In our work, three-dimensional low-density self-assembled monolayers (LDSAMs) with cavities are constructed on a targeted surface using host molecules with an integral spacer (anthracene-derivative) and a long alkane chain. At the liquid/solid interface, structurally homologous guest molecules with functional units can be intercalated into the cavities between hydrophobe arrays from solution under well-controlled external condition. In our previous work, we have investigated the structural features of anthracene-derived LDSAMs using several characterization methods under *ex situ* conditions. Herein, anthracene-derived thiol compounds with long alkane chains are synthesized as a host unit and LDSAMs are formed on gold surface. Quartz crystal microbalance with dissipation (QCM-D) measurements are used to demonstrate the capacity of LDSAMs to confine guest molecules in cavities and the structural changes of the host-guest assembly during guest intercalation from ethanol solution. X-ray photoelectron spectroscopy (XPS) measurements are then used to probe host-guest monolayers formed by immersing the host monolayer in solutions in a variety of other solvents. We believe that a distinct feature of solvent will affect to the intercalation process of guest molecules into the host-cavity by strengthening or weakening interactions between host molecule, guest molecule, and solvent. Hence polarity or dielectric features of solvents are considered to choose the solvents. Further, the chain length or ring size of solvents is concerned.

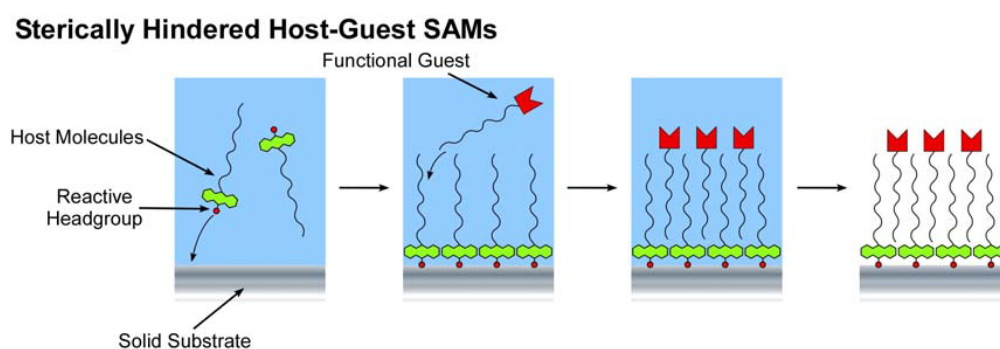


**Figure 5. 1.** Schematic illustration of host-guest assemblies for functional interfaces: Low-density SAMs provide well-ordered structures with nanometre-scale precision. Externally regulated host-guest interactions allow the versatile functionalization on surfaces via the intercalation of functional guests.

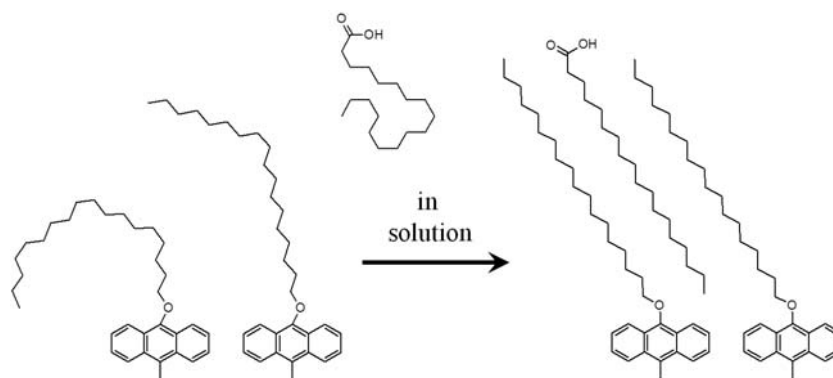


**Figure 5. 2.** Schematic illustration of non-covalently bonded host-guest assemblies via intercalation of stearic acid into host-cavities; interactions between host-guest, host-solvent, and guest-solvent are responsible for the formation of host-guest assemblies.

## 5.2. Experimental

### 5.2.1. Materials

10-bromoanthracene-9-boronic acid, 1-bromooctadecane, 1-octadecanol, copper (II) acetate, triethylamine, sodium ethanethiolate, stearic acid, and 2-naphthyl stearate were obtained from Aldrich. Octadecane was obtained from TCI America. Other common chemicals were obtained through various commercial sources. All reagents were used as received. Au substrates (1000 Å thick on silicon wafer) were purchased from Platypus Technologies (Fitchburg, WI). Au-coated quartz crystals ( $f = 5$  MHz,  $C = 17.7$  ng·cm<sup>-2</sup>·Hz<sup>-1</sup>) for QCM-D measurements were purchased from Q-Sense (Biolin Scientific Inc., Linthicum, MD).

### 5.2.2. Sample preparation

Au substrates were cut into 1'x 1' size. The pre-cut Au substrates were cleaned using 1:3 H<sub>2</sub>SO<sub>4</sub>:H<sub>2</sub>O<sub>2</sub> for 30 min following by extensive rinsing with deionized water (18.2 MΩ, Thermo Scientific Barnstead E-pure water purification system) and then kept dry under vacuum before use. In a similar way, gold-coated quartz crystals were cleaned using piranha solution for 10 min. Host-SAMs on Au surface were obtained by immersion of Au substrate in an ethanol solution of 10-octadecyl-9-anthracenethiol (10 mM) for 72 h at 50°C. The host-SAMs were then removed from the solution and sonicated in anhydrous ethanol then toluene for 10 min each and dried in nitrogen.

Host-guest assemblies were prepared by immersion of host-SAMs in 5 mM solutions of guest molecules in different solvents at room temperature: Benzene, cyclohexane, dibutyl ether, dichloromethane, diethyl ether, ethanol, heptane, toluene, and tetrahydrofuran were used as solvents and octadecane, 1-bromooctadecane, 1-octadecanol, octadecylamine, 2-naphthyl stearate, and stearic acid were used as guest molecules.

### 5.2.3. Characterization of host-guest assembly

All samples were characterized by FTIR/ATR and XPS. Fourier transform infrared (FTIR) spectra were acquired with a Varian 670-IR spectrophotometer with  $4\text{ cm}^{-1}$  resolution using attenuated total reflectance attachment. X-ray photoelectron spectroscopy (XPS) spectra were obtained using Perkin-Elmer PHI Quantera SXM-03 ESCA with a monochromatic Al K $\alpha$  X-ray source of 280 eV, located in the Nano-scale Characterization and Fabrication Laboratory (NCFL) at Virginia Tech. The source was run at 48.1 W and a take-off angle of  $45^\circ$  to the normal sample surface was used. High resolution spectra were obtained for C 1s region. The characterization of the kinetics of intercalation of guest molecules was performed using Q-Sense E1, quartz crystal microbalance with dissipation (Biolin Scientific, Inc., Linthicum, MD). Bare gold crystals were cleaned using 1:3 H<sub>2</sub>SO<sub>4</sub>:H<sub>2</sub>O<sub>2</sub> for 10 min following by extensive rinsing with deionized water (18.2 M $\Omega$ , Thermo Scientific Barnstead E-pure water purification system) and sonicated in anhydrous ethanol then toluene for 10 min each. Changes in frequency and dissipation associated with several overtone frequencies were measured during guest intercalation on host-SAMs-coated gold crystal. Experiments were performed at room temperature in solutions of stearic acid or 2-naphthyl stearate in ethanol. Each experiment began with flow-through of pure ethanol at 50ul/min to establish a reference zero baseline. The pump was stopped in order to switch from pure ethanol to a guest solution. The guest solution was then pumped through the module and changes in the frequency and dissipation were measured over time. Three equal experiments were performed to confirm reproducibility of the data. Host-SAMs coated gold crystal used once was soaked in pure ethanol in order to remove residual guest molecules for 24 hrs and sonicated in pure ethanol then toluene for 1 hrs each. Host-SAMs coated gold crystal was discarded after using it three times.

### 5.2.4. Synthesis

**Synthesis of 10-(octadecyloxy)-9-anthracenethiol** 10-(octadecyloxy)-9-anthracenethiol was synthesized from 10-bromoanthracene-9-boronic acid via a two-step reaction: The O-

arylation of an aliphatic alcohol<sup>9</sup> and the thiolation of the inactivated aryl halide<sup>10</sup>. First, a slurry of 1-octadecanol (0.5 g, 1.85 mmol), arylboronic acid (1.12 g, 3.7 mmol), anhydrous  $\text{Cu}(\text{OAc})_2$  (0.68 g, 3.7 mmol), and triethylamine (1.13 g, 11.2 mmol) in dichloromethane (10 ml) was stirred at room temperature with air flow for 96 h. The organic product, 10-bromo-9-anthryl octadecyl ether, was extracted with anhydrous toluene and then isolated in methanol. Second, 10-bromo-9-anthryl octadecyl ether (1 g, 1.9 mmol) obtained from the first reaction, sodium ethanethiolate (1.28 g, 15.2 mmol), and DMF (20 ml) was refluxed at 150°C then overnight under nitrogen. Once the reaction was cooled and DMF was removed under vacuum, hydrochloric acid (40 ml, 0.2 M) was added under vigorous stirring. The organic product was extracted with dichloromethane or diethyl ether, rinsed three times with distilled water, and dried over anhydrous sodium sulfate.

### 5. 3. Results and Discussion

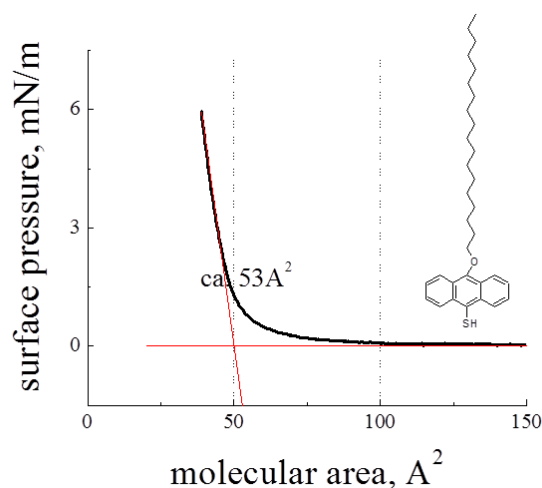


**Figure 5. 3.** Surface pressure ( $\pi$ ) - molecular area ( $A$ ) isotherm for the compression of host molecules at air-aqueous interface. Mean area per molecule (extrapolated to zero pressure) is obtained using 10-octadecyl-9-anthracenethiol solution of 0.1 mg/ml

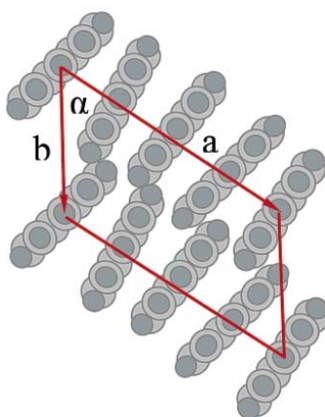


**Figure 5. 4.** Schematic drawing of the model proposed for the ordered structure of 9-mercaptoanthracene (MA) on Au(111), where  $a$ ,  $b$ , and  $\alpha$  are approximately 22.5 Å, 12.7 Å, and 51°, respectively. \* This image was copied from reference 9.

**$\Pi$ -A isotherm of 10-octadecyl-9-anthracenethiol:** To understand the formation of host-guest assemblies via intercalation of guest molecules, it is important to know the molecular arrangement of the host self-assembled monolayer of large, rigid aromatic thiols. Intensive

studies using scanning tunneling microscopy (STM) have been reported on the molecular arrangement of anthracene-derived SAMs that are similar to our anthracene-derived host-SAMs and show that SAMs have a structure with four molecules in a unit cell of ca.  $222 \text{ \AA}^2$ , leading to an area per molecule of ca.  $55\text{-}60 \text{ \AA}^2$ .<sup>11</sup> A Langmuir isotherm of 10-octadecyl-9-anthracenethiol at the air-aqueous interface is shown in Figure 5.3, indicates an extrapolated area of  $S = 53 \text{ \AA}^2$ , which is close to the van der Waals area of a single standing-up anthryl group ( $\sim 52 \text{ \AA}^2$ ). Based on these results, and a cross-sectional area of ca.  $21 \text{ \AA}^2$  for a vertically oriented alkane chain, we estimated a cavity size of ca.  $34\text{-}39 \text{ \AA}^2$ , in our anthracene based LDSAMs. Thus, it should be possible for each cavity to accommodate up to alkane functionalized guest molecules.

### 5.3.1. Examination of the host-guest assembly by QCM

**Stearic acid-intercalated host-guest assemblies:** QCM-D measurements were used to study the intercalation of guest molecules into host-monolayers coated on a gold crystal. Here we focus on the effect of intercalated guest molecules on the adsorption-induced dissipation shift and frequency shift. Figure 5.5 summarizes the results of QCM measurements for the intercalation of stearic acid from an ethanol solution. Figure 5.5a and 5.5b show  $\Delta f$  and  $\Delta D$  as a function of time during the adsorption of stearic acid on a bare gold crystal and a host-coated crystal. The QCM data demonstrates that stearic acid is adsorbed on both substrates. The addition of a stearic acid solution of 25 mM in ethanol causes a sudden drop in frequency followed by a slower decrease until the system saturates. Upon exchange of stearic acid for pure ethanol the frequency reverts to the baseline. In the same manner, the dissipation increases with time during the initial adsorption phase, i.e., more energy is dissipated as stearic acid is adsorbed, and then saturates at  $\Delta D_{\text{avg}} = 2.5 \times 10^{-6}$ . Upon rinsing with pure ethanol the dissipation reverts to the baseline. It is important to note that both  $\Delta f$  and  $\Delta D$  return to the baseline upon rinsing since this phenomenon indicates that the adsorption of stearic acid on the bare gold and host-coated surface is reversible over the time-scale studied.

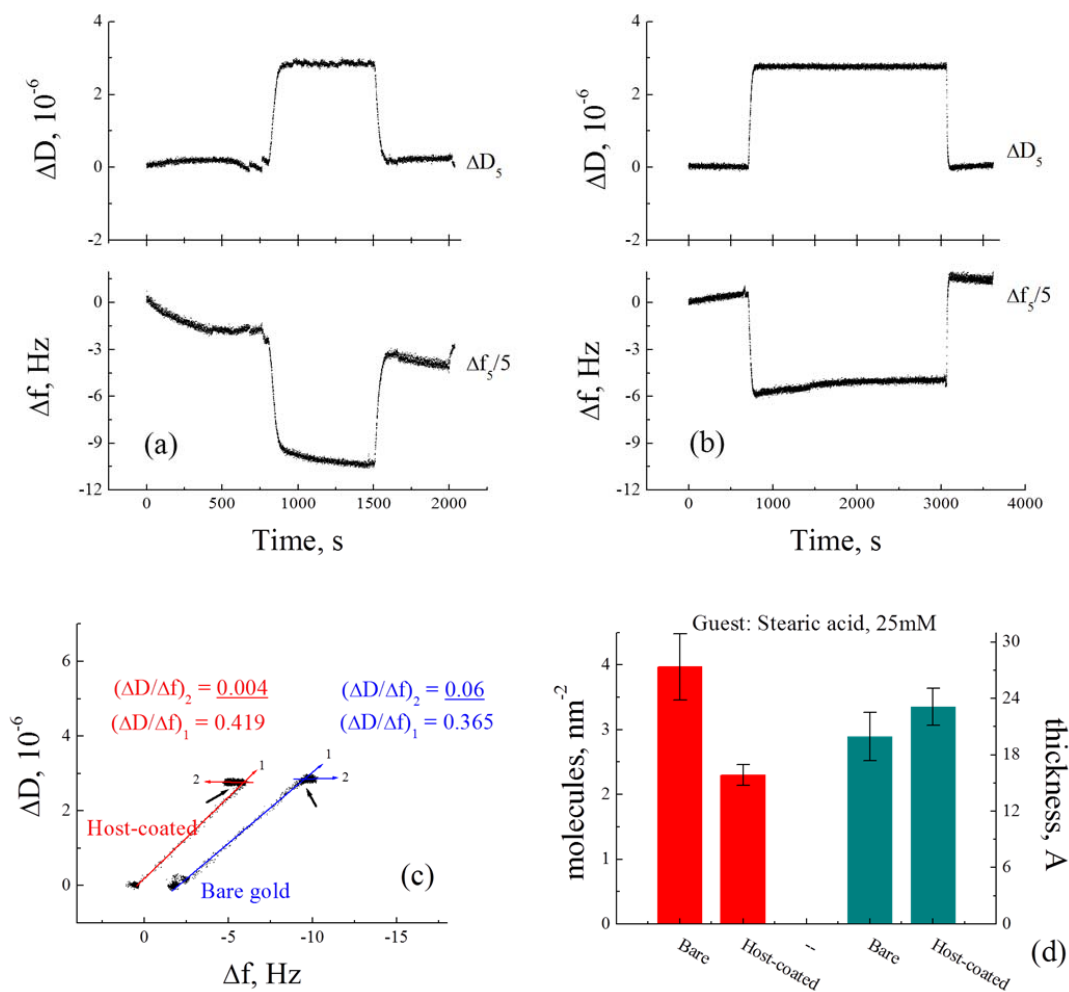


**Figure 5. 5.** Frequency shift (fifth overtone -  $\Delta f_5/5$ ) and dissipation shift  $\Delta D_5$  ( $10^{-6}$ ) vs time a bare gold crystal (a) and a host-coated crystal (b) exposed to a 25 mM solution of stearic acid in ethanol. (c) Dissipation-Frequency (D-f) plots based on the data of  $\Delta f_5/5$  and  $\Delta D_5$ . Black arrows indicate break points where the slope changes. After the break point, the direction of **arrow 2** for the host-coated sample indicates that there is a loss of mass from host-guest assembly. The shallow slope indicates that the host-guest assembly is rigid. (d) The number of adsorbed guest molecules per area and the calculated thickness of the adsorbed films (further details are given in Table 5.1)

A dissipation-frequency (D-f) plot eliminates time as an explicit parameter and reveals how much the dissipation depends on a unit frequency change by looking at the slope at any point on the curve.<sup>12</sup> Thus, combined frequency and dissipation measurements provide information about the structural properties of host-guest assemblies during the adsorption

process. The D-f plot in Figure 5.5c is based on  $\Delta D_5$  vs  $\Delta f_5/5$  and indicates that there exist two different adsorption processes for both bare gold and host-coated surfaces. (**Arrow 1** begins at the start of the process and points towards the break point. Similarly, **arrow 2** begins at the break point and points towards the end of the process) The phase changes of the adsorption processes manifest different slopes of  $\partial D/\partial f$ , with a break point at  $\Delta f_{\text{bare}} \cong -9$  Hz and  $\Delta f_{\text{host}} \cong -6$  Hz, respectively. The initial  $\partial D/\partial f$  slopes at low surface coverage are quite large as  $(\partial D/\partial f)_{1,\text{bare}} = 0.365(\times 10^{-6} \text{ Hz}^{-1})$  and  $(\partial D/\partial f)_{1,\text{host}} = 0.419(\times 10^{-6} \text{ Hz}^{-1})$ , whereas after the break point (at high surface coverage) the slopes substantially decrease to  $(\partial D/\partial f)_{2,\text{bare}} = 0.06$  and  $(\partial D/\partial f)_{2,\text{host}} = 0.004$ , respectively due to stabilization of the monolayer (high rigidity). In this regime the Sauerbrey equation (Eq. 1) is valid:

$$\Delta m = -C \cdot \Delta f_n/n \quad (1)$$

where  $C$  is a constant that depends on the physical properties of the crystal ( $C = 17.7 \text{ ng} \cdot \text{cm}^{-2} \cdot \text{Hz}^{-1}$ ) and  $n$  is the overtone number. Hence, a decrease in frequency correlates to an increase in mass attached to the surface. The surface coverage of the adsorbed guest,  $\Gamma$  ( $\text{mol} \cdot \text{cm}^{-2}$ ) can then be calculated using Eq. 2.

$$\Gamma = \Delta m/\text{m.w.} \quad (2)$$

where **m.w.** is the molar mass of the guest molecules. As mentioned above, it is interesting to note that the plots show no differences between adsorption behavior on bare gold and the host-coated surface. These observations suggest that there are favorable interactions between stearic acid and the pure gold substrate, and thus a self-assembled monolayer of stearic acid was formed.

**Table 5. 1.** Parameters for stearic acid calculated using the Sauerbrey equation for (a) bare gold and (b) host-coated surface: the adsorbed mass per unit area ( $\text{cm}^2$ ), the number of molecule per unit area ( $\text{nm}^2$ ), and the thickness ( $\text{\AA}$ ) of the monolayer. \*The estimated cavity area is approximately  $0.34\text{-}0.39 \text{ nm}^2$ .

(a)	$f_s/5$	(b)	$f_s/5$
ng/cm <sup>2</sup>	187.44	ng/cm <sup>2</sup>	108.70
molecule/nm <sup>2</sup>	3.97	molecule/nm <sup>2</sup>	2.30
thickness, $\text{\AA}$	19.92	thickness, $\text{\AA}$	23.11
		mole/cavity	0.9

The adsorbed mass per unit area ( $\text{cm}^2$ ), the number of molecule per unit area ( $\text{nm}^2$ ), and the layer thickness ( $\text{\AA}$ ), are listed in Table 5.1 (all parameters calculated using the Sauerbrey equation). At full surface coverage, QCM-D measurement for the host-coated surface shows a frequency shift of  $\Delta f_{\text{host}} = -5.1 \text{ Hz}$  that corresponds to the coverage of  $\Gamma_{\text{host}} = 3.16 \times 10^{-10} \text{ mol}\cdot\text{cm}^{-2}$ , which is smaller than that for the bare gold crystal ( $\Gamma_{\text{bare}} = 5.80 \times 10^{-10} \text{ mol}\cdot\text{cm}^{-2}$ ). The molecular area for stearic acid adsorbed on a bare gold crystal ( $A_{\text{bare}}$ ) and the host-coated crystal ( $A_{\text{host}}$ ) are assessed using data in Table 5.1;  $A_{\text{bare}}$  is  $25.2 \text{ \AA}^2/\text{molecule}$  and  $A_{\text{host}}$  is  $43.5 \text{ \AA}^2/\text{molecule}$ .  $A_{\text{bare}}$  of  $25.2 \text{ \AA}^2/\text{molecule}$  is larger than expected molecular area ( $22 \text{ \AA}^2$ ) for closely-packed monolayer of stearic acid at air-water interface, which indicates a slightly expanded state of the monolayer.<sup>13,14,15</sup> On the other hand,  $A_{\text{host}}$  of  $43.5 \text{ \AA}^2/\text{molecule}$  is significantly larger than the expected area per molecule ( $22 \text{ \AA}^2$ ).

Considering the molecular arrangement of host-SAMs, the value of  $A_{\text{host}}$  of  $43.5 \text{ \AA}^2/\text{molecule}$  is an apparent molecular area of the intercalated molecule. This also suggests that the stearic acid is added to the host monolayer in a 1:1 ratio with the host molecules, as  $43.5 \text{ \AA}^2$  corresponds to the expected value of  $53\text{-}60 \text{ \AA}^2$  for anthracene molecules at a surface, as shown in Figure 5.6. This suggestion is supported by an estimation of the layer thickness for the stearic acid-intercalated host-guest assembly. The layer thickness was estimated for both a bare gold crystal and a host-coated crystal:  $t_{\text{bare}}$  is  $19.92 \text{ \AA}$  and its alkyl chain tilt is

53.2° from the normal to the surface, while  $t_{\text{host}}$  is 23.11 Å with a chain tilt of 45.9°. The more vertical orientation of the host-coated crystal suggests that stearic acid is intercalated in the host SAMs. The molecular number of 2.3 molecules/nm<sup>2</sup> corresponds to ca. 0.9 molecules/cavity.

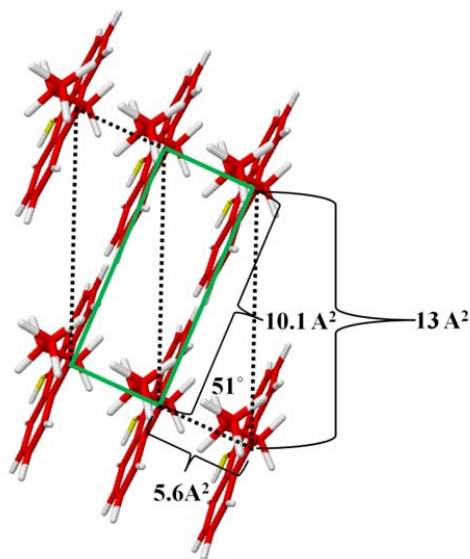


**Figure 5. 6.** Schematic drawing of the ordered structure of OAT host-SAMs on Au(111). Considering the cross-sectional area of alkane chain (21 Å<sup>2</sup>), one host molecule in a unit cell is 34-39 Å<sup>2</sup> in area

**Naphthyl stearate-intercalated host-guest assemblies:** Figure 5.7 summarizes the main results of QCM measurements for intercalation of a naphthyl stearate guest molecule from an ethanol solution. All calculated parameters are listed in Table 5.2. In general, the behavior of  $\Delta f$ ,  $\Delta D$ , and the D-f plot for intercalation of naphthyl stearate into the host monolayer are similar to those for stearic acid. However, there are no significant changes in frequency and dissipation for the bare gold substrate, which suggests that naphthyl stearate molecules cannot form a self-assembled monolayer on bare gold. The coverage of naphthyl stearate is only  $\Gamma_{\text{bare}} = 1.20 \times 10^{-10}$  mol·cm<sup>-2</sup> at the end of adsorption process compared to  $\Gamma_{\text{host}} = 6.24 \times 10^{-10}$  mol·cm<sup>-2</sup>. The molecular area of naphthyl stearate is calculated to be 23.5 Å<sup>2</sup>/molecule, which is similar to the van der Waals area of the naphthyl moiety(24

$\text{\AA}^2/\text{molecule}$ ).<sup>16</sup> This indicates that at least one molecule of naphthyl stearate can fit into each host cavity.

The D-f plot for a host-coated surface also shows two different adsorption processes as in the case of stearic acid (Figure 5.7c). After the break point at  $\Delta f_{\text{host}} \cong -15$  Hz the sign of  $\partial D/\partial f$  turns to the negative, such that  $(\partial D/\partial f)_{1,\text{host}} = 0.402(\times 10^{-6} \text{ Hz}^{-1})$  during first adsorption phase and  $(\partial D/\partial f)_{2,\text{host}} = -0.270(\times 10^{-6} \text{ Hz}^{-1})$  during the second adsorption phase, which indicates that the total energy dissipation decreases as the added mass increases by allowing more and more close packing of naphthyl stearate within the host cavity and thus, the monolayer is highly rigid. As mentioned earlier, the molecular number of 4.26 molecules/ $\text{nm}^2$  gives a value of 1.66 molecules/**cavity**. The validity of this molecular number is supported by both the sign inversion of  $\partial D/\partial f$  and the increased layer thickness during the second adsorption phase, illustrating the formation of densely-packed host-guest assemblies.

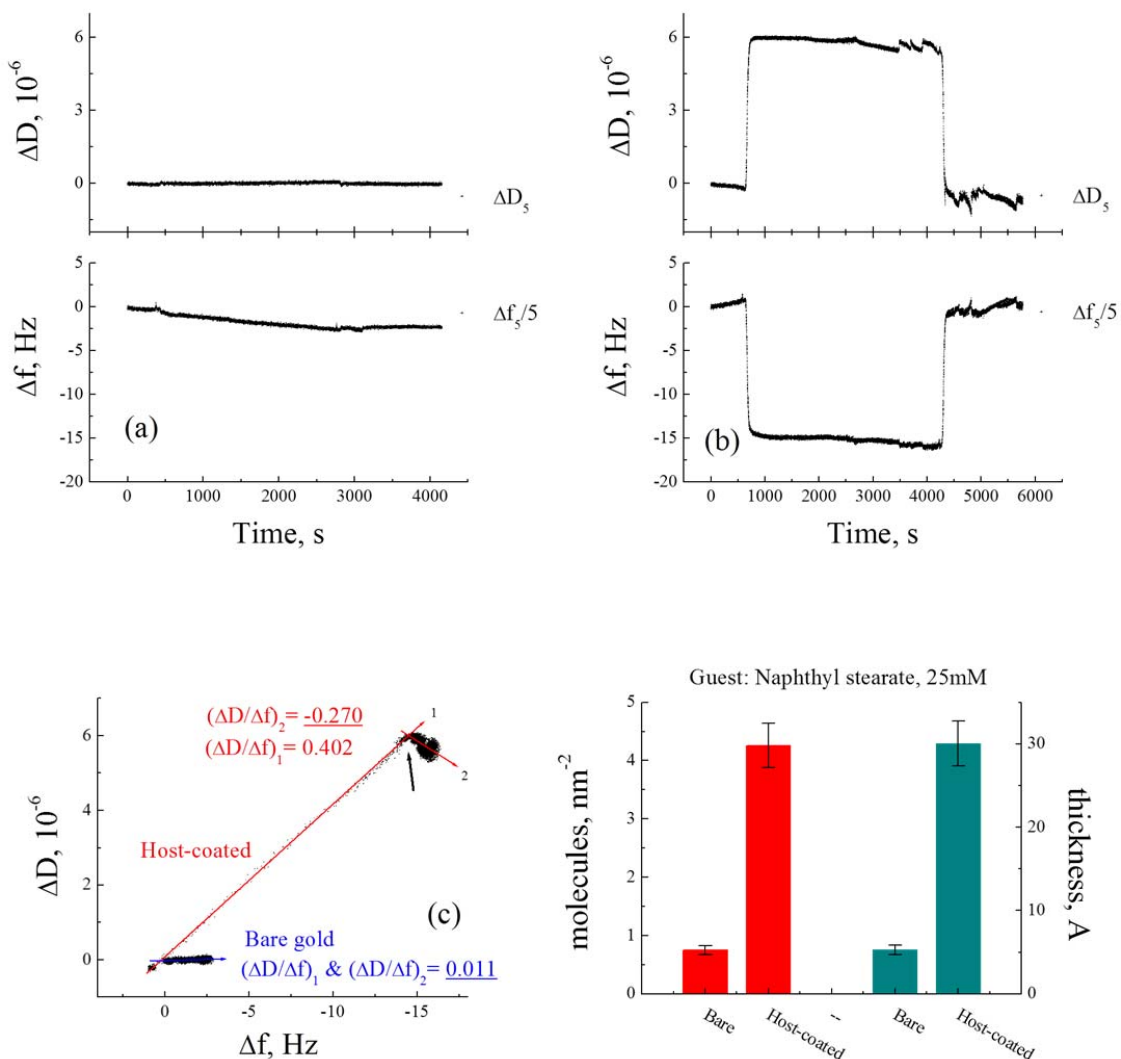


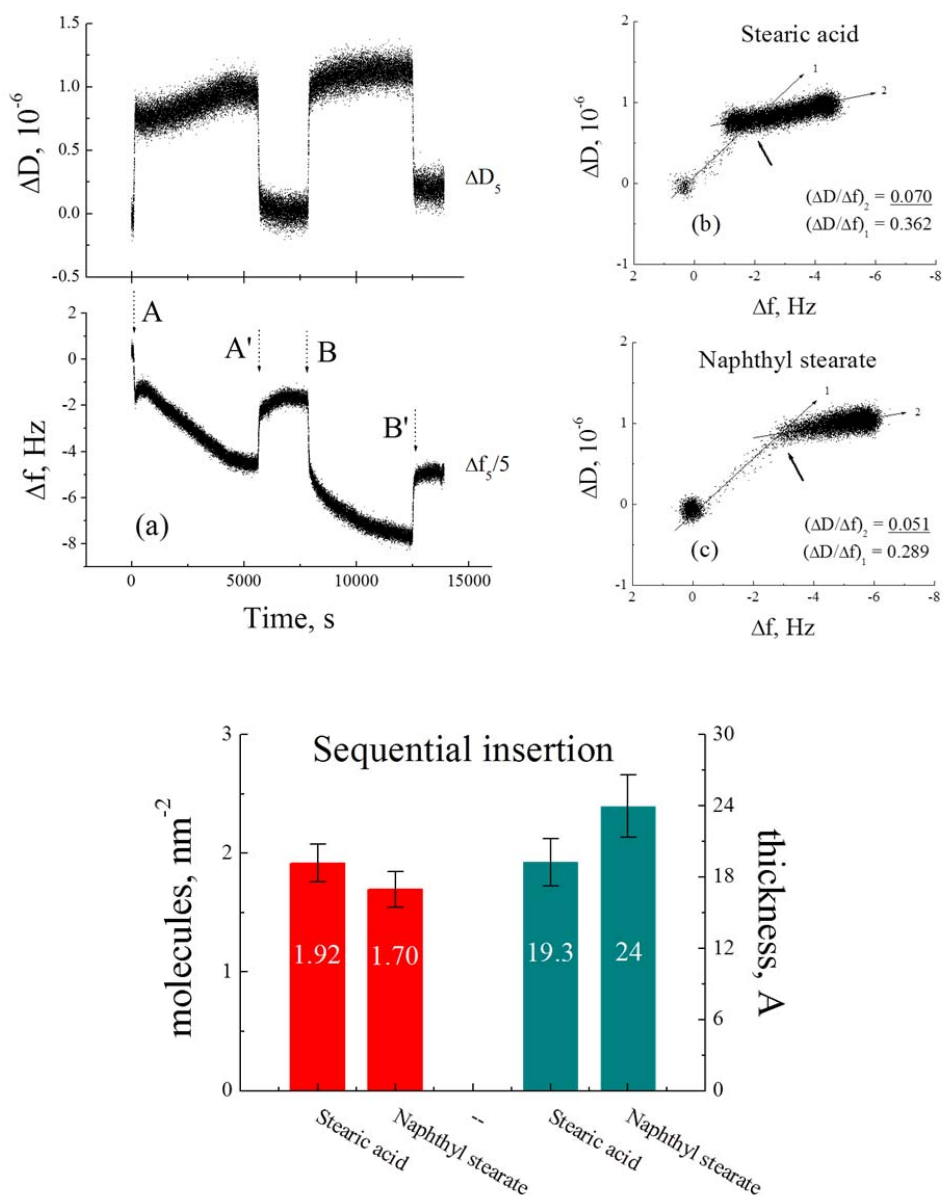
**Figure 5. 7.** Frequency shift (fifth overtone -  $\Delta f_5/5$ ) and dissipation shift ( $\Delta D_5$ ) vs time for a bare gold crystal (a) and a host-coated crystal (b) exposed to a 25 mM solution of naphthyl stearate in ethanol. (c) Dissipation-Frequency (D-F) plots based on the data of  $\Delta f_5/5$  and  $\Delta D_5$ . The arrows indicate break points where the slope changes. The direction of **arrow 2** suggests an increase in mass with a corresponding increase in rigidity, i.e., less dissipation per added molecule during the second adsorption phase. (d) The number of adsorbed guest molecules per area and the calculated thickness of the adsorbed films (further details are given in Table 5.2)

**Table 5. 2.** Parameters for naphthyl stearate calculated using the Sauerbrey equation for (a) bare gold and (b) host-coated surface: the adsorbed mass per unit area ( $\text{cm}^2$ ), the number of molecule per unit area ( $\text{nm}^2$ ), and the layer thickness ( $\text{\AA}$ ). \* The estimated cavity area is approximately  $0.34\text{-}0.39 \text{ nm}^2$ .

(a)	$f_s/5$	(b)	$f_s/5$
ng/cm <sup>2</sup>	51.06	ng/cm <sup>2</sup>	290.24
mole/nm <sup>2</sup>	0.75	mole/nm <sup>2</sup>	4.26
thickness, $\text{\AA}$	5.29	thickness, $\text{\AA}$	30.05
		mole/cavity	1.66

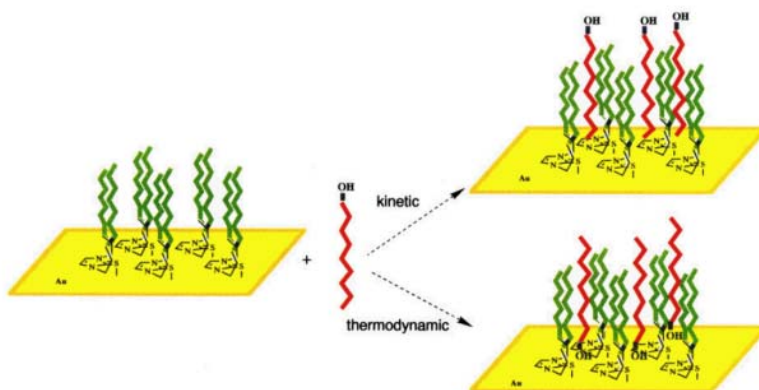
**Sequential insertion of guest molecules into a host-coated surface:** In order to demonstrate the reversibility of the process, we performed experiments on the insertion, removal and exchange of two different guests. Two different guest solutions of 3 mM in ethanol were used: first, a host-coated surface was immersed in a stearic acid solution (A), the stearic acid solution was then replaced with pure ethanol (A'), then the ethanol was replaced by a naphthyl stearate solution (B), and finally this was replaced by pure ethanol (B'). From this experiment we expect that the number of adsorbed molecules will be equal for both stearic acid and naphthyl stearate as the number of host cavities is limited on the surface. Figure 5.8 summarizes the results for the guest exchange experiment. All characteristic parameters are summarized in Table 5.3. First, as shown in Figure 5.8b and 5.8c, the D-f plots indicate that the  $\partial D/\partial f$  values at the end of adsorption process are quite low, indicating that the host-guest assemblies are highly rigid and thus the Sauerbrey equation is valid in this regime. Figure 5.8a presents the frequency shift with time during the adsorption of stearic acid (A) followed by naphthyl stearate (B) on the same host-coated surface. It is particularly interesting to note that after the switch from a guest solution to pure ethanol (A' and B' in Figure 5.8a) the frequency shift does not revert to the baseline, indicating that parts of the host cavities are still occupied by guest molecules. This behavior is attributed to the change of the orientation of carboxylic end of stearic acid, as depicted in

Figure 5.9. Ward et al reported that guest molecules have a favored intercalation process over time depending on inter-chain interactions or guest-substrate interactions. Thus the carboxylic end of stearic acid prefers to interact with the base of the cavities where it can participate in stronger interactions with the host SAM.<sup>17</sup>



**Figure 5. 8.** (a) Frequency shift (fifth overtone -  $\Delta f_5/5$ ) and dissipation shift ( $\Delta D_5$ ) as a function of time for the adsorption of stearic acid (A) followed by naphthyl stearate (B) on host-coated surface. The Dissipation-frequency (D-f) plot for (b) stearic acid and (c) naphthyl stearate. (d) The number of adsorbed guest molecules per area and the calculated

thickness of the adsorbed films (further details are given in Table 5.3)



**Figure 5. 9.** Kinetically favored intercalation of the prefluoroalkyl end of the alcohols results in a hydrophilic surface substituted with hydroxyl group at early time of the adsorption process. At longer times, thermodynamically preferred intercalation of the alcohol end results in a perfluoroalkane interface. \* This image was copied from reference **15**.

The surface coverage is estimated to be  $\Gamma_{st} = 3.29 \times 10^{-10} \text{ mol} \cdot \text{cm}^{-2}$  and  $\Gamma_{na} = 2.52 \times 10^{-10} \text{ mol} \cdot \text{cm}^{-2}$  for stearic acid and naphthyl stearate respectively. The number of molecules per unit area ( $\text{nm}^2$ ) and the layer thickness for the host-guest assemblies are presented in Figure 5.8d. The host cavities accommodate 0.75 molecules for stearic acid and 0.66 molecules for naphthyl stearate at the end of the adsorption processes.

**Table 5. 3.** Parameters for naphthyl stearate calculated using the Sauerbrey equation for (a) bare gold and (b) host-coated surface: the adsorbed mass per unit area ( $\text{cm}^2$ ), the number of molecule per unit area ( $\text{nm}^2$ ), and the layer thickness ( $\text{\AA}$ ). \* The estimated cavity area is approximately  $0.63 \text{ nm}^2$ .

(a)	$f_s/5$	(b)	$f_s/5$
$\text{ng/cm}^2$	90.56	$\text{ng/cm}^2$	115.71
$\text{mole/nm}^2$	1.92	$\text{mole/nm}^2$	1.70
thickness, $\text{\AA}$	19.25	thickness, $\text{\AA}$	23.96
mole/cavity	0.75	mole/cavity	0.66

In summary, the QCM-D experiments using stearic acid and naphthyl stearate in ethanol result in the following conclusions: (i) guest molecules are intercalated into the host cavities, (ii) rigid host-guest assemblies are formed via close-packing of guest molecules at the end of adsorption phase, (iii) thus the Sauerbrey equation is valid in this regime, (iv) guest molecules can be replaced by different guest molecules in a stepwise fashion (guest removal followed by guest insertion).

### 5.3.2. Examination of the host-guest assembly by XPS

**XPS analysis for multi-component host-guest assemblies:** *in-situ* QCM experiments were limited to a few guests in ethanol solution in order to prevent damage to the instrument. A study of a large range of solvents and guests was performed *ex-situ* using XPS. XPS spectral analysis allows a comparison between the spectra of the host-SAMs and the host-guest assemblies. The presence of functional groups and unbound alkyl chains in the host-guest assemblies as compared to the host monolayers provide insight into the intercalation of guest molecules into the host cavities under various conditions. The survey spectra of a blank Au surface, a host-SAM, and a host-guest assembly (stearic acid) are depicted in Figure 5.10. Characterization of the host-SAMs and the host-guest assemblies by XPS confirms that the monolayer structure formed on the gold surface reflects elements of the intended adsorbate:

gold (Au 4f, 4d, 4p), carbon (C 1s), sulfur (S 2p), and oxygen (O 1s, Auger KLL). After the formation of host-SAMs and host-guest assemblies, the relative intensities of the C1s and O1s lines increase simultaneously with a decrease of intensity in the Au 4f and 4d lines. Spectra for all of the samples studied are included in the supporting information.

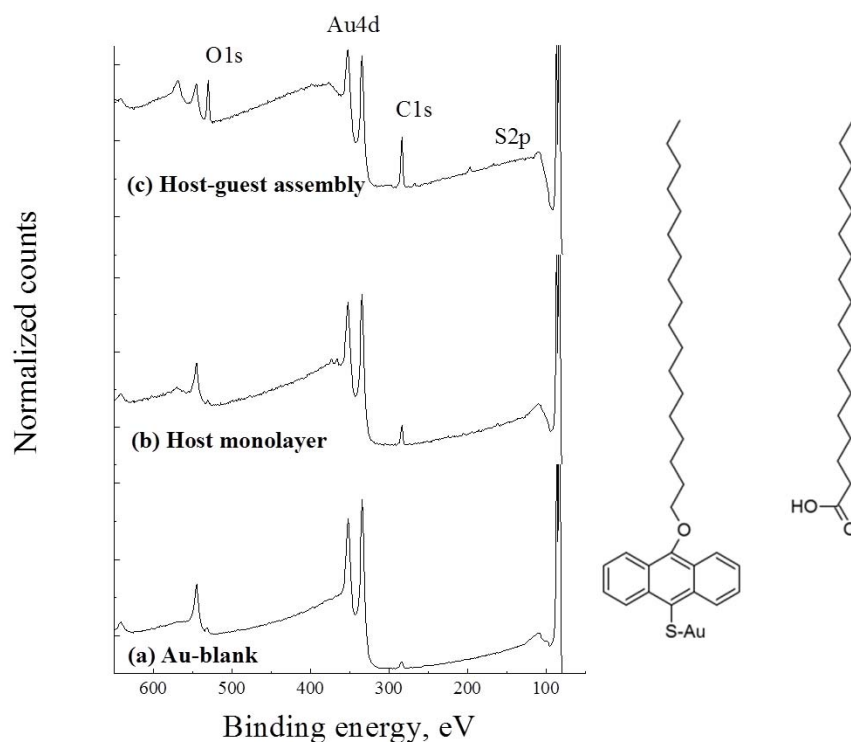


**Figure 5. 10.** XPS spectra of (a) blank Au (bottom), (b) host monolayer (middle), and (c) host-guest (stearic acid) assembly (top). The host monolayer and host-guest assembly show sulfur signals in the region of 160 to 170 eV. The reference Au shows no sulfur peak in this region. Note that the molecular structures of host and guest are depicted, respectively.

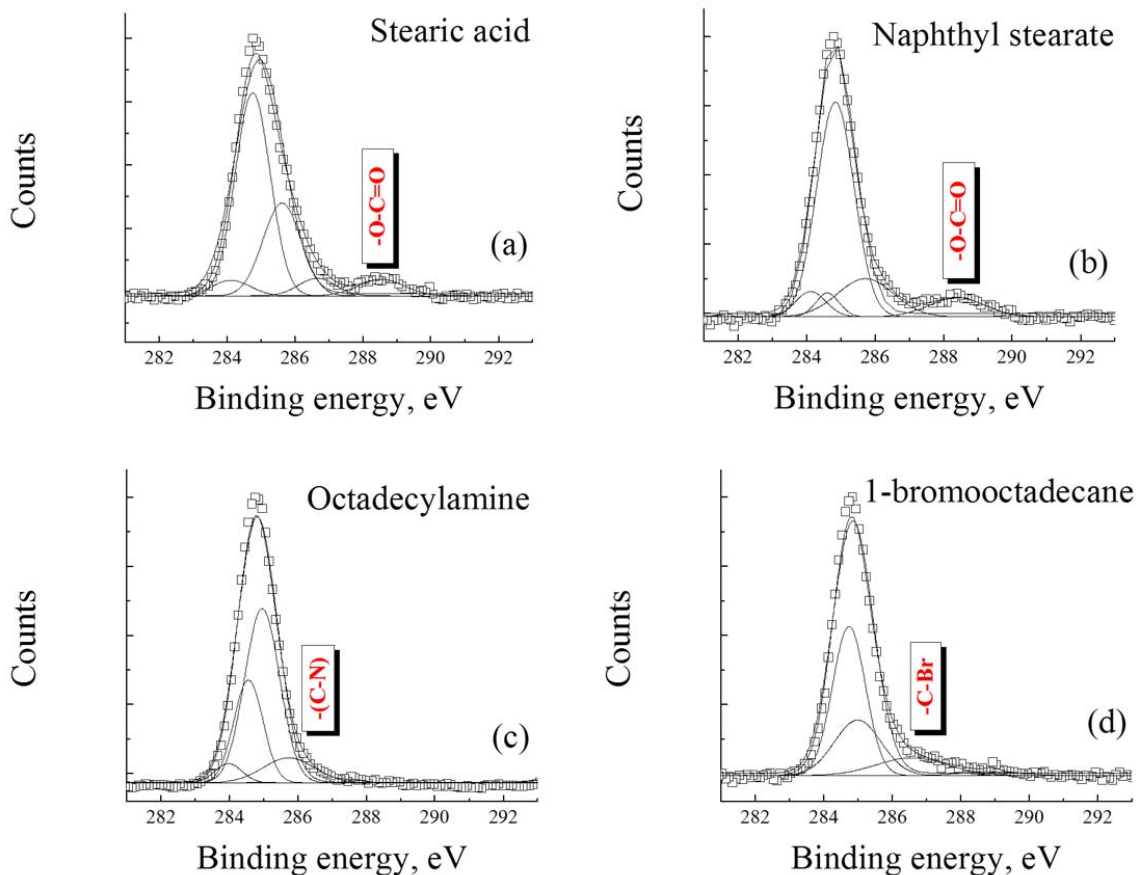


**Figure 5. 11.** High resolution C 1s spectra for host-guest assemblies prepared in the guest solution of (a) stearic acid, (b) 2-naphthyl stearate, (c) 1-octadecylamine, and (d) 1-bromooctadecane in benzene, respectively.

Figure 5.11 shows the high resolution C 1s spectra for host-guest assemblies, which were prepared by immersion of host-coated gold substrates in different guest solutions in benzene for 12 hrs followed by sonication in benzene for 30 min. Curve fitting analysis was carried out using individual peaks of Gaussian line shape. If necessary, new peaks were added to obtain an optimal fit. The standard deviations included are at a 95% confidence level. The line through the data points displays the best fit obtained from the overlapping of the Gaussian peaks. As shown in Figure 5.11, each host-guest assembly has a distinct peak at 288.7 (O-C=O), 285.8 (C-N), and 286.9 eV (C-Br) respectively, corresponding to the functional moiety of each guest molecule. This suggests the presence of the desired guest

molecules in each host-guest assemblies.

High resolution spectra of the C 1s peak of a host-SAM and a stearic acid host-guest assembly are shown in Figure 5.12. The spectrum of the blank Au substrate is also shown for comparison. The position and shape of the C 1s peak measured under the same experimental conditions are different for blank Au, the host monolayer, and a host-guest assembly. The main C 1s peak for a carbon contaminated Au substrate shows a binding energy of 284.8 eV with FWHM of 1.22 eV and a higher binding energy tail which can be attributed to the presence of C-O and -O-C=O bonds at about 286.5 eV and 289.9 eV, respectively. The spectrum of the host monolayer shows a binding energy of 284.9 eV for C-C sp<sup>3</sup> and 284.4 eV for C-C sp<sup>2</sup>, indicating the presence of both aliphatic and aromatic species. In contrast, the spectrum of the host-guest assembly with stearic acid shows two different binding energy states for C-C sp<sup>3</sup>: a lower binding energy state at 284.7 eV with FWHM of 0.94 eV and a higher binding energy state at 285.6 eV with FWHM of 1.1 eV, as well as C-C sp<sup>2</sup> peak at 283.9 eV, C-O peak at 286.7 eV, and -O-C=O peak at 288.5 eV. These lower and higher binding energy states are due to two different carbon species on the surface. We attribute the lower binding energy state to the host monolayer which is chemically bonded to the surface; the higher binding energy component is attributed to the chemically non-bonded, intercalated stearic acid present in the host-guest assemblies.<sup>18,19</sup>

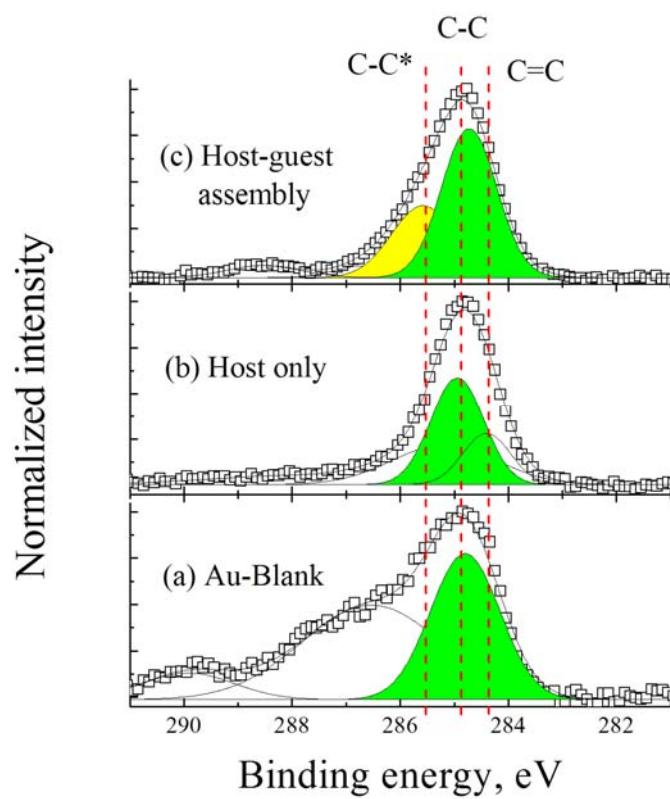


**Figure 5. 12.** High resolution C 1s XPS spectra for (a) blank Au, (b) host SAM, and (c) host-guest assembly with stearic acid on gold surface. The experimental spectra are shown together with curve fittings (solid lines). The vertical lines (red) indicate the position of C=C, C-C, and C-C\*, respectively. Note that unbound C-C peaks are observed around 285.6 eV.

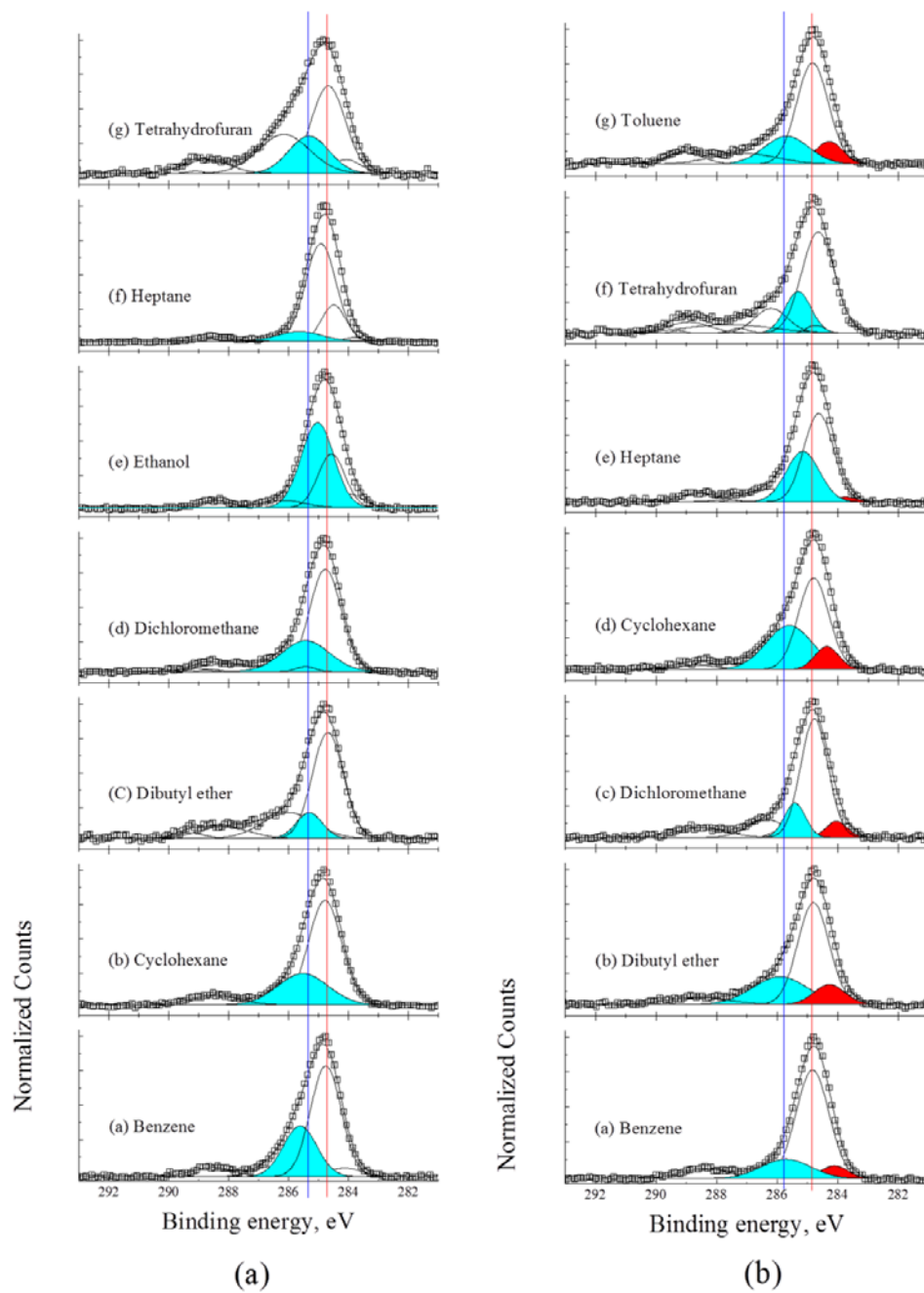


**Figure 5. 13.** High resolution XPS spectra for C 1s for host-guest assembly with (a) stearic acid or (b) naphthyl stearate each. Host-SAMs were immersed in stearic acid solution in various solvent for 12 hrs. Solid lines indicate deconvoluted peaks for each component. Two vertical lines correspond to the position of C-C\* (blue, 285.4 eV) and C-C (red, 284.7 eV), respectively. Red-colored regions in (b) indicates the intensity of C=C (284 eV).

Based on the analysis of the high resolution XPS spectra above, the coverage of unbound alkyl chain (C-C\*) within the host-guest assembly is determined by the ratio of C-C\* peak area to total peak area under the C 1s peak. High resolution C 1s spectra with deconvoluted peaks for host-guest assemblies with stearic acid or naphthyl stearate are shown in Figure 5.13. The average peak locations, their assignments, and the corresponding percentages for unbound C-C\* for stearic acid are shown in Table 5.4. In addition, the layer thickness of the guest-intercalated host-SAMs is shown in Table 5.4 to compare with unbound C-C\* ratio. The thickness of the overlayer is calculated from the C 1s to Au 4f intensity. The ratios are given by:

$$I_{C1s}/I_{Au4f} = k_{Au}(1 - e^{-d_c/\lambda_c})/(e^{-d_c/\lambda_{Au}})$$

where  $d_c$  is the thickness of the carbon layer,  $\lambda_c$  (= 30 Å) is the length of the mean free path (MEP) of the C 1s photoelectrons through the carbon layer and  $\lambda_{Au}$  (= 36.5 Å) is the MEP of the Au photoelectrons through the Au.  $k_{Au}$  is a specific constant.<sup>20</sup>

The main results are summarized in Figure 5.14. Figure 5.14a shows the ratio of unbound C-C\* (stearic acid) adsorbed into host monolayers. No C-C\* peak was observed in the XPS data for the guest-free host-monolayer. The presence of unbound C-C\* bonds suggests the intercalation of stearic acid. This is supported by an estimation of the layer thicknesses of the host-guest assemblies with stearic acid. It is noteworthy that dependence of the ratio of C-C\*/total peak area on solvents type tracks well with the dependence of the overlayer thickness in the ethanol and heptane based stearic acid host-guest assemblies. The large C-C\*/total peak area ratio and layer thickness in the ethanol and heptane based stearic acid host-guest assemblies is attributed to the formation of a multilayer structure on the top of host-monolayer during adsorption. The agreement between C-C\*/total peak area ratio and layer thickness is also observed in the case of naphthyl stearate as shown in Figure 5.14b. It is important to note that the C-C  $sp^2$  (C=C) intensity increases considerably due to the presence of naphthyl moiety. Also, the effect of solvent is not as apparent for the naphthyl stearate guest.

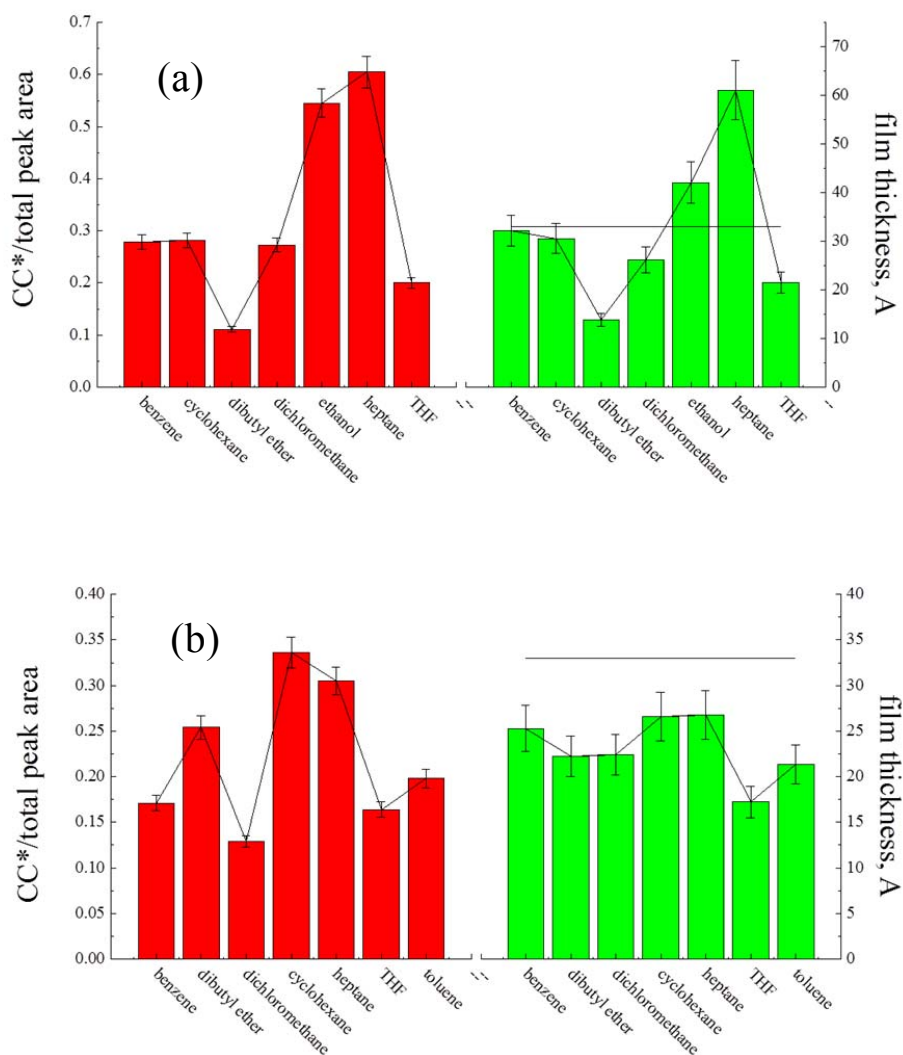


**Figure 5. 14.** The ratio of the C-C\* (alkyl tail of host-guest assembly) to total peak area and calculated thickness for host-guest assemblies with (a) stearic acid and (b) naphthyl stearate in various solvents derived from XPS data. Red horizontal lines are the expected layer thickness for standing-up host monolayer.

The lack of a significant dependence on solvent type could be due to the fact that the samples for XPS measurements were immersed in guest solution (10 mM) over a long period of time (12 hrs). This is significantly longer than the time periods used for QCM measurements, and it is likely that there would be observed differences over short time scales.

Especially this is based on observed differences in contact angle of water depending on the time period of immersion. We expect that there should be interplay between the interactions guest and solvent as well as the host and solvent for guest-intercalation into the host cavity. For example, as solvent becomes more polar, the driving force for transfer of the alkyl tails (hydrophobic) of amphiphiles into the host-cavity via desolvation would be greater.

**Table 5. 4.** Characteristic XPS binding energies and relative area of C-C\* and C-C for the host-guest assemblies with stearic acid and naphthyl stearate at various solvents, and the proposed CC\*/CC ratios. The peak area ratio of the host-guest assemblies to the host monolayer is also listed. The thickness of host-guest assemblies is estimated from the C 1s to Au 4f intensity.

		<b>C-C*</b>	<b>C-C</b>	<b>CC*/total peak area</b>	<b>Calculated thickness, Å (C/Au)</b>
		location/area	location/area		
host-guest (stearic acid) assembly in	benzene	285.6/0.279	284.8/0.562	<b>0.28</b>	<b>32.19</b>
	cyclohexane	285.5/0.281	284.8/0.620	<b>0.28</b>	<b>30.57</b>
	dibutyl ether	285.3/0.111	284.7/0.542	<b>0.11</b>	<b>13.85</b>
	dichloromethane	285.4/0.273	284.8/0.603	<b>0.27</b>	<b>26.19</b>
	ethanol	285.0/0.545	284.6/0.281	<b>0.55</b>	<b>42.10</b>
	heptane	284.9/0.605	284.5/0.195	<b>0.61</b>	<b>61.07</b>
	THF	285.3/0.200	284.7/0.393	<b>0.20</b>	<b>21.44</b>
host monolayer only		-	<b>284.99</b>		<b>10.75</b>
		<b>C-C*</b>	<b>C-C</b>	<b>CC*/total peak area</b>	<b>Calculated thickness, Å (C/Au)</b>
		location/area	location/area		
host-guest (naphthyl stearate) assembly in	benzene	285.7/0.171	284.8/0.639	<b>0.17</b>	<b>25.27</b>
	dibutyl ether	285.9/0.254	284.8/0.539	<b>0.25</b>	<b>22.20</b>
	dichloromethane	285.4/0.129	284.8/0.581	<b>0.13</b>	<b>22.42</b>
	cyclohexane	285.6/0.336	284.8/0.459	<b>0.34</b>	<b>26.61</b>
	heptane	285.2/0.305	284.6/0.477	<b>0.31</b>	<b>26.76</b>
	THF	285.3/0.164	284.7/0.502	<b>0.16</b>	<b>17.23</b>
	toluene	285.7/0.198	284.8/0.516	<b>0.20</b>	<b>21.32</b>
host monolayer only		-	<b>284.99</b>		<b>10.75</b>

In the case of all host-guest assemblies investigated, we observed the following: (i) the peak-intensity of carbon significantly increases after immersion of host-SAMs in guest solution in various solvents, (ii) there are unusual C-C\* peaks with different binding energies in the C 1s region, (iii) estimated values of CC\*/total area under the C 1s peak are analogous with the increment of the intensity of host-guest assemblies. After considering all results, we reach the conclusion that guest molecules were intercalated into the host-cavities and that in some cases multilayer formation was observed.

## 5.4. Conclusions

We demonstrated that guest molecules were intercalated into host-cavities on a surface using QCM-D and XPS measurements. Data analysis from QCM-D measurement revealed that host-guest assemblies become rigid during guest adsorption and thus, the Sauerbrey equation is valid in this regime. The reversibility of the intercalation process allows guest **1** already situated in host-cavities to be replaced with guest **2** under well-regulated solvent conditions. The XPS analysis of host-guest assemblies also revealed the presence of functional moieties of guest molecules. Unfortunately, the effect of solvent on the formation of host-guest assemblies could not be determined via XPS as the time-scale of immersion in the guest solutions was much greater than the time-scale of guest-intercalation.

## 5.5. Summary

Self-assembled monolayers of (10-octadecyl)-9-anthracenethiol (host-SAMs) on Au were prepared. To examine the intercalation of structurally homologous guest molecules, e.g., stearic acid or naphthyl labeled hydrophobic molecules, into the cavities of host-SAMs and the structural properties of host-guest assemblies, a combined quartz crystal microbalance with dissipation (QCM-D) and X-ray photoelectron spectroscopy (XPS) study of molecular adsorption was performed. The behavior of the frequency shift of the QCM-D measurements indicated that molecular adsorption of guest molecules into host-SAMs is a reversible

process, which proves the possibility of exchange and regeneration of molecules situated in host-cavities. The D-factor analysis from QCM-D showed two phases with considerably different slopes during the adsorption process. In particular, the second phase with the lower slope ( $\partial D/\partial f$ ) is associated with the formation of rigid host-guest assemblies via intercalation of guest molecules and thus, the Sauerbrey equation is valid in this regime. Based on the Sauerbrey equation, the thickness of host-guest assembly and the number of molecules in the cavities were estimated. XPS analysis of host-guest assemblies prepared from various solvent environments demonstrated the presence of functional groups on the surface based on an increase in the carbon peak. Further high resolution analysis of the C 1s peak revealed that the ratio of CC\* to total peak area can be related to the structural properties of the host-guest assemblies. XPS data was also analyzed to estimate layer thicknesses of the host-guest assemblies. The thickness of host-guest assemblies determined using XPS agreed closely with those based on QCM data.

## 5.6. Reference

- 
- <sup>1</sup> (a) Berggren, K. K.; Bard, A.; Wilbur, J. L.; Gillaspay, J. D.; Helg, A. G.; McClelland, J. J.; Rolston, S. L.; Philips, W. D.; Prentiss, M.; Whitesides, G. M. *Science* **1995**, *269*, 1255. (b) Kim, E.; Whitesides, G. M.; Lee, L. K.; Smith, S. P.; Prentiss, M. *Adv. Mater.* **1996**, *8*, 139. (c) Hodneland, C. D.; Mrksich, M. *J. Am. Chem. Soc.* **2000**, *122*, 4235. (d) Aswal, D. K.; Lenfant, S.; Guerin, D.; Yakhmi, J. V.; Vuillaume, D. *Anal. Chim. Acta* **2006**, *568*, 84. (e) Phares, N.; White, R. J.; Plaxco, K. W. *Anal. Chem.* **2009**, *81*, 1095.
  - <sup>2</sup> Plaut, D. J.; Martin, S. M.; Kjaer, K.; Weygand, M. J.; Lahav, M.; Leiserowitz, L.; Weissbuch, I.; Ward, M. D. *J. Am. Chem. Soc.* **2003**, *125*, 15922.
  - <sup>3</sup> Love, J. C.; Estroff, L. A.; Krebel, J. K.; Nuzzo, R. G.; Whitesides, G. M. *Chem. Rev.* **2005**, *105*, 1103
  - <sup>4</sup> Miao, X.; Xu, L.; Li, Y.; Li, Z.; Zhou, J.; Deng, W. *Chem. Commun.* **2010**, *46*, 8830
  - <sup>5</sup> Furukawa, S.; Tahara, K.; De Schryver, F. C.; Van der Auweraer, M.; Tobe, Y.; De Feyter, S. *Angew. Chem. Int. Ed.* **2007**, *46*, 2831
  - <sup>6</sup> Theobald, J. A.; Oxtoby, N. S.; Phillips, M. A.; Champness, N. R.; Benton, P. H. *Nature* **2003**, *424*, 1029
  - <sup>7</sup> Stepanow, S.; Lingenfelder, M.; Dmitriev, A.; Spillmann, H.; Delvigne, E.; Lin, N.; Deng, X.; Cai, C.; Barth, J. V. Kern, K. *Nature Mater.* **2004**, *3*, 229
  - <sup>8</sup> Kudernac, .; Lei, S.; Elemans, J. A. A. W.; De Feyter, S. *Chem. Soc. Rev.* **2009**, *38*, 402

- 
- <sup>9</sup> Testaferri, L.; Tiecco, M.; Tingoli, M.; Chianelli, D.; Montanucci, M. *Synthesis* **1983**, 9, 751
- <sup>10</sup> Chan, D. M. T.; Monaco, K. L.; Wang, R.; Winters, M. P. *Tetrahedron Letters* **1998**, 39, 2933
- <sup>11</sup> Dou, R.-F.; Ma, X.-C.; Xi, L.; Yip, H. L.; Wong, K. Yl.; Lau, W. M.; Jia, J.-F., Xue, Q.-K.; Yang, W.-S.; Ma, H.; Jen A. K.-Y. *Langmuir* **2006**, 22, 3049
- <sup>12</sup> Höök, F.; Rodahl, M.; Brezezinski, P.; Kasemo, B. *Langmuir* **1998**, 14, 729
- <sup>13</sup> Mann, S.; Heywood, B. R.; Rajam, S.; Birchall, J. D. *Nature* **1988**, 334, 692
- <sup>14</sup> Rabinovitch, W.; Robertson, R. F.; Mason, S. G. *Can. J. Chem.* **1960**, 38, 1881
- <sup>15</sup> Shaitan, K. V.; Pustoshilov, P. P. *Biophysics* **1999**, 44, 429
- <sup>16</sup> Koga, T.; Kawazumi, H.; Nagamura, T.; Ogawa, T. *Analytical Sciences* **1992**, 8, 259
- <sup>17</sup> Arduengo III, A. J.; Moran, J. R.; Rodriguez-parada, J.; Ward, M. D. *J. Am. Chem. Soc.* **1990**, 112, 6153
- <sup>18</sup> Gouzman, I.; Dubey, M.; Carolus M. D.; Schwartz, J.; Bernasek, S. L. *Surface Science* **2006**, 600, 773
- <sup>19</sup> Castner, G. D.; Hinds, K.; Grainger D. W. *Langmuir* **1996**, 12, 5083
- <sup>20</sup> Dannenberger, O.; Weiss, K.; Himmel, H.-J.; Jäger, B.; Buck, M.; Wöll, Ch. *Thin Solid Films* **1997**, 307, 183

# Chapter 6

## Conclusions and Future work

Surface functionality is of importance in diverse applications such as catalysis, sensing, and bio-compatibility. These applications can benefit from the control of specific chemical and physical surface properties. Self-assembled monolayers, Langmuir-Blodgett films, and other surface-confined assemblies have been acknowledged as a practical strategies for creating tailor-made functional surfaces; however the control of the surface properties via these methods is dependent on the properties of the molecules that are built in the final structure. Thus, in many cases difficult organic synthesis is required to produce the  $\alpha$ - $\omega$  molecules, this approach has limited potential applications. We have developed new methods to construct functional nano-structured host-guest thin films as well as techniques to complement conventional fabrication methods.

The preceding chapters have described the development and characterization of host-guest assemblies and the feasibility for generating of functional surfaces and regenerating surface properties via the intercalation of functional guests into the cavities of a host monolayer. 3-dimensional host structures with cavities were constructed on solid substrates using Langmuir-Blodgett deposition and self-assembly techniques. We have shown that structurally homologous guest molecules with various attached functional groups can be intercalated into the cavities formed between hydrophobe arrays in a host monolayer at a solid interface. This approach allows the creation of a number of different functional surfaces

based on the same host monolayer. We have confirmed our hypothesis that thin films consisting of alkane chains separated by spacer groups in order to create a low-density framework can be used to intercalate alkane substituted guest molecules from solution, thereby creating functionalized surfaces.

Initially, we generated two-dimensional host-guest assemblies based on a hydrogen-bonded **GS** network and various functional alkane guests at the air-aqueous interface, and deposited them onto a Si substrate via the Langmuir-Blodgett technique. The stability of the host-guest assemblies and the feasibility of exchanging molecular guests under exposure to various organic solvent environments were determined via XRR analysis. The results indicated that the stability of the host-guest assemblies could not be achieved due to their weak interactions with the Si surface. Unfortunately, the intercalation of guest molecules into a guest-free host monolayer was not confirmed in this study. Despite the instability of some of the host-guest assemblies when immersed in solvent, the formation of the host-guest assemblies at the air-aqueous interface and their subsequent transfer to a solid substrate suggested a common host monolayer for the inclusion of various functional guests. Furthermore, this suggested an approach for the immobilization of the host-monolayers with integral space molecules.

We then studied effective methodologies to construct low-density self-assembled monolayer (LDSAMs) with integral cavities on a targeted solid surface in a stepwise fashion. In a stepwise reaction based on hydrolytic or silane chemistry, integral spacer molecules such as anthracene-derivatives are anchored to the substrates and then long alkane chains are attached to the spacer molecules. We confirmed that the resulting LDSAMs did not have a densely packed monolayer quality via FTIR, XPS, and XRR measurements. This suggested that the LDSAMs (with cavities) might be capable of accommodating guest molecules, thereby regenerating a functional surface via intercalation of guest molecules.

Finally, we investigated the feasibility of using LDSAMs to generate functional surfaces via the intercalation of guest molecules from solution. Self-assembled monolayers of (10-octadecyl)-9-anthracenethiol (host-SAMs) on Au were prepared. Combined studies of QCM-D and XPS revealed that several different guest molecules were intercalated into the host-cavities from a number of solvents. QCM-D data showed that the intercalation of guest

molecules was a reversible process. The reversibility of the intercalation process allows guest **1** already situated in a host-cavity to be replaced with guest **2** under well-regulated solvent conditions. Unfortunately, the effect of solvent on the formation of host-guest assemblies could not be determined via XPS as the time-scale of immersion in the guest solutions was much greater than the time-scale of guest intercalation. In conclusion, well-ordered LDSAM host films with cavities on a solid surface can be used to separate the functionality of the monolayer surface from the inherent structure of the host molecules. This could allow the creation of a library of different functional surfaces, or the regeneration of damaged or inactive surfaces, via the use of alkane-tethered functional guest molecules and the manipulation of solvent conditions for guest intercalation and removal.

Based on the results of the current work, future efforts should be directed toward applying the host monolayer system developed here to various substrates. Provided that surface host-guest assembly can be generated on a semiconductor substrate such as Si, it is possible to construct highly functional composites via the fusion of the functions of both the substrate and the host-guest assembly. We expect that these combined features, such as electrochemical activity and high electron communication, may make the host-guest assembly a promising material for chemical and biological applications. For example, Patolsky et al reported that Si nanowire arrays modified with antibodies for influenza **A** showed discrete conductance changes characteristic of binding and unbinding in the presence of influenza **A**. Biosensors of this type based on Si nanowire are sensitive enough to detect a single virus level. Considering the selectivity to diverse biomolecules, however, it is necessary to modify the device surface with a large number of antibodies. We can utilize the host-guest assembly system in order to improve the selective surface binding with targeted biomolecules via the simple synthesis necessary to append a proper antibody to the end of the alkane guest. Guest molecules also often need to be embedded temporarily in host-SAMs during detection. We could use a light-induced molecular motion as a switch to control release of the guest molecules. By introducing azobenzene group in the alkane chain of the host-SAM, it may be possible to control the intercalation and release of guest molecules.

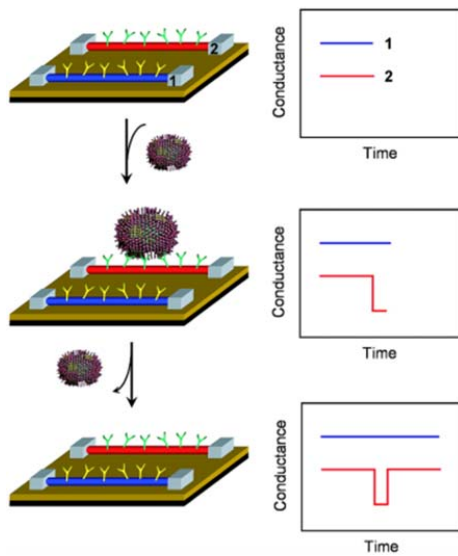
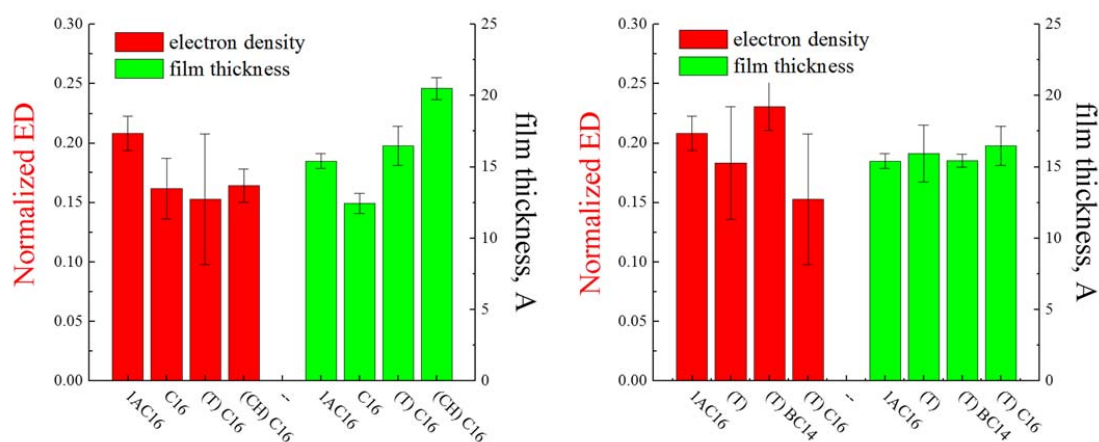


**Figure 6. 1.** Nanowire-based detection of single virus. Schematic illustration shows two nanowire devices, 1 and 2, where the nanowires are modified with different antibody receptors. Specific binding of a single virus to the receptors on nanowire 2 produces a conductance change (*Right*) characteristic of the surface charge of the virus only in nanowire 2. When the virus unbinds from the surface the conductance returns to the baseline value. \*This image was copied from Patolsky, F. et al. *PNAS* **2004**,*101*, 14017.

# Appendix

## Supporting information for Low-Density Self-Assembled Monolayers Based on Integral Spacer

**Appendix A** - Electron density profiles for host-guest assemblies using LDSAM immersed in hexadecane solution in different solvents or different guest solution in toluene.



**S 1.** LDSAM (1AC16) was immersed in hexadecane solution in different solvents or different guest solution in toluene.

**1AC16:** LDSAM

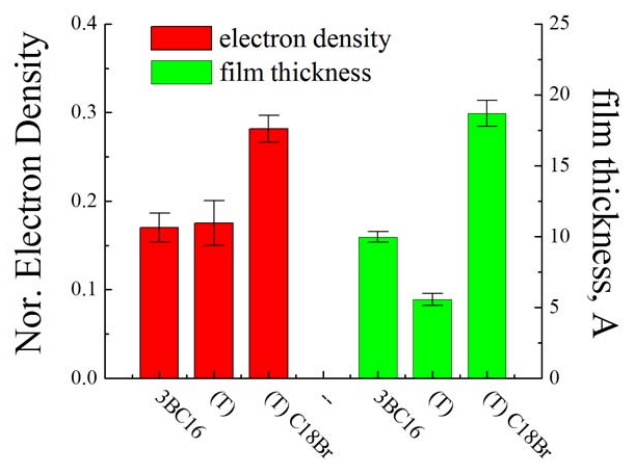
**C16:** LDSAM was immersed in hexadecane solution

**(T)C16:** LDSAM was immersed in hexadecane solution in toluene

**(CH)C16:** LDSAM was immersed in hexadecane solution in cyclohexane

**(T):** LDSAM was immersed in pure toluene

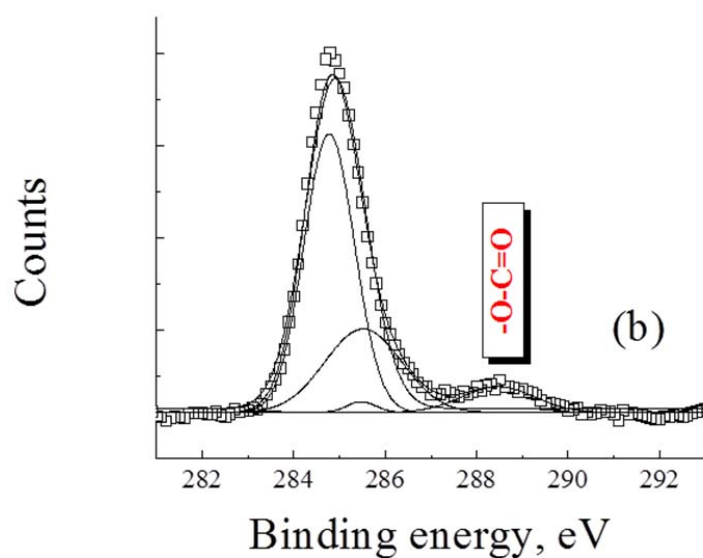
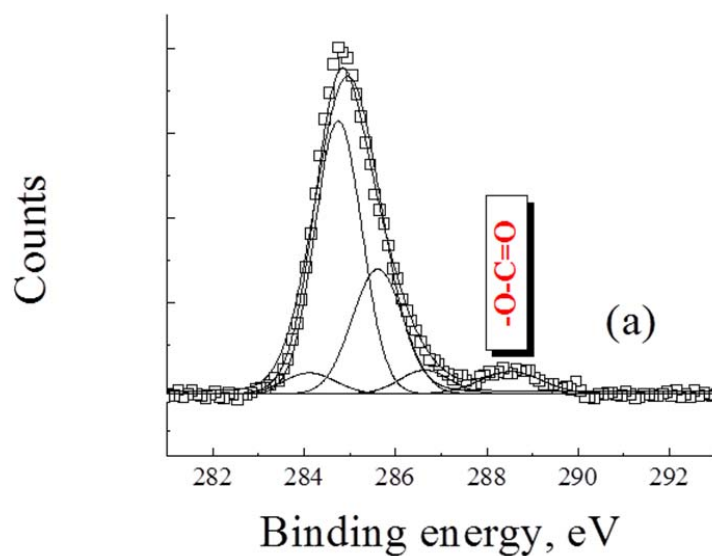
**(T)BC14:** LDSAM was immersed in 1-phenyltetradecane solution in toluene

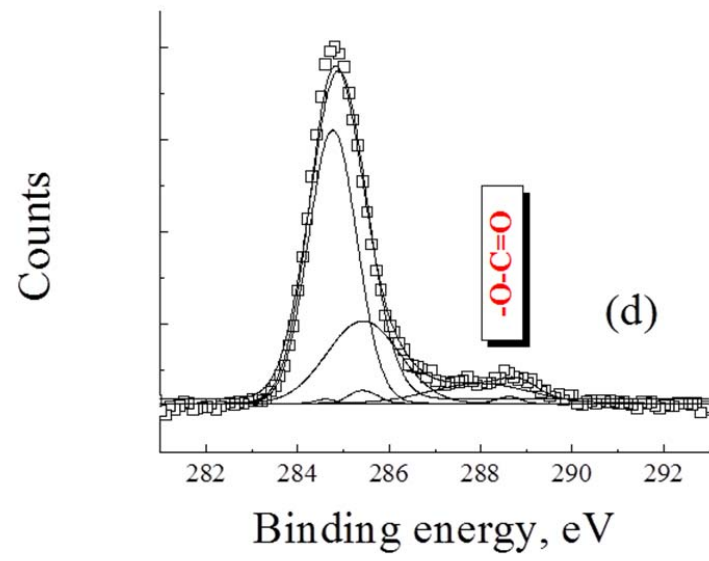
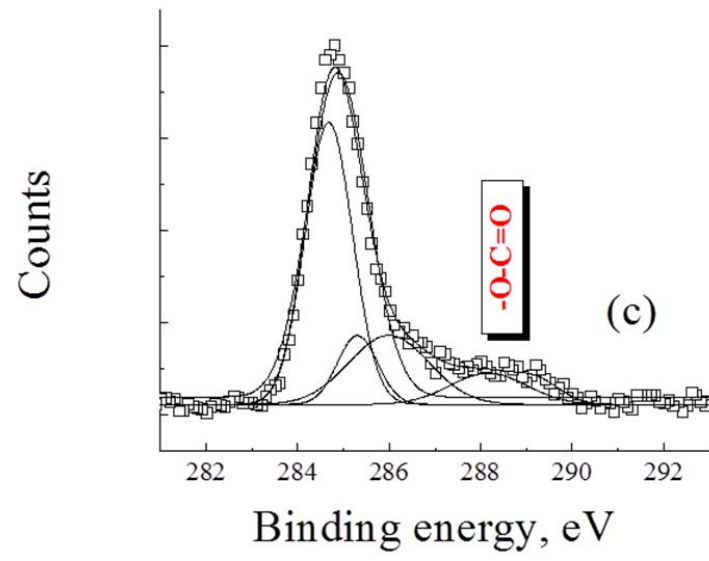


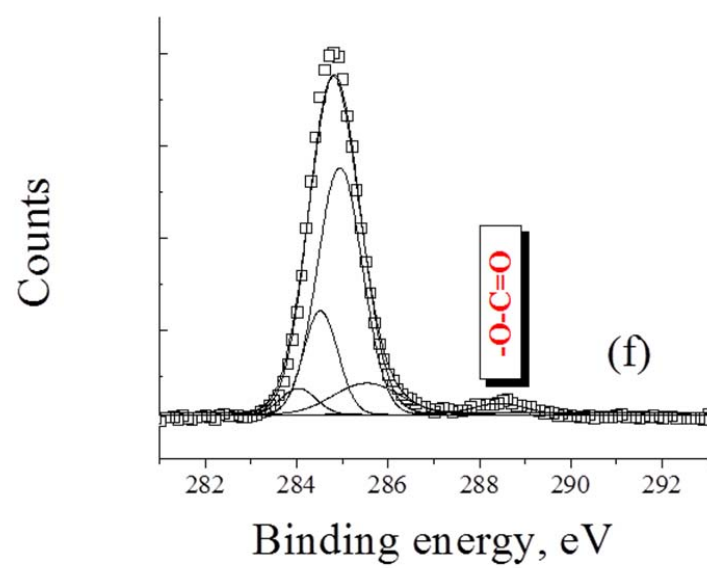
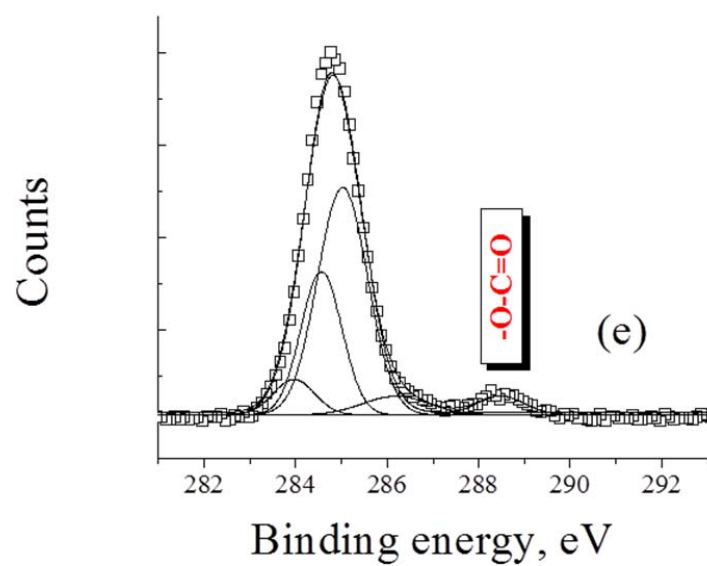
**S 2.** LDSAM (3BC16) was immersed in hexadecane solution in different solvents or different guest solution in toluene.

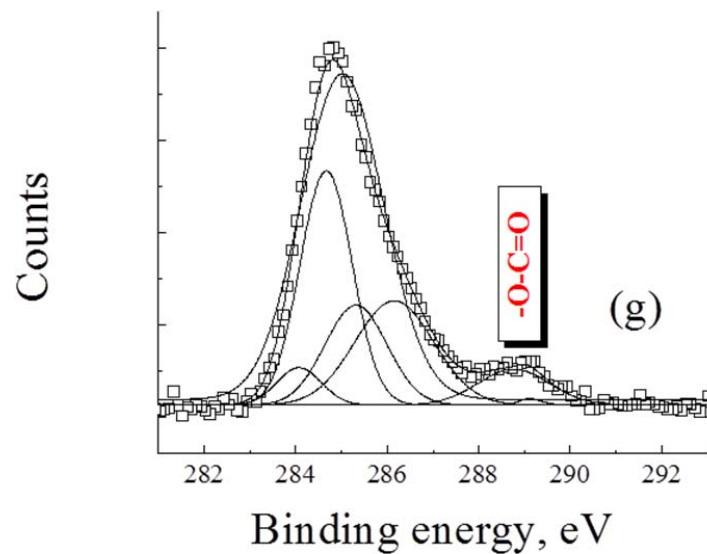
**Supporting information for Host-Guest Assemblies via the Intercalation of Guest molecules on Low-Density Self-Assembled Monolayer**

**Appendix B – XPS data for Host-Guest Assemblies via the Intercalation of Guest molecules on Low-Density Self-Assembled Monolayer**

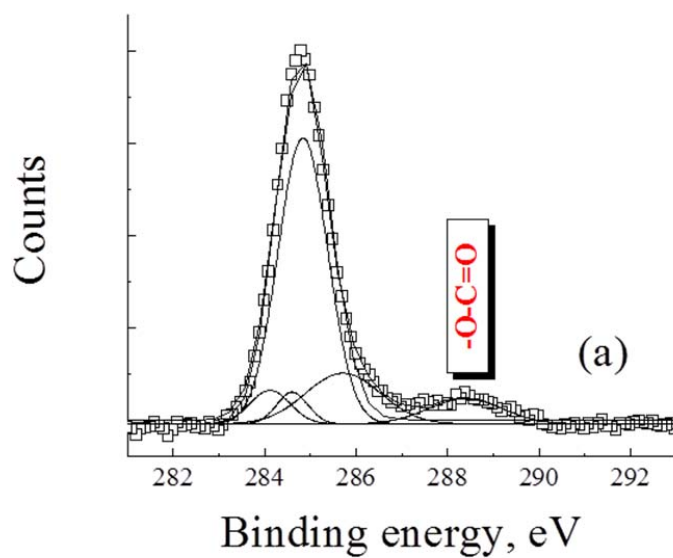


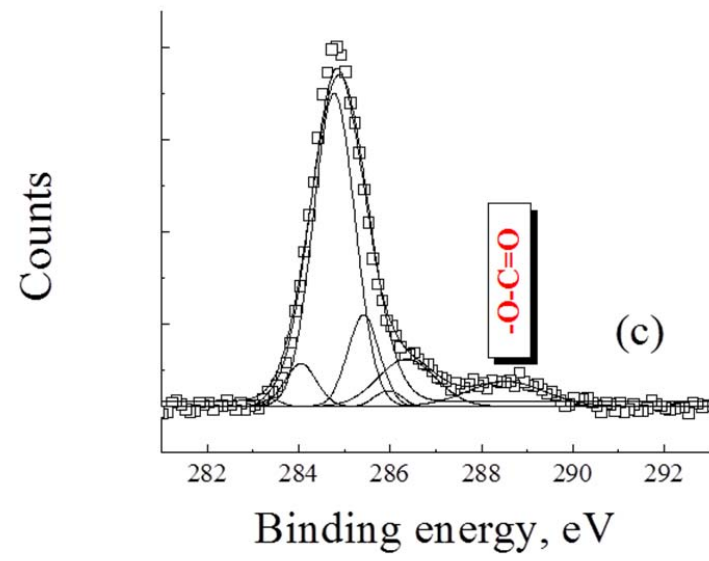
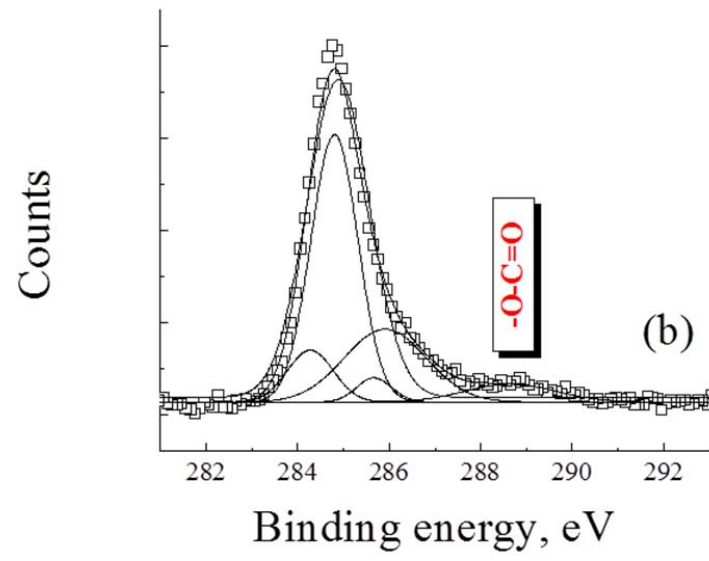


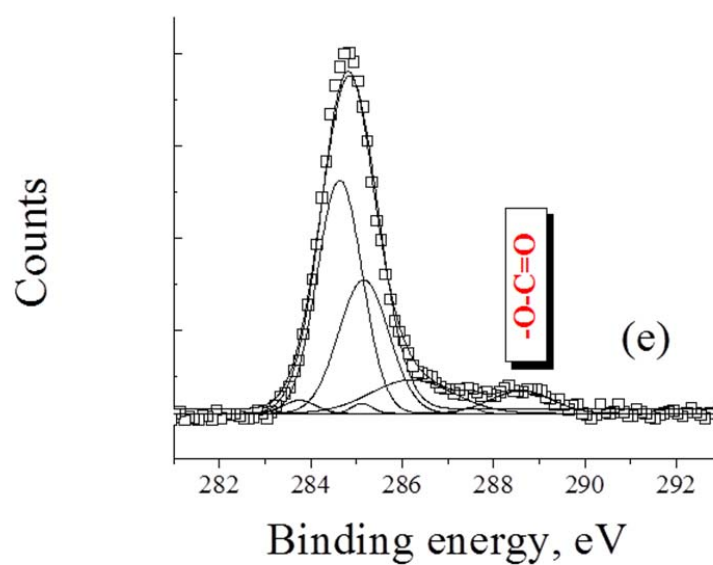
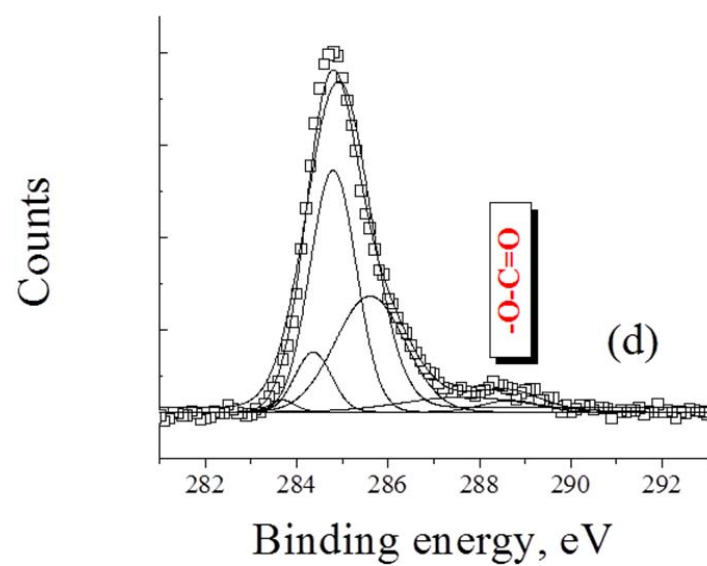


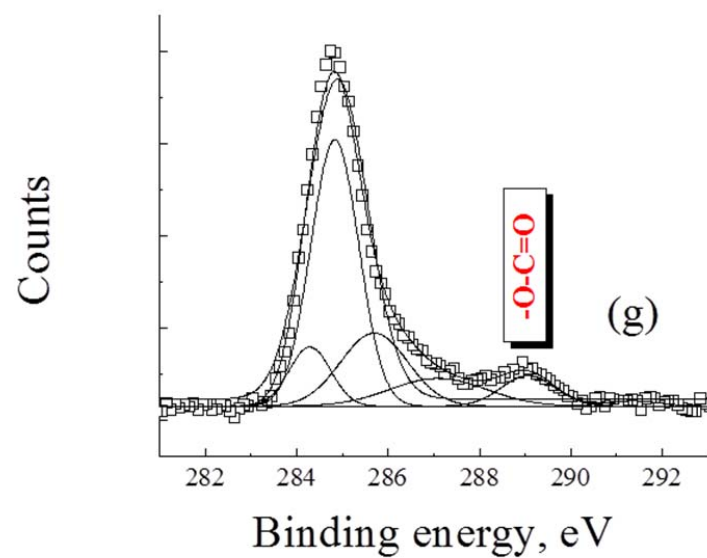
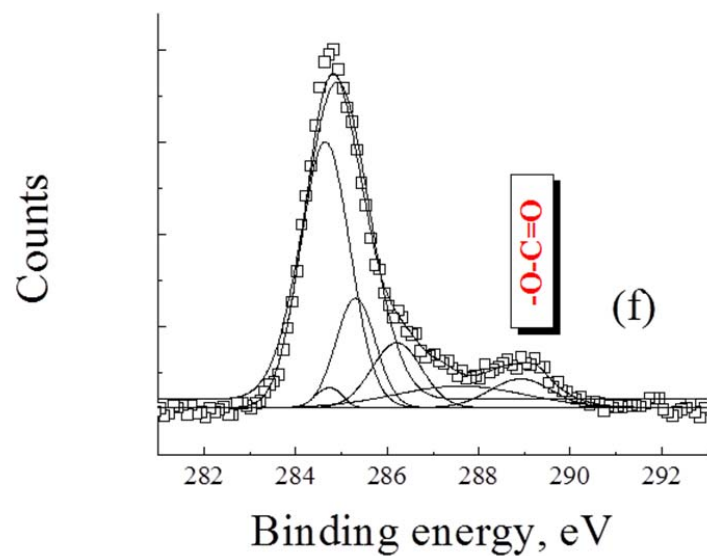


**S 3.** Complete XPS data for host-guest assemblies with **stearic acid** in various solvents. (a) benzene, (b) cyclohexane, (c) dibutyl ether, (d) dichloromethane, (e) ethanol, (f) heptane, and (g) tetrahydrofuran.

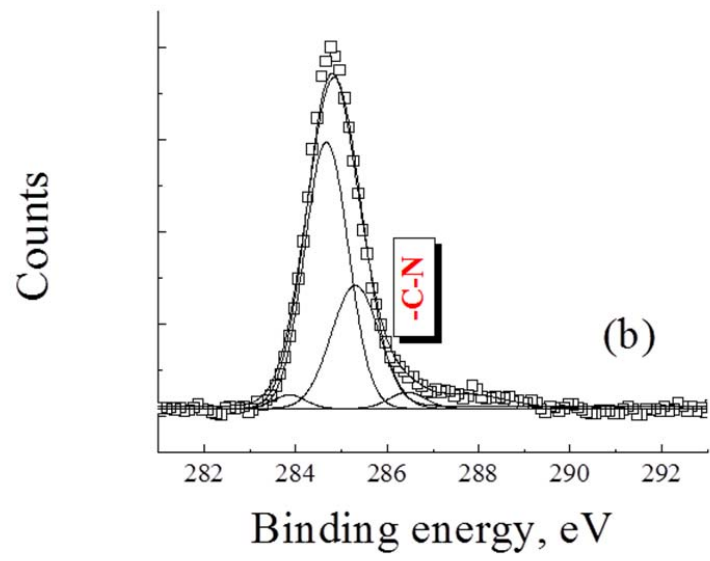
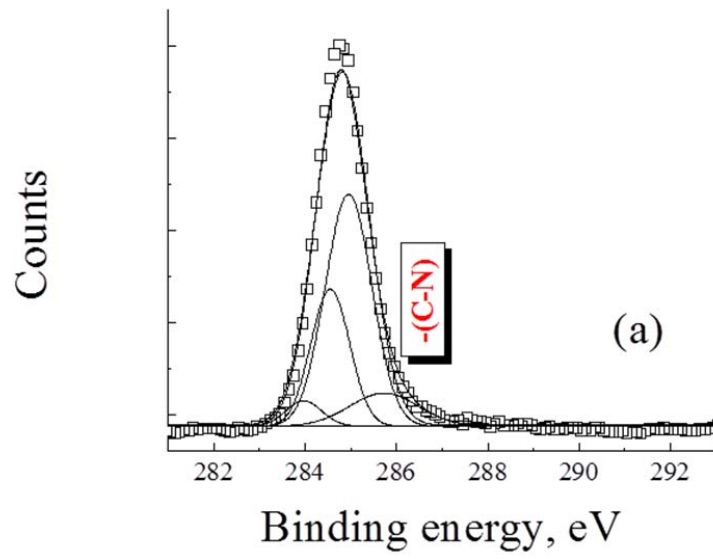


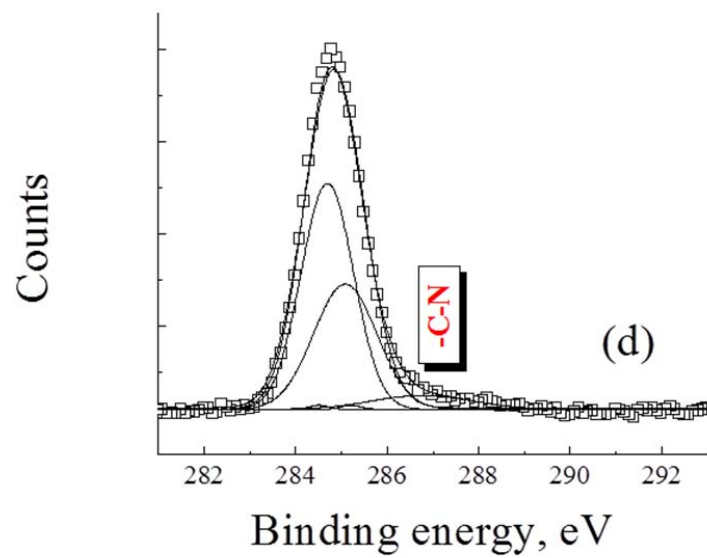
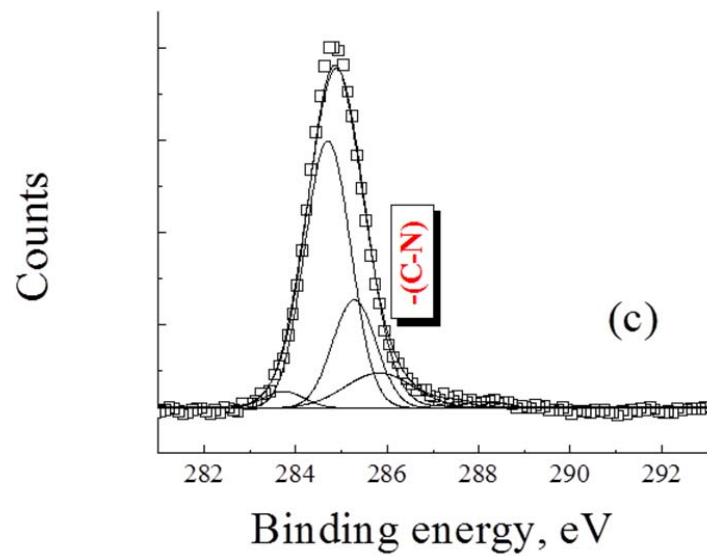


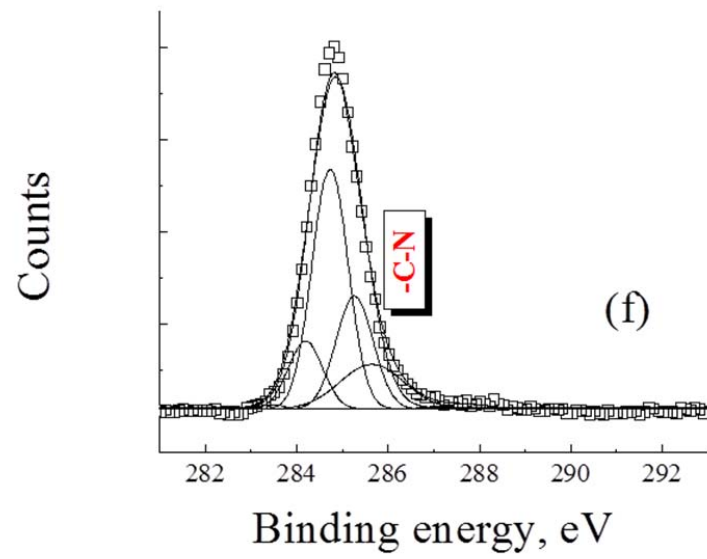
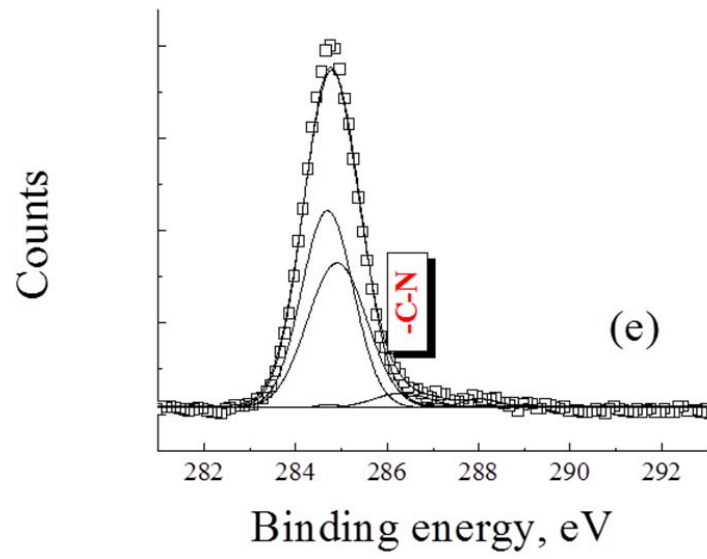


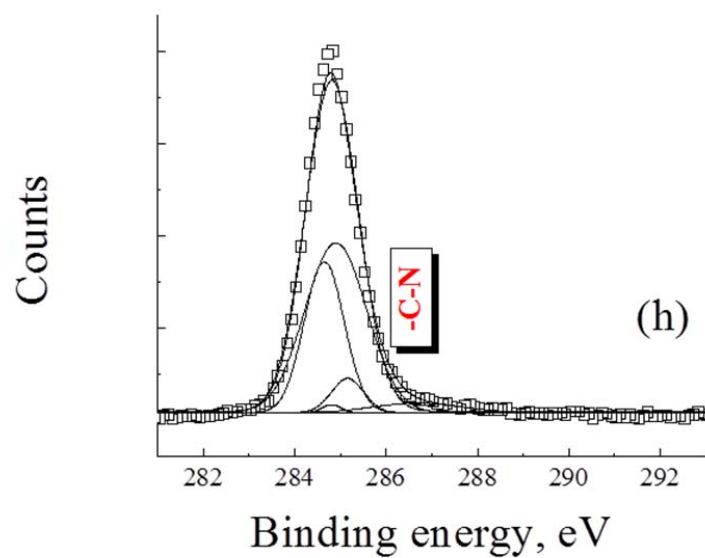
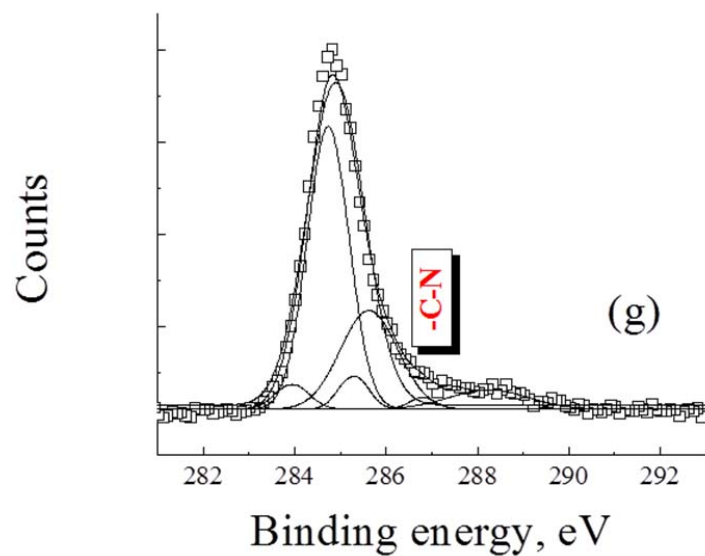


**S 4.** Complete XPS data for host-guest assemblies with **naphthyl stearate** in various solvents. (a) benzene, (b) dibutyl ether, (c) dichloromethane, (d) cyclohexane, (e) heptane, (f) tetrahydrofuran, and (g) toluene.

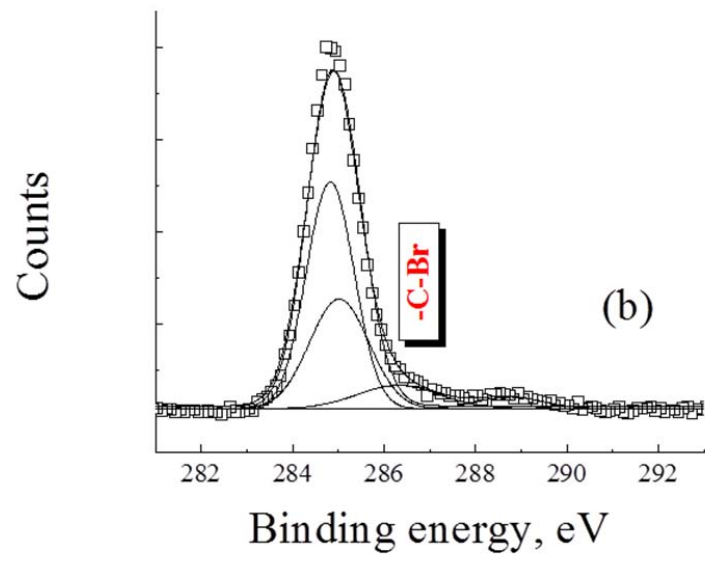
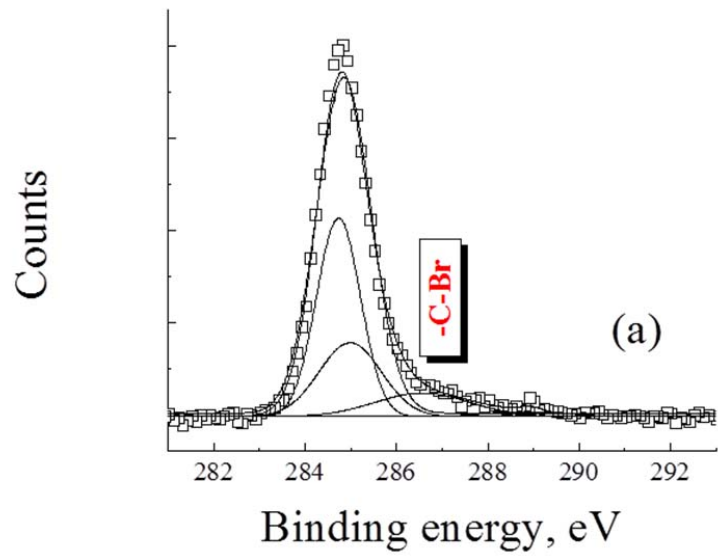


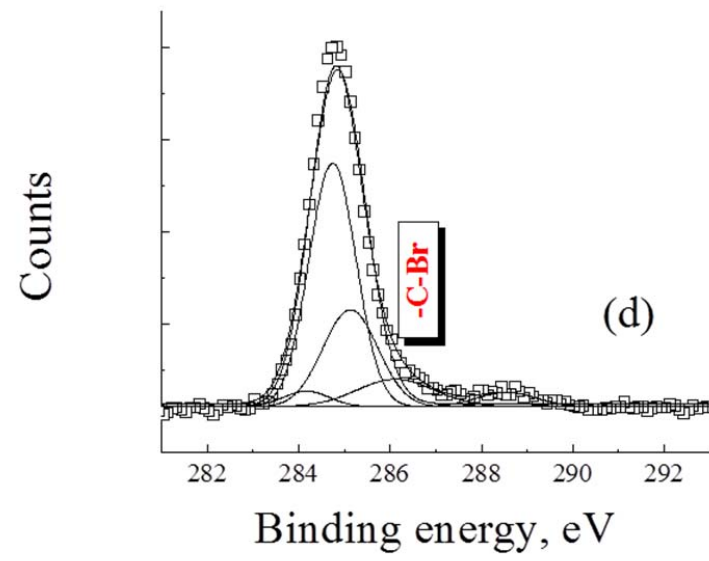
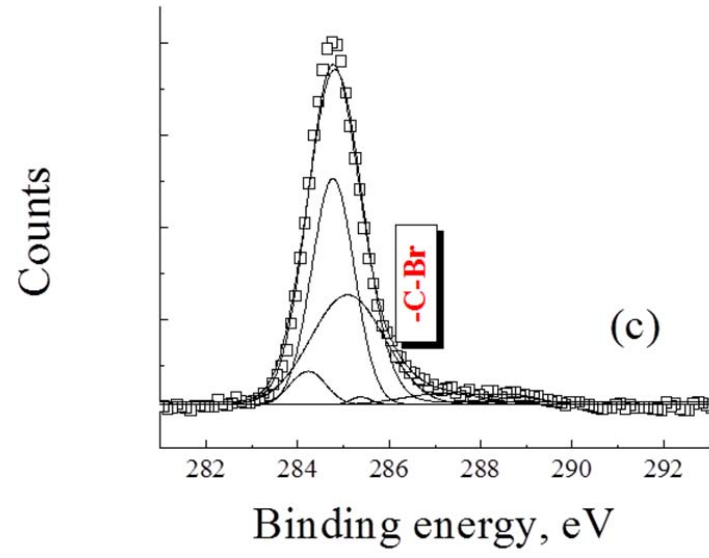


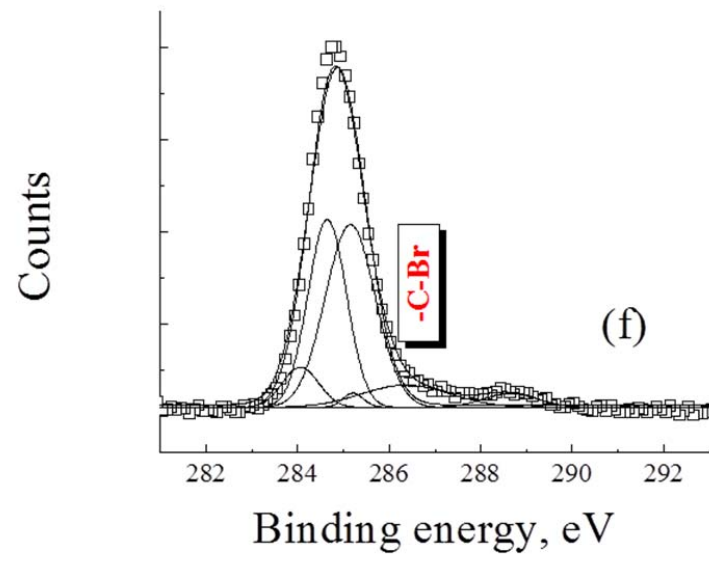
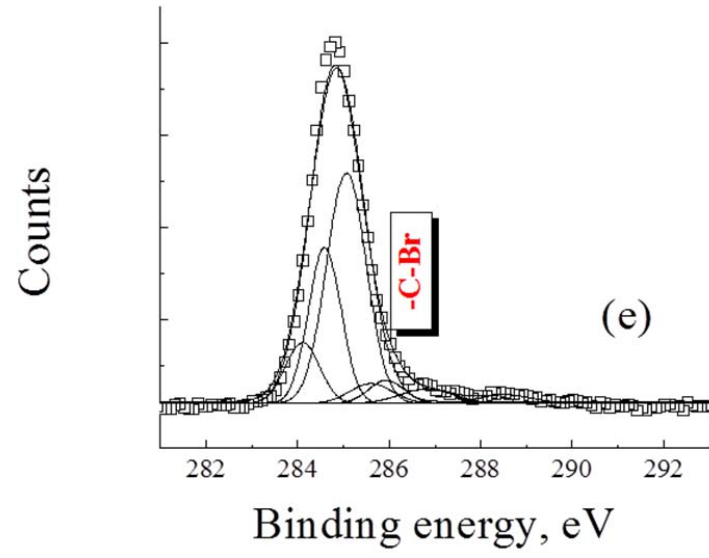


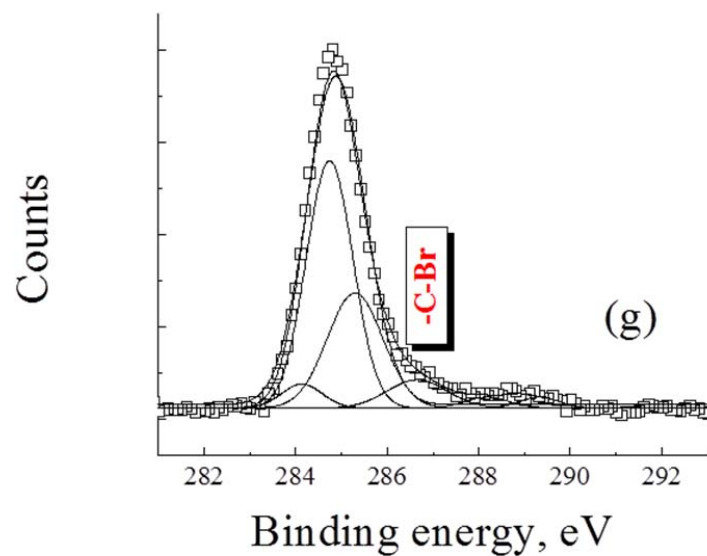


**S 5.** Complete XPS data for host-guest assemblies with **octadecyl amine** in various solvents. (a) benzene, (b) cyclohexane, (c) dibutyl ether, (d) dichloromethane, (e) ethanol, (f) heptane, (g) tetrahydrofuran, and (h) toluene.

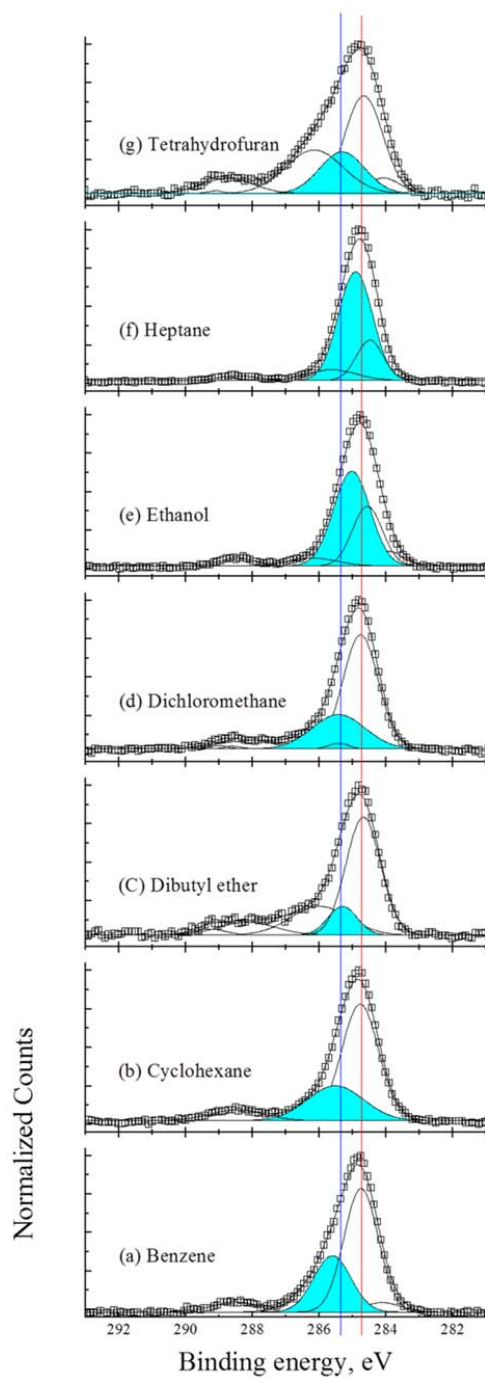




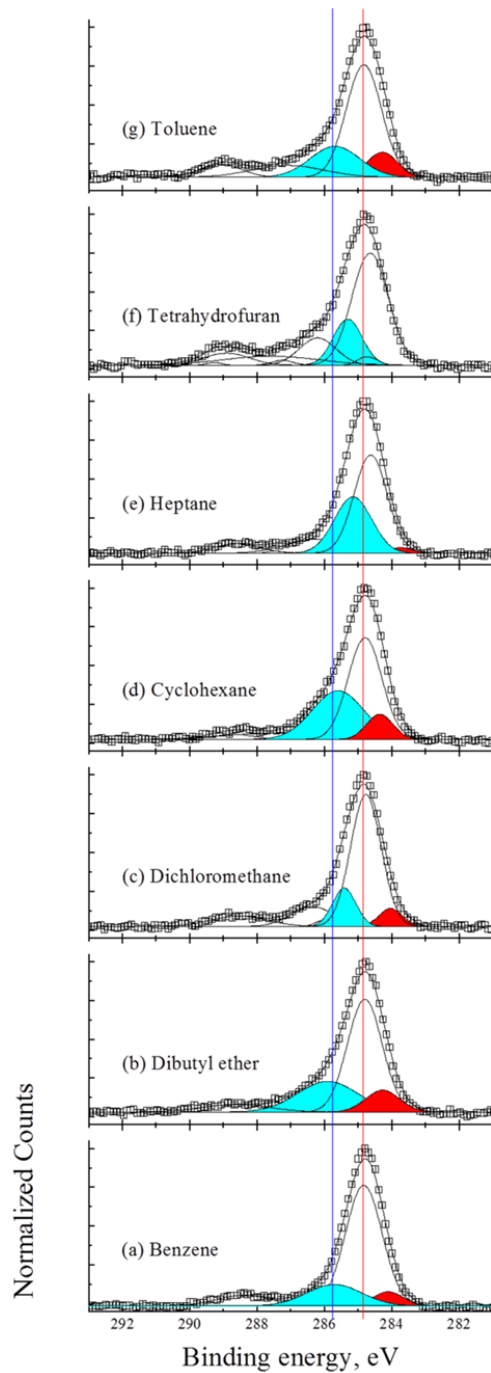




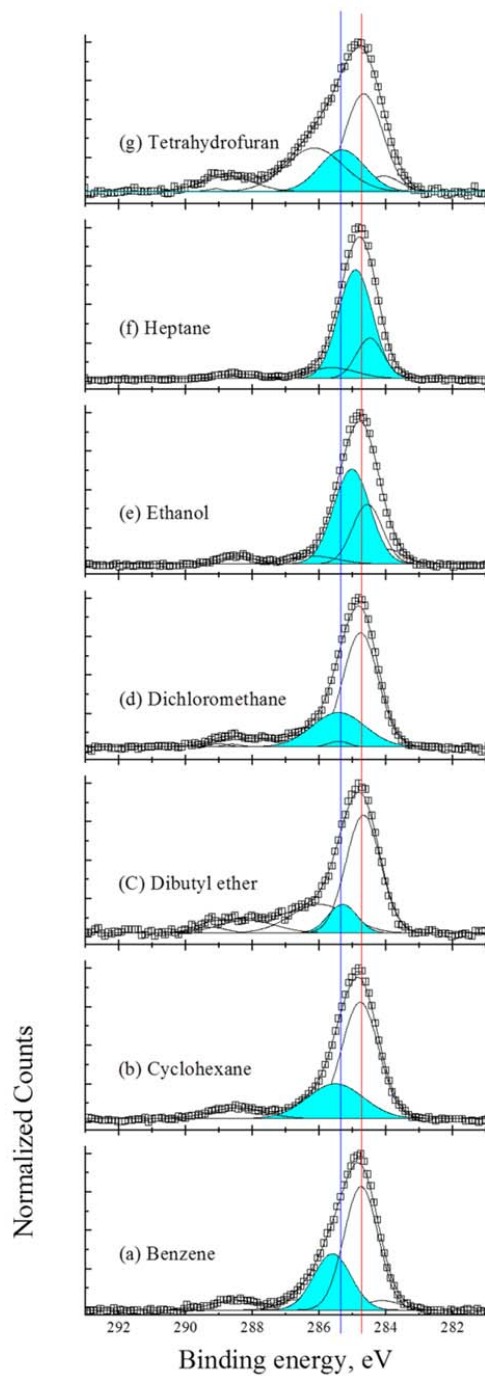
**S 6.** Complete XPS data for host-guest assemblies with **1-bromooctadecane** in various solvents. (a) benzene, (b) cyclohexane, (c) dibutyl ether, (d) dichloromethane, (e) ethanol, (f) heptane, and (g) tetrahydrofuran.



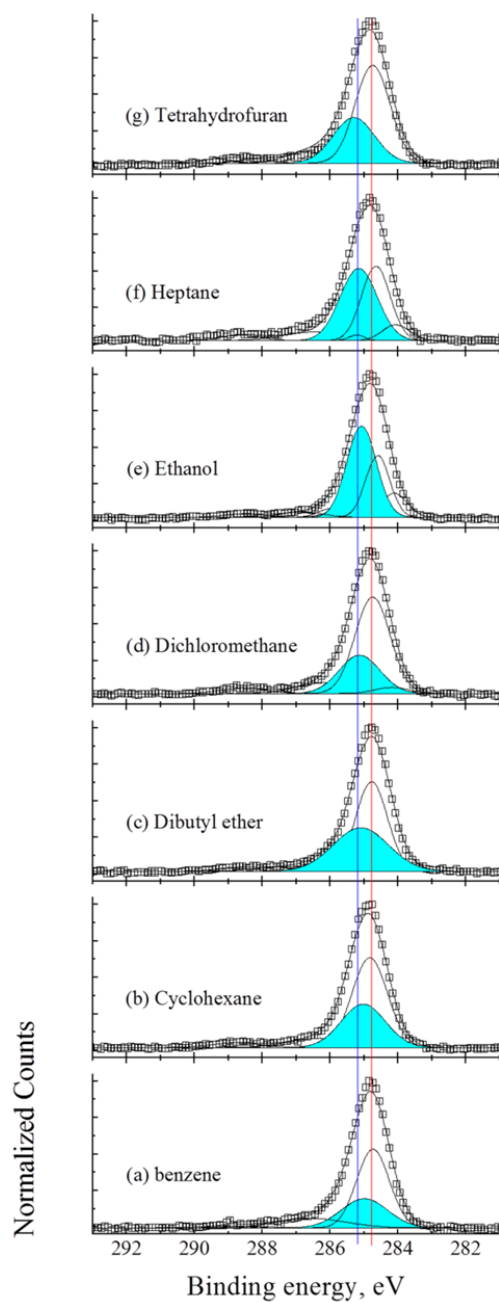
**S 7.** CC\* extraction from the high resolution XPS spectra for C 1s for host-guest assemblies with **stearic acid** in various solvents.



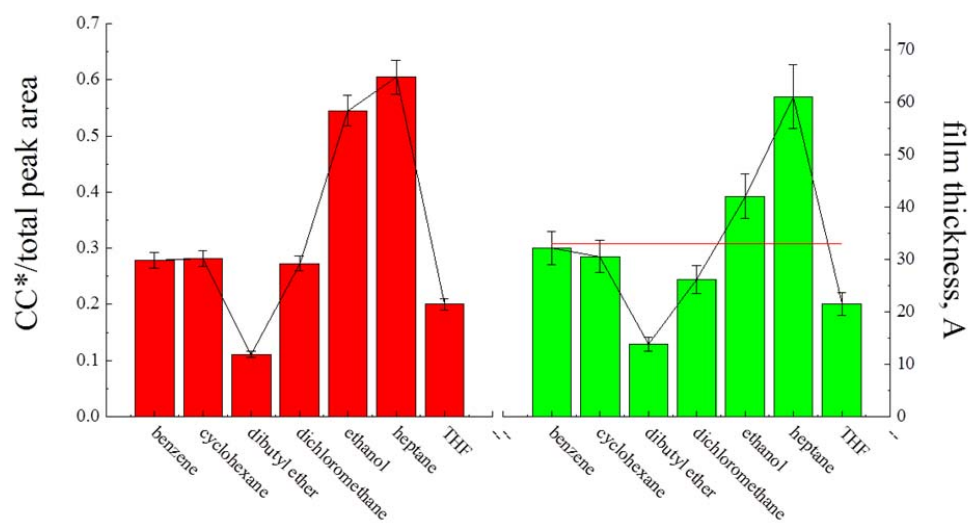
**S 8.** CC\* extraction from the high resolution XPS spectra for C 1s for host-guest assemblies with **naphthyl stearate** in various solvents.



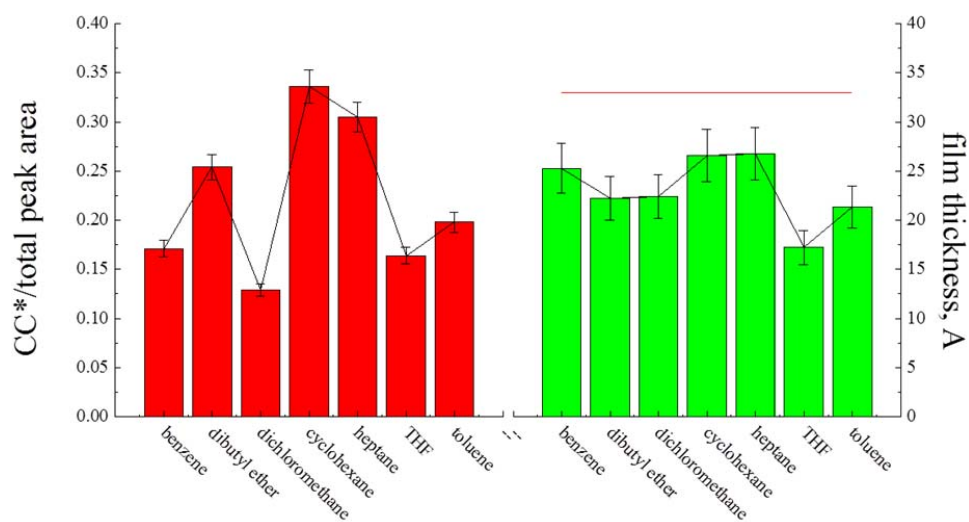
**S 9.** CC\* extraction from the high resolution XPS spectra for C 1s for host-guest assemblies with **octadecyl amine** in various solvents.



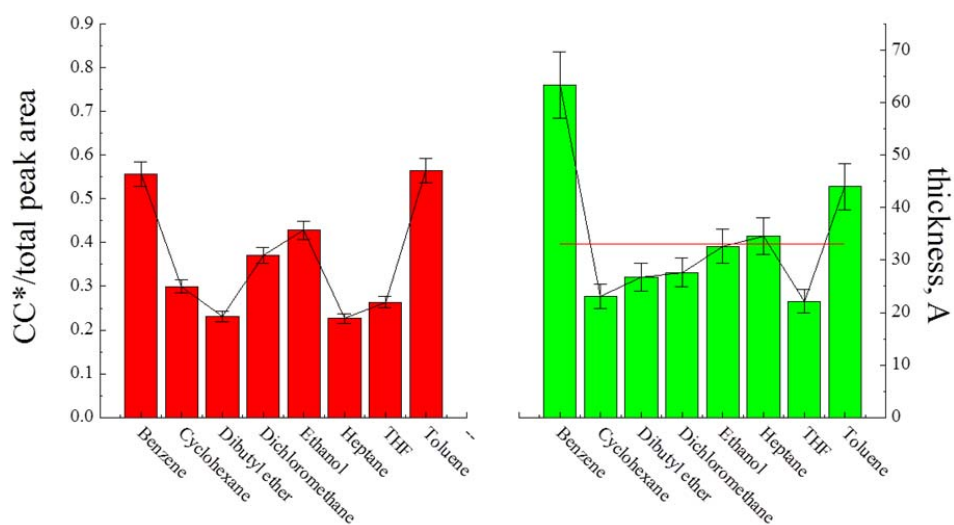
**S 10.** CC\* extraction from the high resolution XPS spectra for C 1s for host-guest assemblies with **1-bromooctadecane** in various solvents.



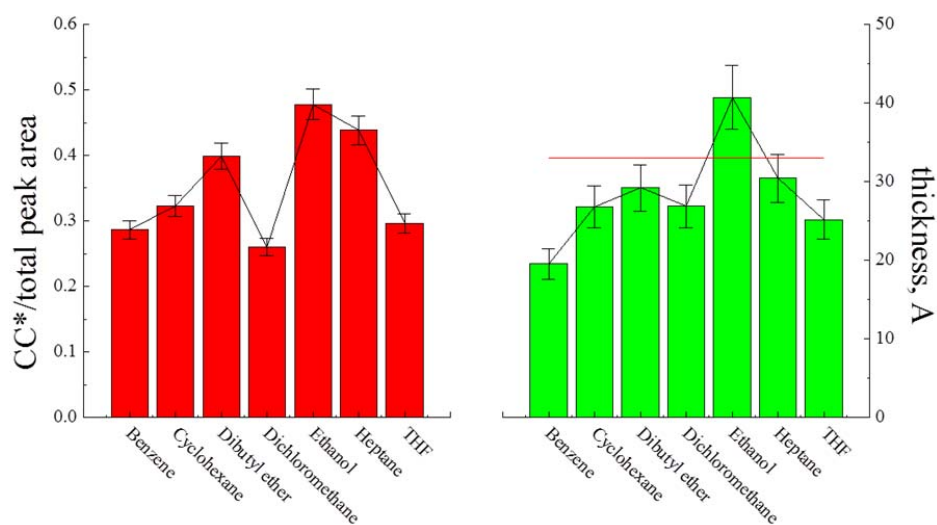
**S 11.** Summary of XPS data for host-guest assemblies with **stearic acid** in various solvents: the ratio of CC\* to total peak area (red column) and film thickness (green column)



**S 12.** Summary of XPS data for host-guest assemblies with **naphthyl stearate** in various solvents: the ratio of CC\* to total peak area (red column) and film thickness (green column)



**S 13.** Summary of XPS data for host-guest assemblies with **octadecyl amine** in various solvents: the ratio of CC\* to total peak area (red column) and film thickness (green column)

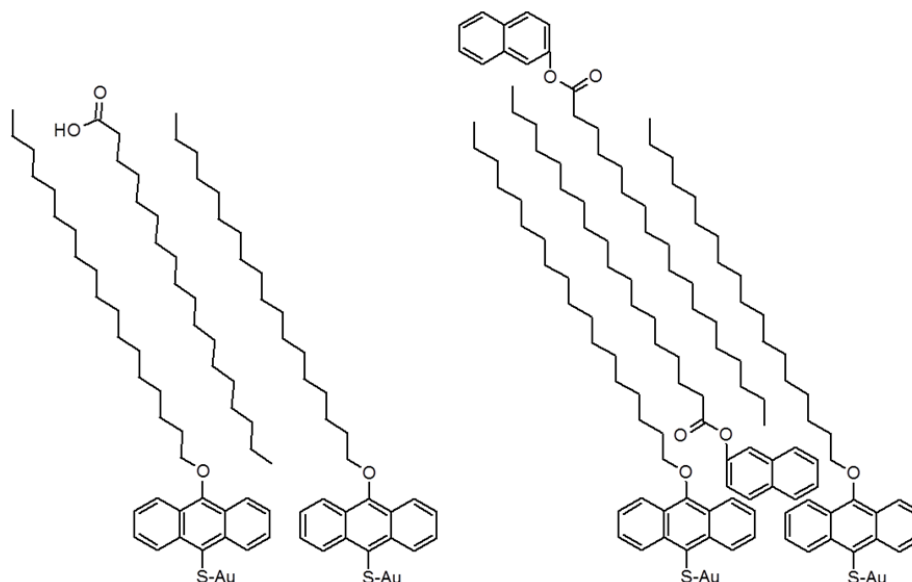


**S 14.** Summary of XPS data for host-guest assemblies with **1-bromooctadecane** in various solvents: the ratio of CC\* to total peak area (red column) and film thickness (green column)

## Appendix C - Calculation for the ratio of host to guest

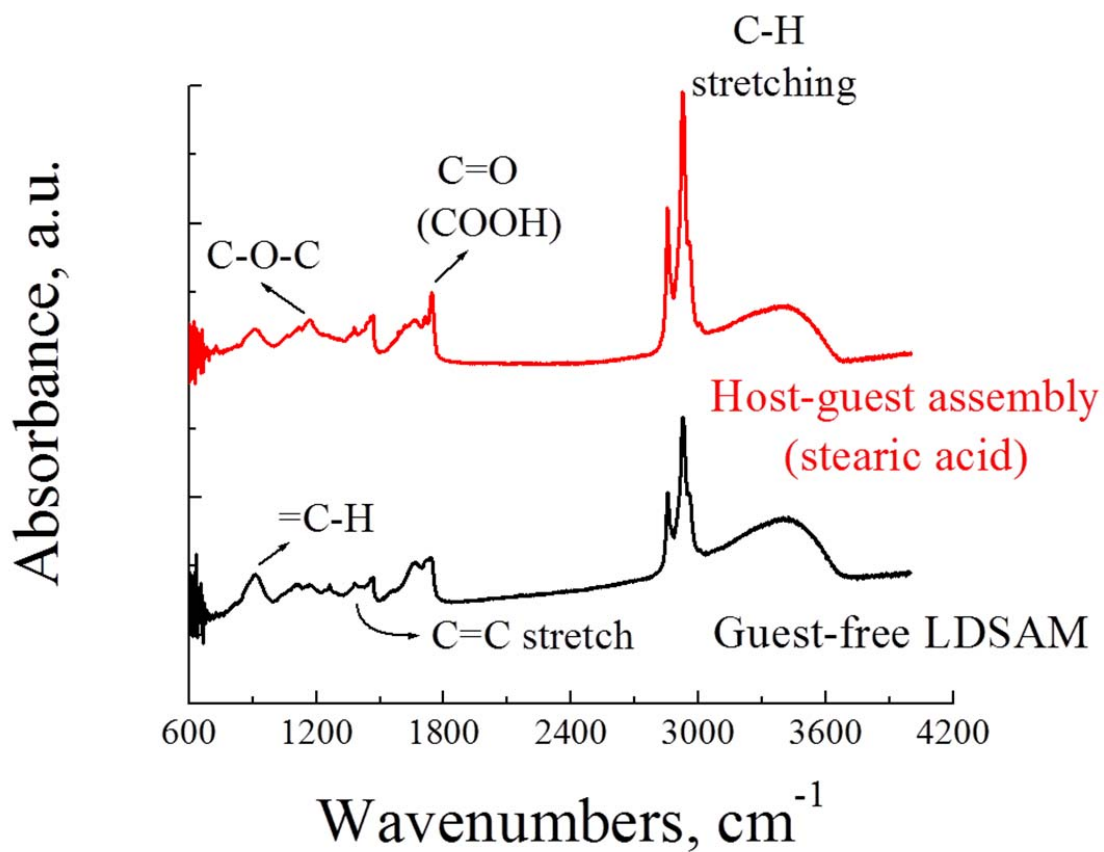
Radius of effective gold-coated quartz-crystal area	0.7	cm
The effective gold-coated quartz-crystal area	1.539	cm <sup>2</sup>
molecular area of host-molecule from $\pi$ -A isotherm	<b>53</b>	Å <sup>2</sup>

The number of alkane per unit area (cm <sup>2</sup> )	<b>1.887E+14</b>	① molecules/cm <sup>2</sup>
$\Delta m$ (from QCM measurement)	<b>8.999E+01</b>	③ ng/cm <sup>2</sup> ( <b>stearic acid</b> )
The number of stearic acid per unit area ③÷②	<b>1.905E+14</b>	④ molecules/cm <sup>2</sup>
$\Delta m$ (from QCM measurement)	<b>2.564E+02</b>	⑥ ng/cm <sup>2</sup> ( <b>naphthyl stearate</b> )
The number of naphthyl stearate per unit area ⑥÷⑤	<b>3.760E+14</b>	⑦ molecules/cm <sup>2</sup>
The ratio of host and guest for stearic acid ①÷④	<b>1.010</b>	1:1 host-guest assembly for stearic acid
The ratio of host and guest for naphthyl stearate ①÷⑦	<b>1.993</b>	1:2 host-guest assembly for naphthyl stearate



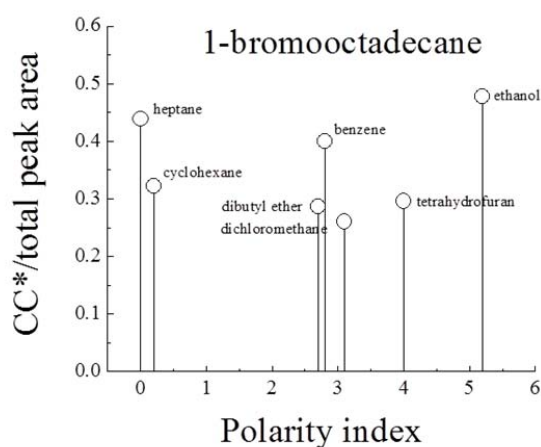
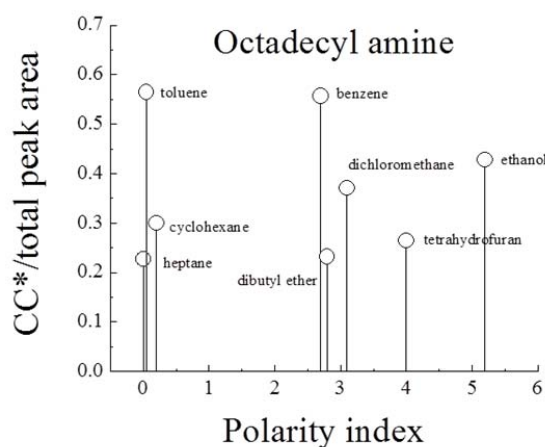
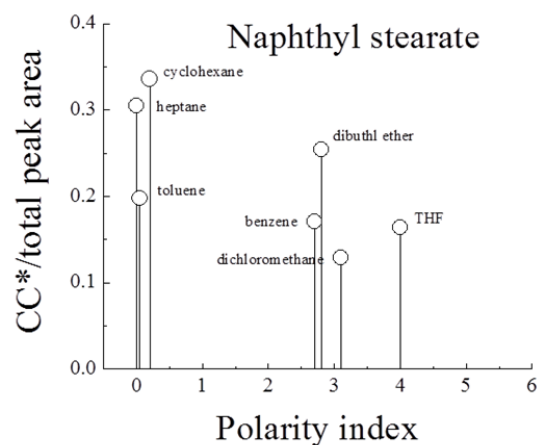
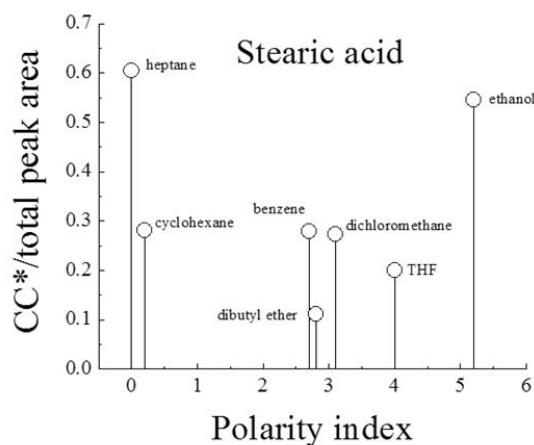
**S 15.** Schematic illustration of host-guest assemblies for stearic acid and naphthyl stearate respectively. 1:1 host-guest assembly for stearic acid and 1:2 host-guest assembly for naphthyl stearate.

**Appendix D** - Comparison of FTIR spectra between guest-free host-SAMs and host-guest assembly with stearic acid.

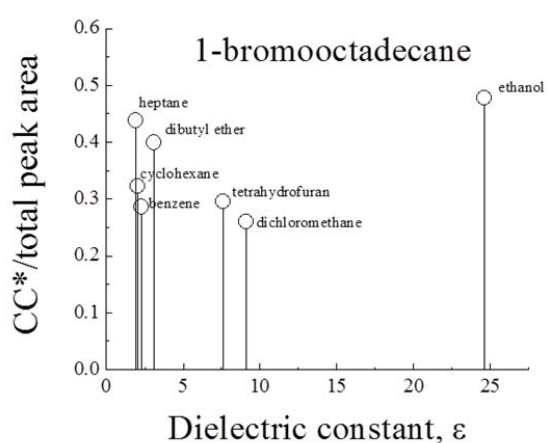
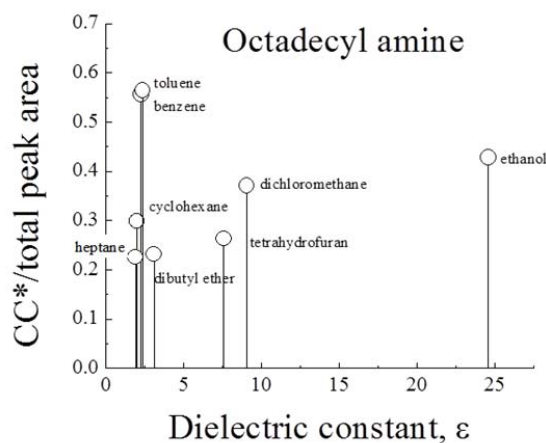
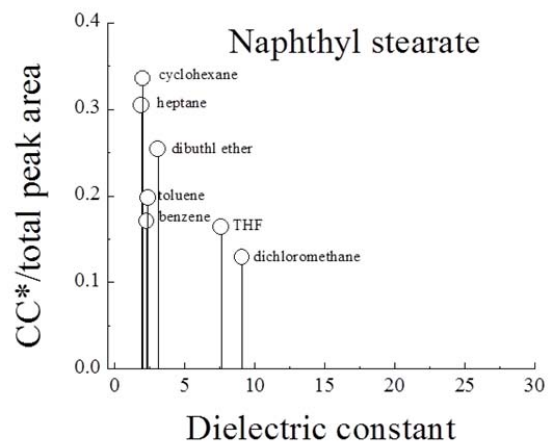
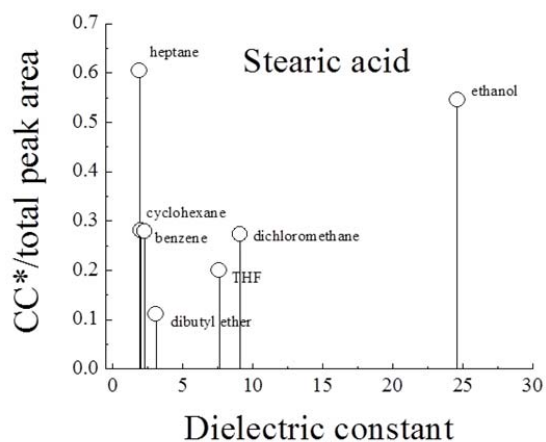


**S 16.** Comparison of FTIR spectra between guest-free host-SAMs and host-guest assembly with stearic acid. After the formation of host-guest assembly with stearic acid, FTIR spectra show a strong absorption peak at 1730 c m<sup>-1</sup> assigning to C=O for carboxylic acid.

**Appendix E** - The ratio of CC\* to total C 1s peak area for host-guest assemblies depending on polarity index of solvents or dielectric constant of solvents



**S 17.** The ratio of CC\* to total C 1s peak area for host-guest assemblies depending on the polarity index of solvents.



**S 18.** The ratio of CC\* to total C 1s peak area for host-guest assemblies depending on the dielectric constant of solvents.

**Appendix F** - The results of contact angles of water for host-guest assemblies in different guest molecules in various solvents.

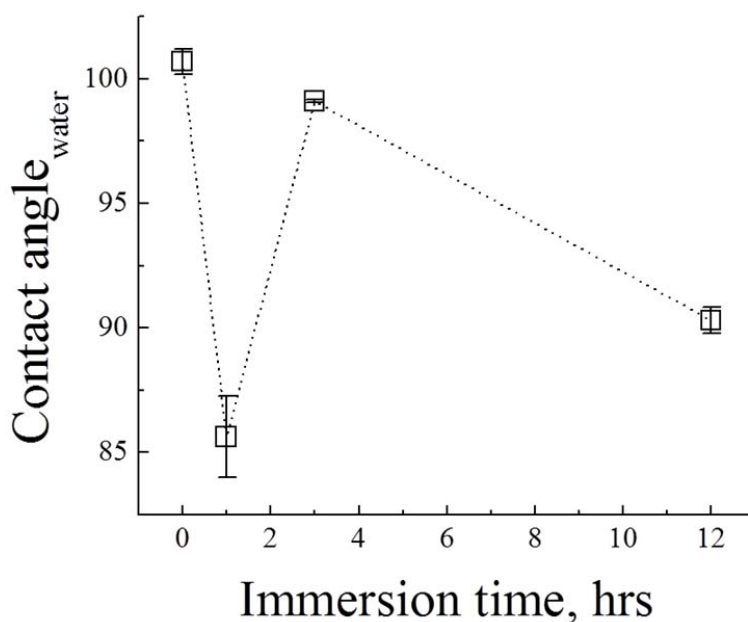
Guest-free LDSAMs	for 12 hrs <b>Stearic acid in</b>	Guest-included LDSAMs
104.53	Benzene	89.83
101.79	Cyclohexane	101.39
101.45	Dibutyl ether	95.34
99.94	Dichloromethane	96.95
100.68	Ethanol	90.30
100.30	Heptane	99.72
100.79	THF	67.86

Guest-free LDSAMs	for 12 hrs <b>2-naphthyl stearate in</b>	Guest-included LDSAMs
92.36	Benzene	93.60
95.72	Dibutyl ether	83.18
94.19	Dichloromethane	88.69
96.74	Cyclohexane	96.84
94.41	Heptane	91.72
94.62	THF	75.47
94.41	Toluene	85.85

Guest-free LDSAMs	for 12 hrs <b>Octadecyl amine in</b>	Guest-included LDSAMs
97.22	Benzene	107.24
96.36	Cyclohexane	111.30
95.87	Dibutyl ether	109.67
95.88	Dichloromethane	109.05
96.25	Ethanol	110.09
95.93	Heptane	121.10
96.22	THF	80.27
95.72	Toluene	107.19

Guest-free LDSAMs	for 12 hrs <b>1-bromooctadecane in</b>	Guest-included LDSAMs
103.34	Benzene	102.68
99.62	Cyclohexane	95.92
102.12	Dibutyl ether	92.87
100.42	Dichloromethane	102.56
100.65	Ethanol	97.82
102.39	Heptane	101.34
101.69	THF	71.35

**S 19.** The result of contact angle of water on host-guest assemblies in different guest molecules in various solvents for 12 hrs.



**S 20.** The result of contact angle of water for host-guest assembly depending on the time period of immersion in stearic acid solution in ethanol.

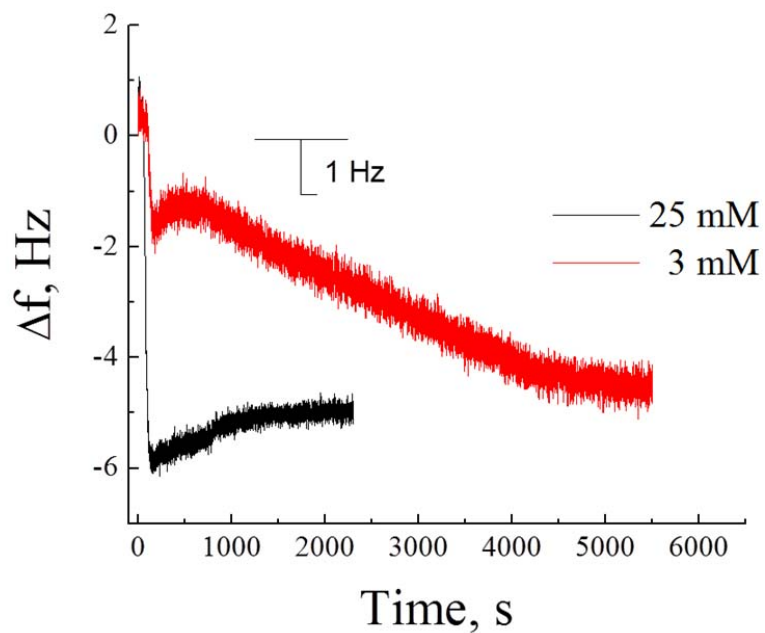
**Appendix G** - The comparison of the contact angle between guest-free LDSAMs, guest-included LDSAMs, and guest-removed LDSAMs.

**Contact angle**

<u>Guest-free</u> LDSAMs	Guest	Solvent	<u>Guest-included</u> LDSAMs	<u>Guest-removed</u> LDSAMs
97.2	<b>C18OH</b>	CHCl <sub>3</sub> (4.1)	79.0 ↓	89.6 ↑
100.4		EtOH (5.2)	63.6 ↓	98.7 ↑
97.6		THF (4.0)	42.2 ↓	88.1 ↑

**S 21.** The comparison of the contact angle between guest-free LDSAMs, guest-included LDSAMs, and guest-removed LDSAMs. Guest-free LDSAMs prepared using anthracene-based thiol host-molecules were immersed in the 1-octadecanol solution in different solvent. Guest-included LDSAMs were then immersed in pure ethanol for 12 hrs and sonicated for 10 min.

**Appendix H** - The dependence of the frequency shifts on the concentration of solution.



**S 22.** The dependence of the frequency shifts on the concentration of stearic acid solution. At equilibrium, the frequency shift is similar to each other.